A MODULUS GRADIENT ELASTICITY MODEL
FOR NANO-REINFORCED COMPOSITES

A THESIS SUBMITTED TO
THE GRADUATE SCHOOL OF NATURAL AND APPLIED SCIENCES
OF
MIDDLE EAST TECHNICAL UNIVERSITY

BY

HASAN GÜLAŞIK

IN PARTIAL FULFILLMENT OF THE REQUIREMENTS
FOR
THE DEGREE OF DOCTOR OF PHILOSOPHY
IN
THE DEPARTMENT OF AEROSPACE ENGINEERING

SEPTEMBER 2018

Approval of the thesis:

**A MODULUS GRADIENT ELASTICITY MODEL
FOR NANO-REINFORCED COMPOSITES**

submitted by **HASAN GÜLAŞIK** in partial fulfillment of the requirements for the degree of **the Doctor of Philosophy in the Department of Aerospace Engineering, Middle East Technical University** by,

Prof. Dr. Halil Kalıpçılar
Dean, Graduate School of **Natural and Applied Sciences**   _____

Prof. Dr. Ozan Tekinalp
Head of Department, **Department of Aerospace Engineering**   _____

Assoc. Prof. Dr. Ercan Gürses
Supervisor, **Department of Aerospace Engineering, METU**   _____

Examining Committee Members

Asst. Prof. Dr. Tuncay Yalçınkaya
Department of Aerospace Engineering, METU   _____

Assoc. Prof. Dr. Ercan Gürses
Department of Aerospace Engineering, METU   _____

Assoc. Prof. Dr. Serdar Göktepe
Department of Civil Engineering, METU   _____

Assoc. Prof. Dr. Cihan Tekoğlu
Department of Mechanical Engineering, TOBB   _____

Asst. Prof. Dr. Ali Javili
Department of Mechanical Engineering, Bilkent University   _____

Date: 06.09.2018

I hereby declare that all information in this document has been obtained and presented in accordance with academic rules and ethical conduct. I also declare that, as required by these rules and conduct, I have fully cited and referenced all material and results that are not original to this work.

Name, Last name: Hasan GÜLAŞIK

Signature

ABSTRACT

A MODULUS GRADIENT ELASTICITY MODEL
FOR NANO-REINFORCED COMPOSITES

Gülaşık, Hasan

Ph.D., Department of Aerospace Engineering

Supervisor: Assoc. Prof. Dr. Ercan Gürses

September 2018, 145 pages

In this work, nanocomposites and their numerical simulations are studied. At the beginning of the study, the properties of the polymer nanocomposites are explained based on a specific nano-inclusion and polymer matrix couple, namely, carbon nanotube (CNT) and thermoplastic polyetheretherketone (PEEK) polymer. In a literature comparison study, it is shown that the properties of the constituents, interface properties, manufacturing methods, characterization methods and therefore mechanical properties of the CNT/PEEK nanocomposites can vary significantly among different studies.

Classical elasticity formulations may become inadequate for the modeling of the nanostructured materials. They do not contain any information about the size and applicable from nanometer to meter scale. Moreover, they do not properly describe stress/strain singularities and are questionable if wavelength of deformation is comparable to dominant micro-structural length scale. Therefore, some extensions of the classical elasticity formulations have been proposed in literature. Two of the widely-used extensions, the Eringen's nonlocal elasticity and the Aifantis's gradient elasticity formulations, are explained. It is seen that nonlocal/gradient formulations include higher order fields and boundary conditions which are not easy to understand intuitively. They also have complex formulations and are

computationally expensive.

In this work, a new gradient elasticity formulation, the so-called E-grad model, is proposed to overcome some of the difficulties in the nonlocal and the gradient elasticity formulations. In the new formulation, similar to the differential relation between the local strain and the gradient enhanced strain in the classical models of gradient elasticity, a differential relation is proposed for the elastic constants of linear elasticity. Analytical and finite element solutions of the proposed formulation are derived for a one-dimensional inhomogeneous rod. The results of the proposed model are compared with a classical model of gradient elasticity for a one-dimensional model problem. It is seen that the discontinuities in the modulus, displacement, strain and stress fields are removed by the proposed model. Furthermore, there are no additional higher-order fields and boundary conditions and the numerical formulations are simpler than the nonlocal/gradient elasticity models.

Then, the E-grad model is extended to more general three-dimensional inhomogeneous materials with isotropic linear elastic constituents. The finite element formulation for axisymmetric problems is derived and a model problem of a soft cylindrical rod with a stiff spherical inclusion is solved. It is seen that discontinuities and/or sharp changes in the modulus, displacement, strain and stress fields that exist in local formulations are smoothed out with the proposed model. The proposed model is compared with a micromechanical model from literature and experiments conducted on polyimide/silica nanocomposites. The results obtained by the proposed approach agree well with the experimentally measured values of the nanocomposite modulus. The model is also extended to obtain anisotropic macroscopic response by choosing different length scale parameters in different directions.

At the end, a CNT reinforced polymer nanocomposite problem from literature is reconsidered in which the nanocomposite is assumed to be composed of four distinct phases: CNT, interface, interphase and bulk polymer. Rather than being homogeneous, the interphase is considered to be graded by the E-grad model. By

using the E-grad model and the genetic algorithm optimization, homogenized elastic constants of the transversely isotropic effective fiber are calculated. It is seen that, although the effective fiber has higher modulus in the axial direction, it has lower modulus values in transverse and shear directions compared to the polymer matrix. Then, the effect of the orientation distribution of the effective fibers in a nanocomposite is taken into account by using an orientation distribution function. It is seen that, if effective fibers are aligned in a direction, the modulus of the composite increases in that direction as expected. However, it is also seen that, isotropic distribution of the effective fibers makes the composite to have lower modulus than the matrix due to low transverse and shear moduli of the effective fiber.

ÖZ

NANO-GÜÇLENDİRİLMİŞ KOMPOZİTLER İÇİN
BİR MODÜL GRADYANI ELASTİSİTE MODELİ

Gülaşık, Hasan

Doktora, Havacılık ve Uzay Mühendisliği Bölümü

Tez Yöneticisi: Doç. Dr. Ercan Gürses

Eylül 2018, 145 sayfa

Bu çalışmada, nanokompozitler ve sayısal benzetimleri çalışılmıştır. Başlangıçta, nanokompozitlerin özellikleri belirli bir nano-katkı/polimer çifti, karbon nanotüp (KNT) ve termoplastik polietereterketon (PEEK) polimer, baz alınarak araştırılmıştır. Bir literatür karşılaştırma çalışmasında, KNT/PEEK nanokompozitlerin, bileşen özelliklerinin, arayüz özelliklerinin, üretim yöntemlerinin, karakterizasyon yöntemlerinin ve bunlardan dolayı mekanik özelliklerinin her bir çalışmada önemli ölçüde değiştiği gösterilmiştir.

Klasik elastisite formülasyonu nano yapılı malzemelerin modellemesinde yetersiz kalabilmektedir. Klasik elastisite formülasyonları boyut konusunda herhangi bir bilgi içermezler ve nanometer boyutdan metre boyutuna kadar uygulanabilirler. Ayrıca, gerinim/gerilim tekilliğini gerektiğince tanımlayamazlar ve deformasyon ve mikro yapı boyutunun benzer olduğu durumlarda tartışmalıdırlar. Bundan dolayı, literatürde klasik elastisite formülasyonuna bazı açılımlar önerilmiştir. Çoklukla kullanılan bu açılımlardan ikisi, Eringen'in yerel olmayan elastisite ve Aifantis'in gradyan elastisite teorileri, açıklanmıştır. Yerel olmayan/gradyan elastisite modellerinin, anlamlandırılmaları kolay olmayan yüksek mertebeli alanlar ve sınır koşulları içerdiği görülmüştür. Ayrıca, karmaşık formülasyonları vardır ve sayısal hesaplamaları pahalıdır.

Bu çalışmada, yerel olmayan elastisite ve gradyan elastisite formülasyonlarında karşılaşılan güçlüklerin üstesinden gelmek için yeni bir gradyan formülasyonu, E-grad modeli, önerilmiştir. Yeni formülasyonda, gradyan elastisite formülasyonundaki local gerinim ve gradyanla geliştirilmiş gerinim arasındakine benzer bir diferansiyel denklem, doğrusal elastisite malzeme parametreleri için önerilmiştir. Önerilen formülasyonun analitik ve sonlu eleman çözümleri, bir boyutlu homojen olmayan bir çubuk için verilmiştir. Önerilen formülasyon sonuçları ve gradyan elastisite formülasyon sonuçları, bir boyutlu örnek bir problem için karşılaştırılmıştır. Önerilen formülasyon ile modülüs, deplasman, gerinim ve gerilim alanlarındaki süreksizliklerin kaldırıldığı görülmüştür. Ek olarak, yüksek mertebeli alanlar ve sınır koşulları yoktur ve sayısal formülasyonları yerel olmayan/gradyan elastisite modellerinden daha basittir.

Daha sonra, E-grad modeli izotropik lineer elastik bileşenlerden oluşan üç boyutlu genel bir malzemeye genişletilmiştir. Eksenel simetrik problemler için sonlu eleman formülasyonu verilmiştir ve sert küresel bir katkı içeren yumuşak silindirik çubuktan oluşan örnek bir problemin çözümü verilmiştir. Önerilen formülasyonu ile, yerel elastisite formülasyonunda görülen modülüs, deplasman, gerinim ve gerilim alanlarındaki keskin değişimlerin yumuşatıldığı görülmüştür. Önerilen model, literatürden mikromekanik bir model ve poliamid/silica nanocomposite malzeme test sonuçları ile karşılaştırılmıştır. Önerilen modelin nanokompozit malzeme test sonuçlarını yakaladığı görülmüştür. Model, farklı yönlerde değişik uzunluk parametreleri kullanılarak, makro düzeyde anizotropik yanıt alacak şekilde geliştirilmiştir.

Çalışmanın sonunda, literatürden bir KNT ile güçlendirilmiş polimer, ki KNT, arayüz, arafaz ve polimerden oluşmaktadır, problemi yeniden ele alınmıştır. Arafazın, homojen malzemelerden farklı olarak, E-grad modeli kullanılarak aşamalı değişim gösteren malzeme özellklerine sahip olduğu düşünülmüştür. E-grad modeli ve genetik algoritma optimizasyonu kullanılarak, enine izotrop etkin bir efektif fiberin homojenleştirilmiş elastik sabitleri hesaplanmıştır. Polimer matrisle karşılaştırılınca, her ne kadar efektif fiberin eksenel yönde daha yüksek modüle

sahip olduğu görülsede, en ve kesme yönlerinde daha düşük modüle sahip olduğu görülmüştür. Daha sonra, fiberlerin yönelim etkisini dikkate almak için bir yönelim dağılımı fonksiyonu kullanılmıştır. Fiberler belirli bir yönde hizalanırsa, beklenildiği gibi, o yönde kompozit modülünün arttığı görülmüştür. Buna rağmen, efektif fiberin izotropik dağıldığı durumda, efektif fiberin düşük en ve kesme modüllerinden kaynaklı olarak, kompozit malzemenin matrise göre daha düşük modüle sahip olduğu görülmüştür.

Anahtar Kelimeler: nanokompozit, karbon nanotüp (KNT), PEEK polimer, yerel olmayan elastisite, gradyan elastisite, büyüklük etkisi, homojen olmayan malzemeler, sonlu elemanlar metodu (SEM)

to mom

ACKNOWLEDGEMENTS

Firstly, I would like to express my sincere gratitude to my supervisor Assoc. Prof. Dr. Ercan Gürses for his continuous support during my PhD. He has always been an understanding person and tried to help in any subject I asked for.

I would like to thank specially to project collaborator Assoc. Prof. Dr. Serdar Göktepe for his invaluable comments and suggestions during my PhD study. It has always been very instructive to discuss with him.

I would like to thank to project collaborators Assoc. Prof. Dr. Hande Toffoli, Dr. Mine Konuk, Gözde Toraman and Elif Sert for their collaboration which helps me to understand molecular dynamics.

I would like to thank to my thesis monitoring committee member Assoc. Prof. Dr. Cihan Tekoğlu, for sharing his knowledge about the subject and giving feedbacks during our meetings.

I would like to thank to the thesis committee members, Asst. Prof. Dr. Tuncay Yalçınkaya and Asst. Prof. Dr. Ali Javili for their interest and participating in the thesis defense committee.

TABLE OF CONTENTS

TABLES

FIGURES

xxiii

SYMBOLS AND ABBREVIATIONS

A, **A**   : Area, 6th order elasticity tensor

B, **B**   : matrix of the shape functions derivative, 5th order elasticity tensor

C   : 4th order elasticity tensor

CF   : Carbon Fiber

C$_h$: Chiral vector

CNT   : Carbon Nanotube

CVD   : Chemical Vapor Deposition

DDS   : Dynamic Dielectric Spectroscopy

DMA   : Dynamic Mechanical Analyzer

DMF   : Dimethylformamide

DSC   : Differential Scanning Calorimeter

DWCNT   : Double Wall Carbon Nanotube

D, D   : Elasticity tensor, diameter

Du   : Normal derivative of the displacement

DFT   : Density Functional Theory

E   : Young's modulus

F   : Force vector

FE   : Field Emission

FE/FEM   : Finite Element / Finite Element Method

FIBM   : Focused Ion Beam Microscope

FT-IR   : Fourier Tranform-InfraRed

G   : Shear modulus

GF   : Glass fiber

GO   : Graphene oxide

GPa	: GigaPascal
HR	: High Resolution
HSS	: High Strength Steel
K	: Kelvin, Stiffness matrix
KNT	: Karbon Nanotüp
L	: length
LFA	: Laser Flash Analyzer
MD	: Molecular Dynamics
MPa	: MegaPascal
MW	: Molecular Weight
MWCNT	: Multi Wall Carbon Nanotube
N	: Newton, shape function
P	: Pressure, Load
Pa	: Pascal
PBA	: Phenoxybenzoic acid
PEEK	: PolyEtherEtherKetone
PEES	: PhenyleneEtherEtherSulfone
PEK	: PolyEtherKetone
PES	: PolyEtherSulphone
PPA	: Polyphosphoric acid
R	: Radius
RS	: Raman Spectroscopy
RVE	: Representative Volume Element
S	: Siemens
SEM	: Scanning Electron Microscope
SWCNT	: Single Wall Carbon Nanotube

T	: CNT axis vector, Temperature
T_g	: Glass transition temperature
T_m	: Melting temperature
T_d	: Degrading temperature
TEM	: Tranmission Electron Microscope
TGA	: Thermo-Gravimetric Analysis
THE	: Temsili Hacim Elamanı
TMA	: Thermo-Mechanical Analyzer
TPa	: TeraPascal
TWCNT	: Three Wall Carbon Nanotube
W	: Watt
WF	: weight fraction
V	: Volume
VF	: volume fraction
a, a	: unit vector, area
b	: body load
c	: internal length scale parameter
cm	: centimeter
d	: diameter, distance
div	: divergence operator
f	: force vector
g, -g-	: gram, attenuation function, -grafted-
h	: hour
kg	: kilogram
l	: length, distance
ℓ	: internal length scale parameter

m, m	: unit vector, meter
min	: minute
mm	: millimeter
n	: unit vector
nm	: nanometer
q	: higher order traction
r, **r**	: radius, line load
rpm	: revolution per minute
s	: second
t	: thickness, time
t	: traction
tr	: trace operator
u	: displacement, deformation
v	: volume
w	: width, watt, weight function, strain energy density
wt	: weight percentage
x	: material point
Å	: Angstrom
Γ	: integral domain surface boundary
γ, $\boldsymbol{\gamma}$	: integral domain line boundary, relative deformation
$\boldsymbol{\varepsilon}$	: strain
$\boldsymbol{\eta}$	: strain gradient filed
θ	: angle, rotation
κ	: bulk modulus
λ	: Lame constant
δ	: Dirac delta function

μ	: Lame constant, higher order stress field
μm	: micrometer
ν	: Poisson's ratio
Π	: strain energy
π	: Pi number
ρ	: density
σ, **σ**	: electrical conductivity, stress
ϑ	: viscosity
φ	: micro deformation
ω	: rotational speed
Ω	: integral domain
∇	: del, gradient operator
∇^2	: Laplacian
∂	: derivative
°, °C	: degree, degree Celsius

xxx

CHAPTER 1

INTRODUCTION

In today's industry, especially in aviation, composite materials are replacing homogeneous materials because of their enhanced material properties, high strength/density and high rigidity/density ratios. There are even aircrafts, Boeing 787 Dreamliner and Airbus A350, which utilized considerable amount of carbon fiber reinforced polymer composites. Carbon fiber or glass fiber reinforced polymer/ceramic/metallic materials are well known to most of the people, Figure 1.1. Besides these usual fiber reinforced composite materials, there are also nano-reinforced composites.
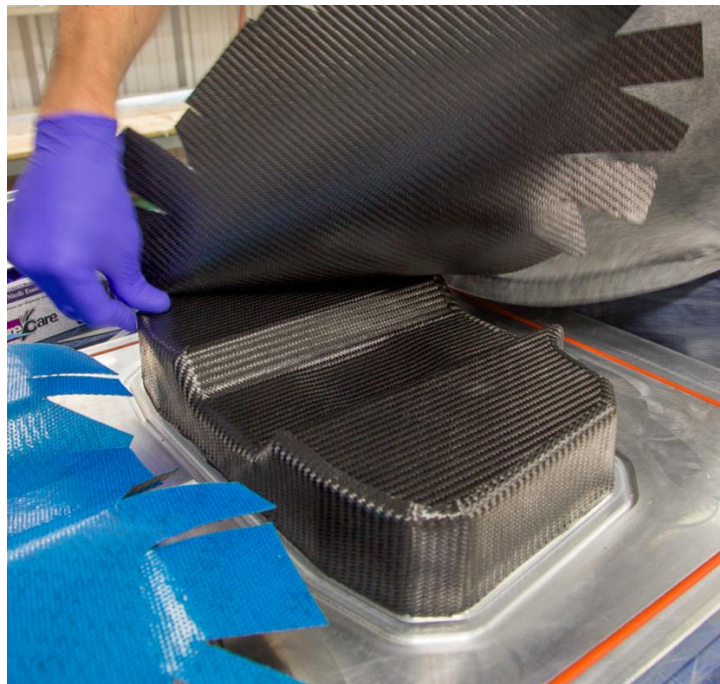
Figure 1.1 – *A carbon fiber (CF) reinforced polymer part is being manufactured (Innovativecomposite, 2018)*

Nanocomposites are composed of at least two materials, a reinforcing nano-inclusion and a matrix material. Polymer, ceramic and metallic materials can be used

as matrix materials, with the same nano inclusion, i.e., carbon nanotube (CNT), graphene, silica. Figure 1.2 shows a scanning electron microscope (SEM) image of a multi walled carbon nanotube (MWCNT)/carbon fiber (CF)/polyetheretherketone (PEEK) polymer nanocomposite. Note that, in the figure, the size of MWCNTs is much smaller than the CFs. For the same volume or mass fractions, the surface area of the nano-inclusions is much higher than the corresponding micro or macro counterparts. Therefore, small amount of nano-inclusion can enhance the material properties significantly.

The nano-inclusions are used to enhance mechanical, thermal and electrical properties of the matrix material. With a proper understanding of the properties of the nanocomposites, reliable numerical models can be proposed. Therefore, in Chapter 2, the properties of the nanocomposites are discussed. Rather than giving general information about the nanocomposites, a specific nano-inclusion (CNT)/ polymer (PEEK) couple is selected to better investigate the nanocomposites. Individual material properties, interface properties, manufacturing processes, structural characterization methods and mechanical properties of CNT/PEEK nanocomposites are compared among several works from literature.
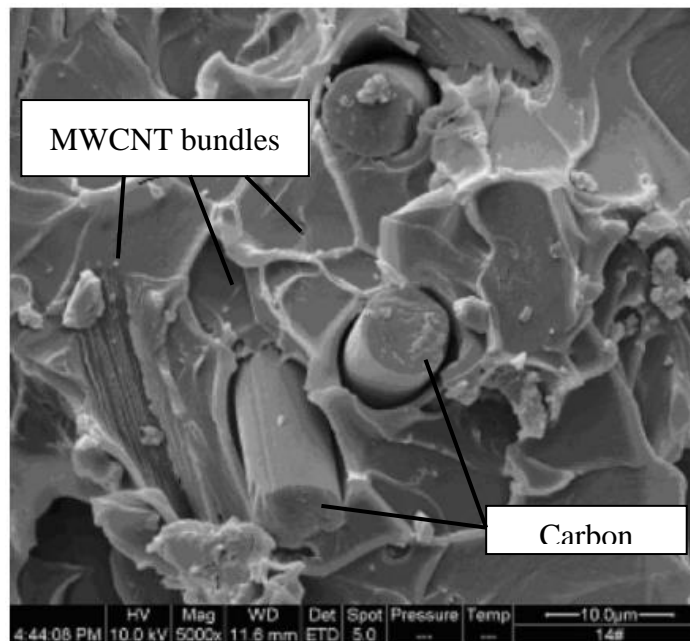
Figure 1.2 - *Field emission scanning electron microscopy (FE-SEM) of a fractured sample of MWCNT/CF/PEEK composite (Li and Zhang, 2011)*

In nanoscale, materials exhibit different properties than in the macro scale. The overall effect can be named as the size effect. For the modeling of materials in small (sub-micron) scales, atomistic or quantum mechanics based simulation methods are generally used, i.e., density functional theory (DFT), molecular dynamics (MD) and the coarse grain methods. However, the atomistic simulations are computationally significantly more expensive than the continuum mechanics based methods. The spanned time and length scales are also limited with the atomistic simulations. On the contrary, classical continuum based simulations are computationally efficient but these methods normally do not include any parameter to account the size effect for nano-structured materials. Therefore, extensions have been proposed to the classical local continuum theories over the years. The Mindlin's higher order elasticity theory, the Eringen's nonlocal elasticity model and the Aifantis's gradient elasticity models are the most well-known continuum models. In Chapter 3, to develop a thorough understanding of these models, Eringen's nonlocal elasticity and Aifantis's gradient elasticity models are explained in detail.

Although, they can take the size effect into account, the nonlocal and gradient elasticity models have some shortcomings. They require introduction of some additional higher order strain and stress fields and also boundary conditions which are not always easy to motivate physically. Therefore, to overcome some of the difficulties in nonlocal and gradient elasticity formulations, a new gradient elasticity formulation, the so-called E-grad model, is proposed for a one-dimensional inhomogeneous rod in Chapter 4. In the new formulation, similar to the differential relation between the local strain and the gradient enhanced strain in the classical models of gradient elasticity, a differential relation is proposed for the Young's modulus. Analytical and finite element solutions of the proposed formulation are derived for a one-dimensional inhomogeneous rod. The results of the proposed model are compared with a classical model of gradient elasticity for a model problem of carbon nanotube reinforced polymer composite.

In Chapter 5, the one-dimensional E-grad model proposed in the previous chapter is extended to more general three-dimensional inhomogeneous materials with

isotropic linear elastic constituents. In addition to the constitutive equations and the balance relations, differential relations for the material parameters of isotropic linear elasticity are provided. The finite element formulation for axisymmetric problems is derived and a model problem of a soft cylindrical rod with a stiff spherical inclusion is solved. The proposed model is compared with a micromechanical model from literature and experiments conducted with polyimide/silica nanocomposites. Finally, the model is extended to obtain an anisotropic macroscopic response.

In Chapter 6, a CNT reinforced polymer nanocomposite problem from literature is reconsidered. To this end, the nanocomposite is assumed to consist of four distinct phases: CNT, interface, interphase and bulk polymer. Rather than being homogeneous, the interphase is considered to be graded and the E-grad model is utilized to determine its properties. Then, the CNT, the interface and the interphase are treated as a transversely isotropic effective fiber. By using the E-grad model and the genetic algorithm optimization, homogenized elastic constants of the effective fiber are calculated. In nanocomposites, rather than a perfect alignment in a specific direction fibers/CNTs are either randomly distributed or oriented around a main direction. The statistical distribution of CNTs in a polymer matrix is discussed. The effect of orientations of the fibers are taken into account by using orientation distribution functions. Finally, the elastic properties of the nanocomposite with different fiber orientation distribution are computed.

In Chapter 7, an overall discussion of the study is given, the conclusions are drawn and the potential future studies are considered.

1.1. MOTIVATION AND OBJECTIVES

It is well-known that small amount of nano-inclusions enhances the matrix material properties significantly. Therefore, nano-reinforced composites have a great potential in a wide range of applications in several industries. For this purpose, material models are needed to account for the size effect in the nano-structured materials. Available nonlocal and gradient material models require introduction of some additional higher-order strain and stress fields and also boundary conditions which are not always easy to motivate physically and understand intuitively. On the

other hand, atomistic simulations are computationally very expensive and require a different area of expertise than the continuum scale models. Therefore, the main motivation of this study is to develop a more general and intuitively understandable modeling approach for the numerical simulation of polymer nanocomposites.

The first objective of the study is to develop a deeper understanding of the individual material properties, interface properties, manufacturing processes, structural characterization methods and mechanical properties of nanocomposites. The second objective is to build theoretical and numerical modeling experience about the nonlocal and gradient elasticity models. It is the third and the main objective to develop a simple gradient elasticity model for the numerical simulation of the polymer nanocomposites. The last objective is to apply the developed model to different problems in literature for the validation of the model.

CHAPTER 2

POLYMER NANOCOMPOSITES

As stated previously, a small amount of nano inclusion can enhance the properties of the matrix material in great amounts. For a deeper understanding of the properties of a composite, a comprehensive knowledge from individual constituents to composite level has to be developed. Instead of giving general information about nanocomposites, it is better to choose a specific nano-inclusion/matrix material couple and explain the properties of the nanocomposite based on this couple. In this study, carbon nanotube (CNT) reinforced polyetheretherketone (PEEK) polymer is investigated as an example.

General information about CNT and PEEK is given in Section 2.1 and Section 2.2, respectively. In Section 2.3, detailed information about the individual constituents of the nanocomposite, interface properties between CNT and PEEK, manufacturing methods, characterizing methods and mechanical properties of nanocomposites are given.

2.1.   CARBON NANOTUBE (CNT)

The diameters of the carbon fibers (CF) used today, generally are in the micrometer range. It is known that, for a specified volume fraction, decreasing the diameter of the reinforcing fibers increases the interface area between the fiber and the matrix which eventually results in stronger composite materials. One of the most promising candidate for reinforcing fibers is CNT. CNTs are thought to replace or used together with the common carbon fibers in the composites because of their nano-size diameter which enhances the adhesion surface area. In the investigations, it is seen that inclusion of minimum amount of CNT into polymers enhances the mechanical, electrical and thermal properties of the polymers (Boyer et al. 2012, Zhang et al. 2012).

CNTs can be described as cylindrical tubes which are made by rolling graphene

sheets around a certain axis. If a CNT has a single carbon layer, it is a single-wall carbon nanotube (SWCNT), if it has more than one carbon layer, it is a multi-wall carbon nanotube (MWCNT), see Figure 2.1. In Figure 2.2, unit translational vectors on a graphene layer, $\boldsymbol{a}_1$ and $\boldsymbol{a}_2$, are shown which compose the chiral vector, $\boldsymbol{C}_h$, of a CNT. The chiral vector is calculated as:

$$C_h = m\boldsymbol{a}_1 + n\boldsymbol{a}_2 \tag{2.1}$$

Where, m and n show the number of hexagons travelled by the unit vectors. The $\boldsymbol{T}$ vector designates the CNT axis and perpendicular to $\boldsymbol{C}_h$ (Kalamkarov et al., 2006). The chiral angle, θ, is defined as the angle between $\boldsymbol{C}_h$ and $\boldsymbol{a}_1$ and changes between 0° and 30°. By using the parameters m and n, θ is calculated as (Grady, 2011):

$$tan\theta = \frac{n-m}{\sqrt{3}(n+m)} \tag{2.2}$$

The diameter of the CNT can be calculated as (Dresselhaus et al. 1995):

$$d = \frac{a}{\pi}\sqrt{n^2 + m^2 + nm} \tag{2.3}$$

where, d in the above formula is in angstrom (Å). The constant a is equal to 2.46 Å for carbon. According to the chiral angle, CNTs have armchair, zigzag and chiral configurations, see Table 2.1 and Figure 2.3.

(a)

graphene   SWCNT

(b)
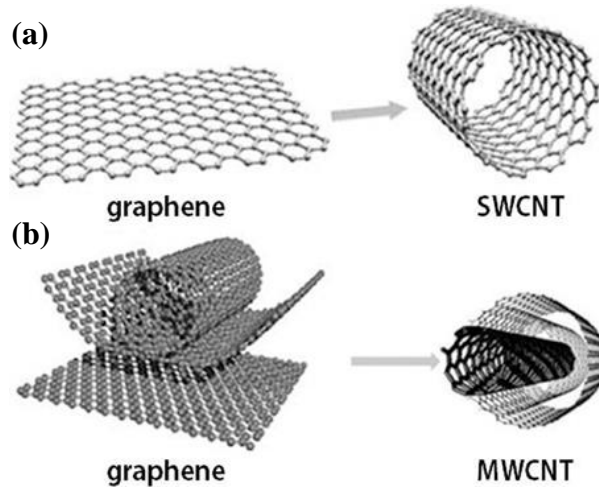
graphene   MWCNT

Figure 2.1 - *(a) Single-Wall Carbon Nanotube (SWCNT), (b) Multi-Wall Carbon Nanotube (MWCNT) (Vidu et al. 2014)*
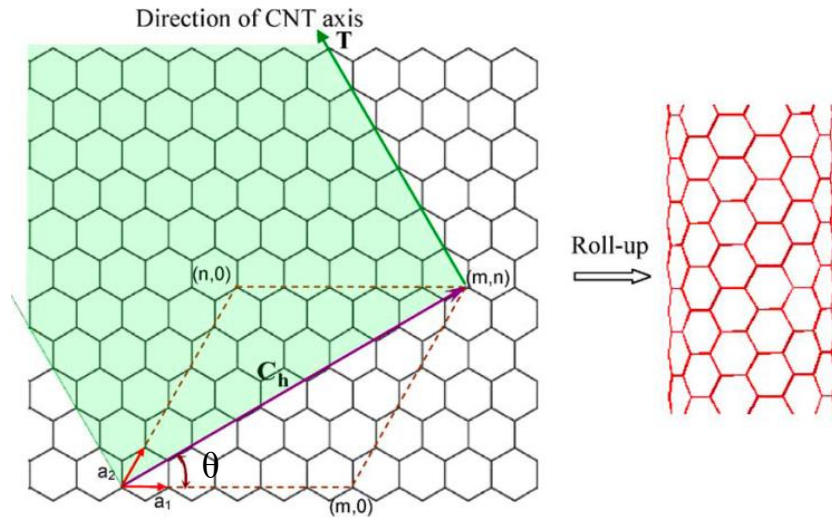
Figure 2.2 *- (a) Unit translational vectors $\boldsymbol{a}_1$, $\boldsymbol{a}_2$ and chiral vector, $\boldsymbol{C}_h = m\boldsymbol{a}_1 + n\boldsymbol{a}_2$, on a graphene layer. Chiral vector shows the rolling direction while tangent vector, $\boldsymbol{T}$, shows the CNT axis (Kalamkarov et al., 2006)*

Table 2.1 *- CNT types based on chiral angle*

CNT type	Chiral vector, C_h	Chiral angle, θ [°]
zigzag	$(m, 0)$	0°
armchair	(m, m)	30°
chiral	$(m, n), m \neq 0, n \neq 0$	$0° < \theta < 30°$
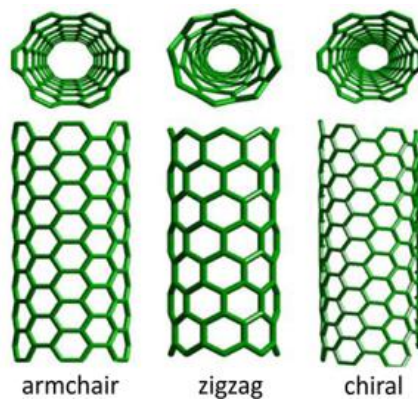
Figure 2.3 *– Armchair, Zigzag, Chiral SWCNTs (Madani et al., 2013)*

9

CNTs have extraordinary mechanical, thermal and electrical properties because of their high length/diameter ratio and covalent bonds between the carbon atoms. The covalent bonds between the carbon atoms make the nanotubes one of the strongest materials known.

Table 2.2 (Tserpes and Silvestre, 2014) compares the mechanical properties of CNT with other commonly used engineering materials. It can be seen that CNT has much higher modulus (E), strength and toughness than the high strength steel (HSS) with a 1/5 density of the HSS. Therefore, CNT has extremely high specific strength compared to conventional engineering materials.

Table 2.3 (Tserpes and Silvestre, 2014) shows the thermal and electrical properties of CNTs. It can be seen that CNTs have ten times thermal conductance and almost the same electrical conductance compared to copper which is the most widely used conductive material. The thermal and electrical properties of CNTs are also better than the common carbon fibers.

Figure 2.4 (Liu et al., 2009) shows conduction properties of zigzag, chiral and armchair CNTs for different values of m and n. If the difference between m and n can be divided by three, CNTs show conducting behavior.

Table 2.2 - Mechanical properties of CNT (Tserpes and Silvestre, 2014)

Fiber Material	Specific Density [gr/cm³]	E [TPa]	Strength [GPa]	Strain at Break [%]
CNT	1.3 – 2	1	10 – 60	10
HS Steel	7.8	0.2	4.1	< 10
Carbon fiber	1.7 – 2	0.2 − 0.6	1.7 – 5	0.3 − 2.4
E/S - glass	2.5	0.07 / 0.08	2.4 / 4.5	4.8
Kevlar 49	1.4	0.13	3.6 − 4.1	2.8

Table 2.3 *- Thermal and electrical properties of CNT (Tserpes and Silvestre, 2014)*

Material	Thermal Conductivity [W/(m.K)]	Electrical Conductivity [S/m]
CNT	$25 - 3000$	$10^6 - 10^7$
Copper	400	6×10^7
CF	1000	$2 \times 10^6 - 8.5 \times 10^6$
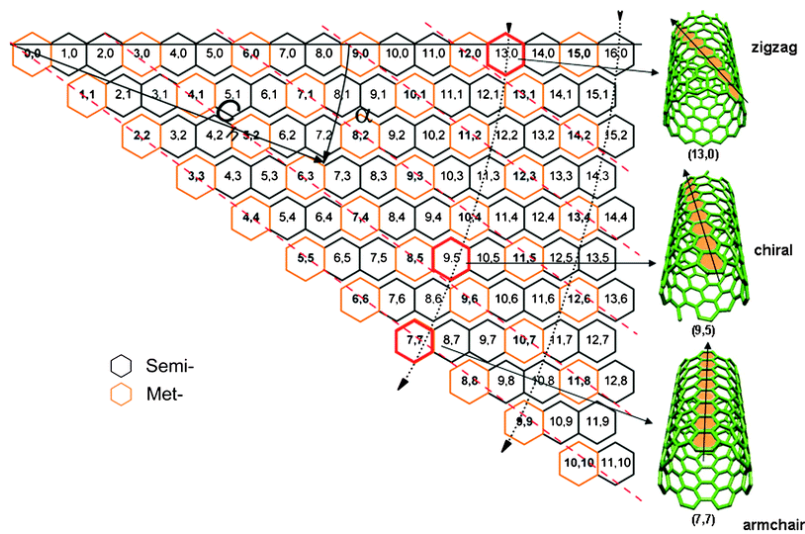
Figure 2.4 *– Semiconductor and conductor (metallic) SWCNT types obtained for different rolling directions (Liu et al., 2009)*

2.2.   POLY ETHER-ETHER KETONE (PEEK)

The other constituent of the composite material is the polymer matrix. Thermoset polymers are mostly used in industry, e.g. epoxy, because of their high strength compared to thermoplastic and elastomer polymers. But they cannot be recycled and therefore they are environmentally not preferable.

Thermoplastic polymers are good candidates to replace the thermosets. First of all, they can be recycled and used repeatedly. In addition, moderate strengths are achievable with thermoplastics. PEEK is one of the candidates to be used, especially in structural applications. PEEK is a colorless, semi-crystalline, high performance,

thermoplastic polymer. Figure 2.5 shows a PEEK monomer, $C_{21}H_{18}O_3$.
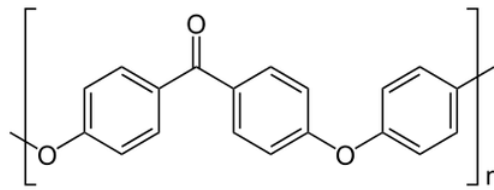
Figure 2.5 – PEEK monomer (Wikipedia, 2018)

The advantageous properties of the PEEK are listed below (Brydson, 1999):

- PEEK can be recycled as other thermoplastic polymers.
- PEEK has high stiffness ($E \simeq 3$ GPa) snd strength ($\sigma_f \simeq 100$ Mpa). Therefore, it is suitable for structural applications.
- PEEK is wear resistant. Therefore, it is suitable for tribology applications i.e. bearings, gears, (Li and Zhang, 2011).
- PEEK has a high chemical, radiation and moisture resistance. Therefore, it is suitable for harsh environment applications (chemical industry, space platforms, off-shore platforms…).
- PEEK has excellent thermal properties with high glass transition and melting temperatures ($T_g \simeq 140$ °C, $T_m \simeq 350$ °C). PEEK also has a low flammability rating (V-0) with low smoke and toxic gas emission. Therefore, it is suitable for interior applications (vehicle interiors, household devices…).

PEEK has some disadvantages in addition to its excellent properties:

- PEEK has high cost and low volume production compared to other polymers (Wikipedia, 2018).
- PEEK needs high processing temperatures because of its high T_g and T_m.

Figure 2.6 shows a general classification of the polymers. It can be seen that PEEK is one of the high performance polymers.
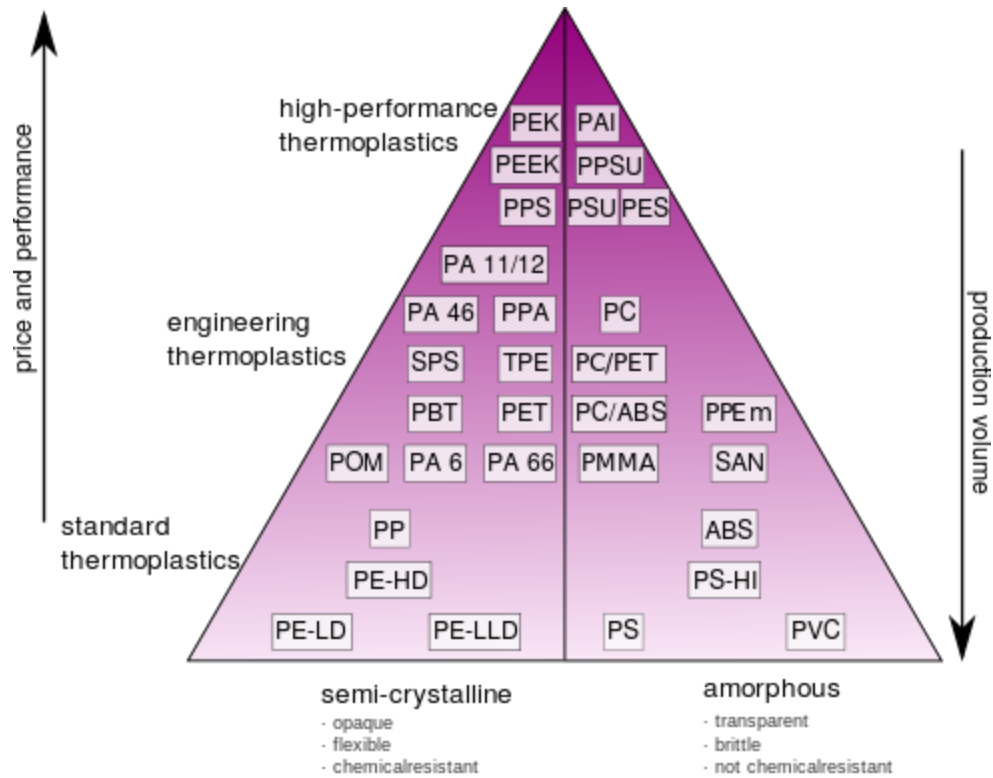
Figure 2.6– Classification of polymers by price, performance, production volume and crystallinity (Wikipedia, 2016)

2.3. CNT/PEEK COMPARISON STUDY

A numerical model of a composite material requires a comprehensive understanding of the material and its constituents. Therefore, a comparative study is made for the CNT/PEEK nanocomposite by using some articles listed in Table 2.4. The properties of the constituents, interface, manufacturing processes, characterization techniques and mechanical properties of the CNT reinforced PEEK nanocomposites are compared.

Table 2.4 – Considered articles in the CNT/PEEK comparison study

[1]	Boyer, F., Olivier, P.A., Pons, F., Cadaux, P.H. 2012. "Mechanical and electrical behavior of a Peek/Carbon nanotube composite".

[2] Tishkova, V., Raynal, P., Puech, P., Lonjon, A., Le Fournier, M., Demont, P., Flahaut, E., Bacsa W. 2011. "Electrical conductivity and Raman imaging of double wall carbon nanotubes in a polymer matrix".

[3] Jain, R., Choi, Y. H., Yaodong, L., Minus, M. L., Chae, H. G., Kumar, S., Baek, J. 2010. "Processing, structure and properties of poly(ether ketone) grafted few wall carbon nanotube composite fibers".

[4] Zhang, S., Wang, H., Wang, G., Jiang, Z. 2012. "Material With High Dielectric Constant, Low Dielectric Loss, And Good Mechanical And Thermal Properties Produced Using Multi-Wall Carbon Nanotubes Wrapped With Poly(Ether Sulphone) in a Poly(Ether Ether Ketone) Matrix".

[5] Mohiuddin, M., Hoa, S.V. 2011. "Temperature dependent electrical conductivity of CNT–PEEK composites".

[6] Li, J., Zhang, L.Q. 2011. "Reinforcing effect of carbon nanotubes on PEEK composite filled with carbon fiber".

[7] Guehenec, M., Tishkova, V., Dagreou, S. Leonardi, F., Derail, C., Puech, P., Pons, F., Gauthier, B., Cadaux, P.H., Bacsa, W. 2013. "The effect of twin screw extrusion on structural, electrical, and rheological properties in carbon nanotube poly-ether-ether-ketone nanocomposites".

[8] Hwang, Y., Kim, M., Kim, J. 2013. "Improvement of the mechanical properties and thermal conductivity of poly(ether-ether-ketone) with the addition of graphene oxide-carbon nanotube hybrid fillers".

[9] Ashrafi, B., Díez-Pascual, A.M., Johnson, L., Genest, M., Hind, S., Martinez-Rubi, Y., González-Domínguez, Jose M., Martínez, M. T., Simard, B., Gómez-Fatou, M.A., Johnston, A. 2012. "Processing and properties of PEEK/glass fiber laminates: Effect of addition of single-walled carbon nanotubes".

[10] Ogasawara, T., Tsuda, T., Takeda, N. 2011. "Stress–strain behavior of multi-walled carbon nanotube/PEEK composites".

2.3.1. Constituents of CNT/PEEK Nanocomposites

In the list below, the individual material properties of the nanocomposites can be found for the considered articles. Therefore, a better comparison can be made and differences among the composites may be underlined starting from the material level.

[1]- Boyer et al., 2012

- CNT: MWCNT ($d = 10 - 15$ nm, $l = 0.1 - 10$ μm, $5 - 15$ walls)
- PEEK: grade 1000P ($T_g = 149\ °C$, $\vartheta = 50$ Pa. s@380°C), grade 2000P ($T_g = 149\ °C$, $\vartheta = 270$ Pa. s@380°C)

[2] - Tishkova et al., 2011

- CNT: 12% SWCNT, 70% DWCNT, 16% TWCNT, 1.5% QWCNT (Chemical Vapor Deposition, CVD, $d = 2.8$ nm, $l = 10$ μm)
- PEEK: grade 90P ($\rho = 1.3$ g/cm³ @25°C, $T_m = 341°C$, $\vartheta = 90$ Pa. s @ 400°C, $crystallinity = 32\%$)

[3] - Jain et al., 2010

- CNT: MWCNT
- PEK: 4-phenoxybenzoic acid (4-PBA) monomer, poly phosphoric acid (PPA), phosphorous pentoxide (P_2O_5)

[4] - Zhang et al., 2012

- CNT: MWCNT
- PEEK: no information given

[5] - Mohiuddin and Hoa, 2011

- CNT: MWCNT (CVD, $purity = 95\%$, $\rho = 2.2$ g/cm³, $d_{outer} = 13 - 16$ nm, $d_{inner} = 4$ nm, $l = 1 - 10$ μm, $\sigma_{CNT} = 104$ S/cm)

- PEEK: ($\rho = 1.263$ g/cm^3)

[6] - Li and Zhang, 2011:

- CNT: MWCNT ($d = 6 - 20$ nm, $l = 1.5$ μm)
- PEEK: grade 450P ($\rho = 1.32$ g/cm^3, $T_g = 143°C$, $T_m = 334°C$, $T_d = 590°C$)

[7] - Guehenec et al., 2013

- CNT: MWCNT ($purity = 90\%$, $d = 50 - 150$ kg/m^3, $l = 0.1 - 10$ μm, $d = 15$ nm, 5-15 walls)
- PEEK: grade 2000P ($MW = 25000$ g/mol, $d = 1.2$ g/cm^3 @25°C, $T_g = 143°C$, $T_m = 345°C$)

[8] - Hwanget al., 2013

- CNT: MWCNT ($purity = 95\%$, $d = 40 - 60$ nm)
- PEEK: no information given

[9] - Ashrafi et al., 2012

- CNT: SWCNT (laser grown, arc grown)
- PEES: $MW = 38000$ g/mol, $\rho = 1.38$ g/cm^3 @25°C, $T_g = 192°C$
- PEEK: grade 150PF ($MW = 40000$g/mol, $\rho = 1.3$ g/cm^3 @25°C, $T_g = 147°C$, $T_m = 345°C$, $\vartheta = 103$ Pa. s @ 350°C)

[10] - Ogasawara et al., 2011

- CNT: MWCNT (CVD, $d = 40 - 100$ nm)
- PEEK: grade 151G

Although, not all of the references specified all the material properties, it is seen

from the above list that, there are lots of material configurations used in the references. CNTs have different properties in terms of the purity, density (ρ), diameter (d), length (l), and number of walls. Similarly, PEEK polymers have different specifications in terms of the molecular weight (MW), density, glass transition temperature (T_g), melting temperature (T_m) and the viscosity (ϑ). Therefore, it is reasonable to expect that, the composite properties will be different for each reference.

2.3.2. Interface of CNT/PEEK Nanocomposites

The successful load transfer between the CNT and the PEEK is in crucial importance for the performance of the nanocomposites. If no functionalization is done on the CNT, the load transfer is by the mechanical mechanisms and the weak van-der Walls attractions between the nanotube and the polymer. To increase the load transfer between CNT and PEEK, chemical treatments are applied on CNTs to form covalent bonds with PEEK. It is also known that, the chemical treatment influences the dispersion of the CNTs preventing agglomeration within the polymer matrix. Therefore, it is important to investigate the interface region separately and specify the current treatments on the constituents. The treatment procedures of PEEK and CNT are provided below for each reference if available.

[2] - Tishkova et al., 2011
- catalyst particles removed from CNTs through chemical etching
- CNTs washed many times with distilled water
- CNTs kept in acetone prior dispersion in PEEK
- PEEK powder added to CNT/acetone suspension
- suspension submitted to sonication for 10 s

[3] - Jain et al., 2010
- Grafting PEK (polyetherketone) on CNTs (PEK-g-MWCNT) by in-situ polymerization

17

- Monomer and MWCNT mixed under dry nitrogen purge at 130°C for 72 h

[4] - Zhang et al., 2012

- MWCNT wrapped in PES (polyethersulphone)

[8] - Hwanget al., 2013

- MWCNT purified and functionalized with carboxylic acid groups by heat treating the MWCNT in 800 mL of H_2SO_4 (Sulfuric acid) and HNO_3 (Nitric acid) in an ultrasonicater bath for 8h at room temperature
- Suspension heated to 50°C and stirred for 24 h and filtered through a nylon membrane
- Filtered cake washed thoroughly with water for several times until the filtrate becomes neutral
- Carboxylated MWCNT immersed into $SOCl_2$ (Thionyl chloride) using an ultrasonicator at room temperature for 1h and stirred for 12h at 65°C to convert the carboxylic acid groups on the surface of MWCNT to acid chlorides
- Suspension vacuum-filtered through a membrane, washed with THF (tetrahydrofuran), and dried for 12h under vacuum at ambient temperature.
- Chlorinated MWCNT dispersed in 20 mL of ethylenediamine and refluxed at 125°C for 2 days with stirring
- MWCNT also filtered through a nylon membrane and washed several times.
- Product dried under vacuum at room temperature for 24 h

[9] - Ashrafi et al., 2012

Laser-grown SWCNT:

- wrapped with PEES (Polyether ether sulfone)

Arc-grown SWCNT:

- thermally oxidized in an air atmosphere at 350 °C for 2 h

- then refluxed in HCl (Hydrochloric acid) for 4 h

- wrapped with PEES

From the above list, it can be seen that half of the references do not apply a treatment on the CNTs. The other references used different methods for the functionalization of CNTs. Chemical etching, grafting by in-situ polymerization, wrapping and oxidization are used. As seen in reference Hwang et al., (2013), the functionalization may take several days and numerous processing. Therefore, it is reasonable to develop standard procedures for the functionalization. This will also help the repeatability of the procedure and also experiments. Figure 2.7 shows some of the commonly used CNT functionalization methods in summary.
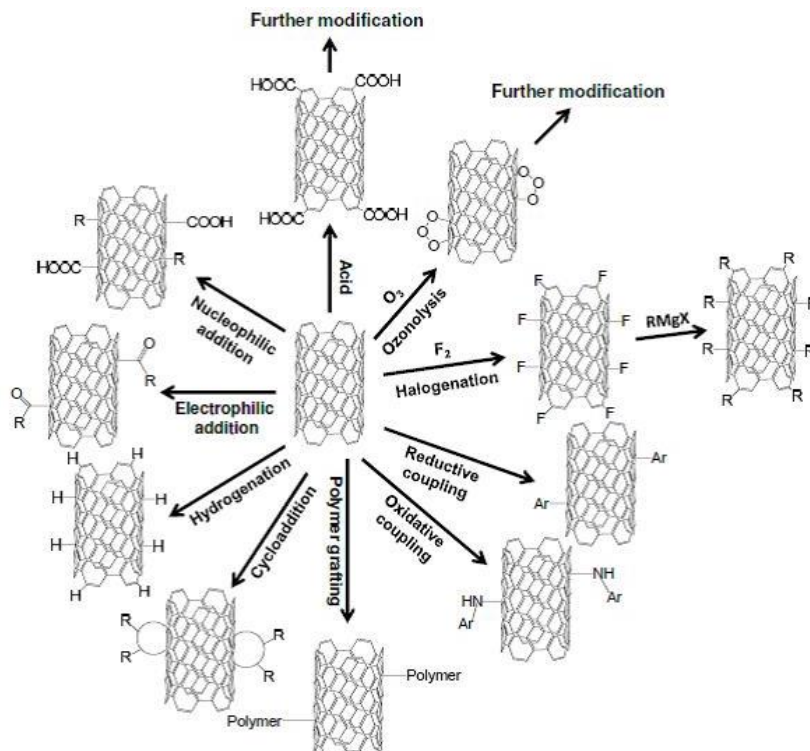
Figure 2.7 – Surface functionalization of CNTs (Wu et al., 2009)

2.3.3. Manufacturing of CNT/PEEK Nanocomposites

Apart from the functionalization, the manufacturing processes influence the dispersion and orientation of CNTs in the matrix. The properties of the

19

nanocomposite are strongly related with the homogeneity of the dispersion of CNTs in the PEEK matrix. If a nonhomogeneous dispersion exists, cracks can initiate around the bundles of the CNTs. In addition to dispersion, orientation of the CNTs is also important. If a uniform orientation is obtained in the axial direction, the modulus and strength in this direction will be higher compared to other directions, then the composite will be transversely isotropic. If the dispersion of the CNTs is uniform in all directions, the modulus and strength of the composite will be the same in all directions, then and the composite will be isotropic. Nanocomposite manufacturing processes are given below for the considered articles.

[1]- Boyer et al., 2012

- Premixing of PEEK powder and MWCNT
- twin-screw co-rotating extruder, @380°C, 400 rpm, torque=11 N.m, feeding rate= 1 kg/h.
- Membrane specimens: hot-pressing of PEEK/MWCNT granulates obtained from the twin-screw extruder, @380°C, $t = 2$ mins
- Tensile specimens: injection molding of PEEK/MWCNT granulates

[2] - Tishkova et al., 2011

- PEEK/CNTs/acetone solution heated to 50°C to evaporate acetone
- PEEK/CNTs/acetone paste compression molded in hydraulic hot press, @400°C, $t = 30$ mins, $P = 0.01$ MPa.

[3] - Jain et al., 2010

- Dry-jet wet-spinning of fibers
- PEK-g-MWCNT/PPA solution placed into barrel (28 mm internal diameter)
- Solution extruded through a single-hole spinneret of 120 mm diameter equipped with filter (mesh size was 20 mm) and passed through distilled water coagulation bath (1.2 m long, at room temperature)

- Fibers immersed in water for several days to remove the residual PPA and the bath water periodically replaced with fresh water
- Fibers drawn at various draw ratios @ 200°C

[4] - Zhang et al., 2012

- Melt mixing

[5] - Mohiuddin and Hoa, 2011

- CNT mixed with PEEK
- Melting and high temperature shear mixing, @380°C, $\omega = 100$ rpm, $t = 20$ min
- CNT/PEEK melt compression molded, @340°C, $P = 10$ tons, $t = 15$ min, round shaped samples having 25.4 mm diameter and 1.4 mm thickness

[6] - Li and Zhang, 2011

- PEEK dried in a dehumidifier, @160°C, $t = 10$ h
- CF dried in a dehumidifier, @1000°C, $t = 2$ h
- PEEK mixed with CF with different weight percentage (5, 10, 15, 20) in a batch mixer, @340°C, $t = 30$ min
- compounds dried in a dehumidifier, @160°C, $t = 2$ h
- samples compression molded, @350°C, $P = 15$ MPa, $t = 15$ min

[7] - Guehenec et al., 2013

- PEEK powder dried in an oven, @140°C, $t = 6$ h
- PEEK powder mixed with 3% weight percentage of MWCNT
- Melt compounding performed in a co-rotating twin screw extruder (10 different heating zones, @ 390°C max with varying temperature profile)
- PEEK with 3% wt MWCNTs extruded ($\omega = 100, 150, 200, 300,$ and 400 rpm), feed rate= 1kg/h

21

- Material cooled down in a temperature regulated water bath and then pelletized

- Extruded pellets dried in air, @140°C

- Pellets compression molded for the rheological measurements, @380°C, disks with a diameter of 25 mm and a thickness of 2 mm

- Thin films hot pressed, @380°C, $P = 40$ bars, $t = 2$ min, pellets with a thickness of 150 μm and 10 cm in diameter

- Films cooled down below the T_g, $t = 3$ mins

[8] – Hwang et al., 2013

- GO, MWCNT, and PEEK powders dried overnight, @80°C

- fillers were premixed with anhydrous DMF (Dimethylformamide) using an ultrasonicator, @room temperature, t=1h

- Premixed GO and MWCNT (or functionalized GO and MWCNT) added into PEEK

- Mixture dispersed in the ultrasonicator, followed by stirring continuously, @65°C, $t = 8$ h. Chemical reaction between the chlorinated GO and amine-treated MWCNT achieved

- Slurry dried in an oven, @100°C, $t =$ overnight

- hot press to fabricate the circular disk at an average, heating rate= 5°C/min, @340°C, then hot pressed @340°C, $P = 15$MPa, $t = 10$ min

- cooled to below the glass transition temperature of PEEK

[9] - Ashrafi et al., 2012

- PEEK resin melt-blended SWCNT (wrapped in polysulfone and unwrapped)

- Extruded PEEK/SWCNT pellets used to fabricate films, $t = 0.5$ mm

- Films made using a hot-press, @380°C, $P = 5 - 40 - 130$ bars, $t = 6$ min at each pressure

- Hot compression of alternating layers of PEEK films and GF fabric sheets, @380°C, $t = 20$ mins

- the edges of the laminates trimmed to 150x150 mm, after ultrasonic and thermographic inspection, laminates cut into pieces of approximately 10x10 mm.

[10] - Ogasawara et al., 2011

- PEEK/CNT master batches using a twin-screw extruder, @380°C

- Injection molding, @180°C

- Annealing, @230°C, $t = 5$h

- Cooled to room temperature to reduce thermal stress and to improve the degree of crystallinity, $t = 20$ h

Different manufacturing methods, procedures, temperature, pressures, durations etc. are applied for each reference as seen from the above comparison. Therefore, it is reasonable to have different PEEK/CNT interface, dispersion, orientations and properties for each manufactured composite.

2.3.4. Structural Characterization of CNT/PEEK Nanocomposites

Different characterization methods are used to investigate the structure of the produced material. Raman Spectroscopy (RS), Transmission Electron Microscopy (TEM), Scanning Electron Microscopy (SEM), Fourier Transform-Infra Red (FT-IR), Focused Ion Beam Microscopy (FIBM), Dynamic Mechanical Analyzer (DMA), Dynamic Dielectric Spectroscopy (DDS), Differential Scanning Calorimeter (DSC), Thermo-Gravimetric Analysis (TGA), Laser Flash Analyzer (LFA) are extensively used characterization methods. Some conventional methods are also used for nanocomposite characterization; strain gage, extensometer, multi-meter, ring on block friction test, thermocouple etc. The material, mechanical, thermal and electrical characterization methods for the PEEK/CNT nanocomposite for each reference are provided in Table 2.5. But only material characterization

methods are detailed for some references further in below paragraphs. In the next chapter, mechanical properties are investigated.

Table 2.5 *– List of structural characterization methods used in the references*

	material char. methods	instruments for mechanical property char.	instruments for thermal property char.	instruments for electrical property char.
[1]	…	strain gage, extensometer, DMA	DSC	DDS
[2]	RS, TEM	…	…	broadband spectrometer
[3]	X-ray, RS, SEM, HR-TEM	DMA	TGA	point probe with source meter
[4]	SEM	…	TGA	…
[5]	…	…	thermocouple	multi meter
[6]	FE-SEM	ring on block friction test	…	…
[7]	TEM, RS	…	…	electrometer
[8]	FT-IR, FE-SEM, X-ray	DMA	TGA, DSC, LFA	…
[9]	ultrasonic C-scan, optical microscopy, SEM	short beam shear strength	DSC, thermography	source meter
[10]	SEM, FIBM	extensometer, DMA	…	…

[2] - Tishkova et al., 2011

Tishkova et al. (2011) provided the TEM images of 0.8% weight percentage DWCNT/PEEK composite. Figure 2.8(a) shows DWCNT agglomeration in the PEEK matrix with higher magnification in Figure 2.8(b). Several residual catalyst particles (black dots) are also seen. The TEM images reveal an inhomogeneous dispersion of CNTs in the matrix.
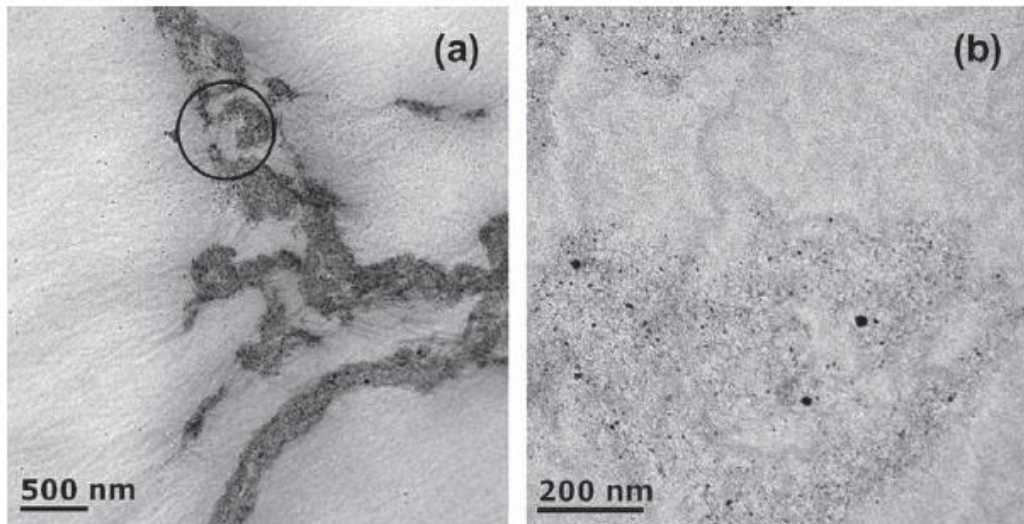
***Figure 2.8** – (a) TEM image of 0.8 wt% DWNTs/PEEK composites. (b) Higher magnification view (Tishkova et al., 2011)*

[3] - Jain et al., 2010

Jain et al. (2010) provided the cross-sectional SEM images of PEK and various PEK-g-MWCNT composite fibers, see Figure 2.9. It can be noted that PEK-g-20% MWCNT fiber shows highly porous structure while the other fibers appear to have relatively flat cross sections.

[9] - Ashrafi et al., 2012

Ashrafi et al., (2012) investigated the effects of the CNT addition on the density and porosity content of glass fiber reinforced PEEK. The weight fractions of the composite laminate types are summarized in Table 2.6. It can be seen that they acquired higher density for the modified composites than the pure PEEK/GF. They

said that composites with SWCNT wrapped in the compatibilizer (PEES) exhibit the highest density values.
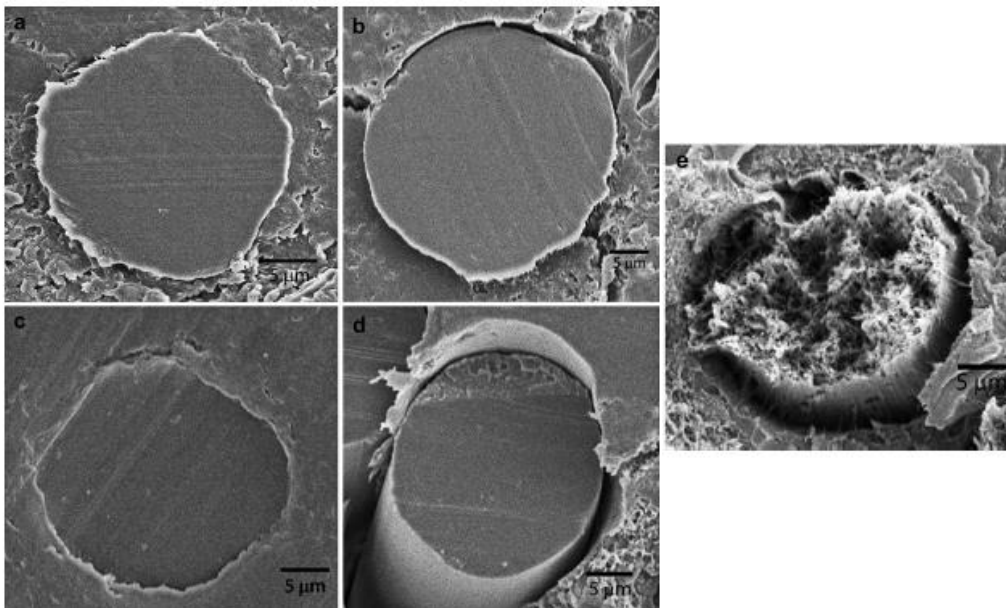
Figure 2.9 – Cross-sectional SEM images of (a) PEK, (b) PEK-g-1% MWCNT, (c) PEK-g-5% MWNT, (d) PEK-g-10% MWCNT, and (e) PEK-g-20% MWCNT fibers (Jain et al., 2010)

Table 2.6 - Resin/fiber weight fraction, density, porosity of manufactured laminates (Ashrafi et al., 2012)

Laminates	Resin/fiber weight fraction [%]	Density [g/cm³]	Porosity [%]
PEEK/GF	36.0/64.0 ± 0.4	1.78 ± 0.02	5.3 ± 1.2
PEEK/PEES/GF	36.1/63.9 ± 0.3	1.78 ± 0.02	5.0 ± 1.2
PEEK/arc SWCNT (1.0 wt.%)/GF	35.9/64.1 ± 0.2	1.81 ± 0.02	3.4 ± 0.8
PEEK/laser SWCNT (1.0 wt.%)/GF	35.4/64.6 ± 0.5	1.84 ± 0.02	2.2 ± 1.3
PEEK/arc SWCNT (1.0 wt.%) + PEES/GF	35.9/64.1 ± 0.5	1.85 ± 0.01	1.3 ± 0.5

PEEK/laser SWCNT (0.5 wt.%) + PEES/GF	*36.0/64.0 ± 0.2*	*1.84 ± 0.01*	*1.6 ± 0.7*
PEEK/laser SWCNT (1.0 wt.%) + PEES/GF	*36.2/63.8 ± 1.0*	*1.86 ± 0.01*	*0.3 ± 0.2*

[10] - *Ogasawara et al., 2011*

As seen from the FIB micrographs in Figure 2.10, by using injection molding, Ogasawara et al. (2011) obtained well aligned CNT dispersion in the longitudinal direction.
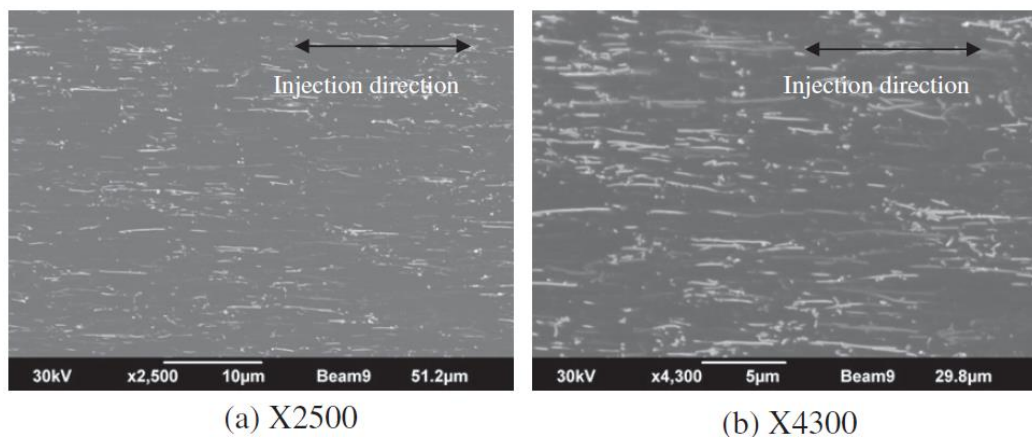
Figure 2.10 - *Focused ion beam (FIB) micrograph of a tensile specimen (Ogasawara et al., 2011)*

As can be seen from the above discussion, various characterization methods are used and there is not a standard procedure for material characterization. Therefore, it is reasonable to expect scatter in the results.

2.3.5. Mechanical Properties of CNT/PEEK Nanocomposites

In the above sections, material properties, interface properties and manufacturing processes are explained. These all affect mechanical, electrical and thermal properties of the nanocomposite. In this section, mechanical properties of the final nanocomposite products for the considered references are given.

[1]- Boyer et al., 2012

As seen from Table 2.7 (Boyer et al., 2012), MWCNT modifies the PEEK properties drastically. By the addition of the MWCNTs, the elastic modulus and the yield strength increase but the ultimate tensile strength decreases. PEEK becomes more brittle and maximum elongation decreases. Note the scatter of the values which is possibly caused from the agglomeration of the CNTs.

Boyer et al. (2012) also investigated dynamic mechanical properties of the PEEK/MWCNT by using DMA, Figure 2.11. They showed that MWCNT increases the storage modulus but the glass transition temperature T_g almost stays constant. They also showed that as MWCNT weight content is increased, loss angle tangent $\tan\delta$ increases to some degree, then starts to decrease. They commented that modification of $\tan\delta$ shows the decrease in the chain mobility of the matrix.

Table 2.7 - Experimental mechanical results for neat PEEK and PEEK/MWCNT
(Boyer et al., 2012)

Material	Neat PEEK	1%wt MWCNT	3%wt MWCNT	5%wt MWCNT
Young's Modulus [MPa]	3678.6 ± 71.3	3703.3 ± 82.9	3774.5 ± 125.1	4145.3
σ_{max} [MPa]	91.8 ± 4.9	83 ± 9.1	80.5 ± 10.8	84.4
ε_{max} [%]	28.6	3.3 ± 1	5 ± 1	2.5
$\sigma @ \varepsilon_x = 0.2\%$ [MPa]	62.2 ± 0.1	60.6 ± 5	60.6 ± 4.6	66

[4] - Zhang et al., 2012

The mechanical properties of PEEK and its nanocomposites in the work of Zhang et al. (2012) are presented in

Table *2.8*. It can be seen that the flexural modulus and the flexural strength are increased while the tensile strength and the elongation at break are decreased with the increasing MWCNT content. After 5% content, the effect of the MWCNT on

the mechanical properties is generally negative.
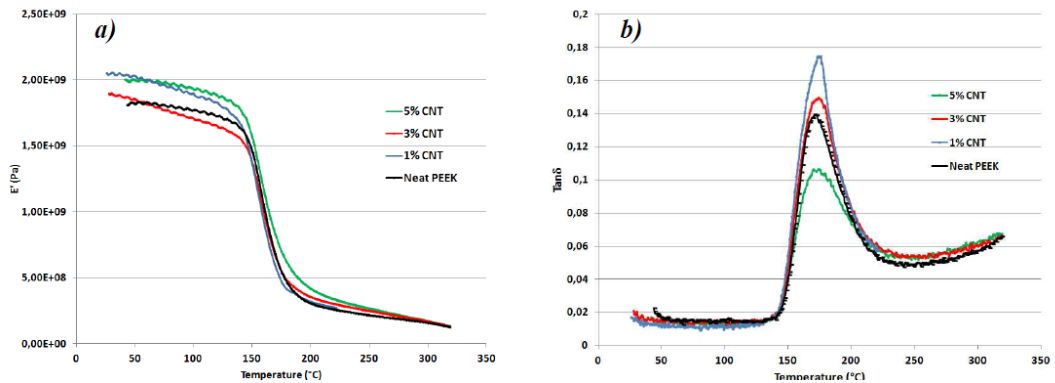
Figure 2.11 – DMA of nanocomposites behavior. a) Storage modulus E' and b) loss angle tangent tan δ as a function of temperature for neat PEEK and PEEK filled with 1, 3 and 5 % wt of MWCNT (Boyer et al., 2012)

Table 2.8 - Mechanical properties of PEEK and CNT/ PEEK composites (Zhang et al., 2012)

Samples	PEEK	MWCNT/ PEEK, 3% / 97%	MWCNT/ PEEK, 5% / 95%	MWCNT/ PEEK, 7% / 93%
Flexural modulus [MPa]	3758	3895	3968	3985
Flexural strength [MPa]	183	188	188	186
Tensile strength [MPa]	107	102	99	96
Elongation at break [%]	27.8	17.2	16.5	15.9

[6] - Li and Zhang, 2011

Figure 2.12 shows the tensile properties of the 20% weight percent carbon fiber in PEEK for varying MWCNT addition (Li and Zhang, 2011). Improvement in the tensile properties of the composite with the increase of MWCNT concentration can be seen clearly. Li and Zhang (2011) said that MWCNTs are warped by the PEEK chains, attached to each other and linked by CF's forming through the system. They commented that this new network acted as a new reinforcement and lead to high

strength and modulus.

Li and Zhang (2011) also investigated the variation in the specific wear rate and the friction coefficient as a function of abrading distance of CF/PEEK and CF/MWCNTs/PEEK composites, see Figure 2.13(a) and (b). As can be seen form the figure, the specific wear rate decreases with increasing abrading distance for both composites. Higher specific wear rate is noticed for the CF/PEEK composite compared to the CF/MWCNTs/PEEK composite. They commented that CF/MWCNTs has high specific strength and reduced ductility compared to CF. The results show that addition of MWCNTs to PEEK increases the tribological properties of the polymer.
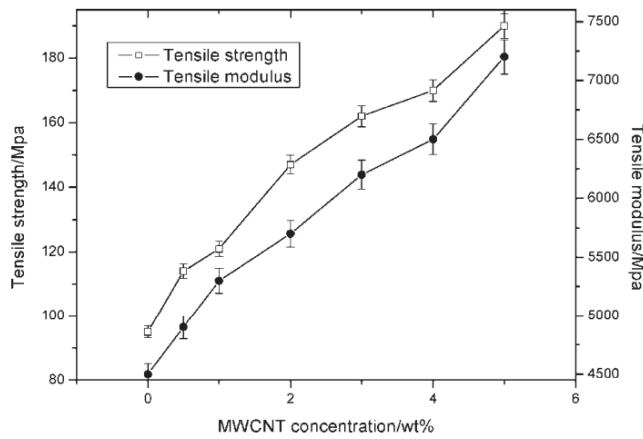
Figure 2.12 – *Tensile properties of MWCNT/ CF/PEEK composite (Li and Zhang, 2011)*
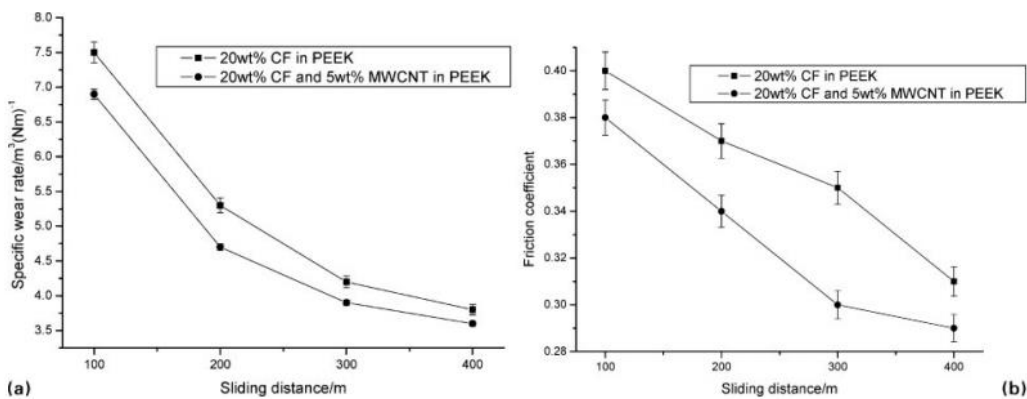
Figure 2.13 – *Friction and wear properties of MWCNT/ CF/PEEK composite (Li and Zhang, 2011)*

[7] - Guehenec et al., 2013

Guehenec et al. (2013) provided the mechanical spectra of PEEK with 3 % weight percentage of CNTs extruded at various screw speeds in Figure 2.14. Note that the insert in this figure shows the spectro-mechanical behavior of the pure PEEK in the same frequency range. They showed that the pure PEEK exhibits a liquid-like behavior while the PEEK with 3% weight percentage MWCNT shows a solid-like behavior. They observed that when MWCNT content increases, a liquid to solid transition at low frequency is observed, which is referred to as the rheological percolation. They also showed that the storage modulus G' and loss modulus G'' are very sensitive to screw speed of the extruder.
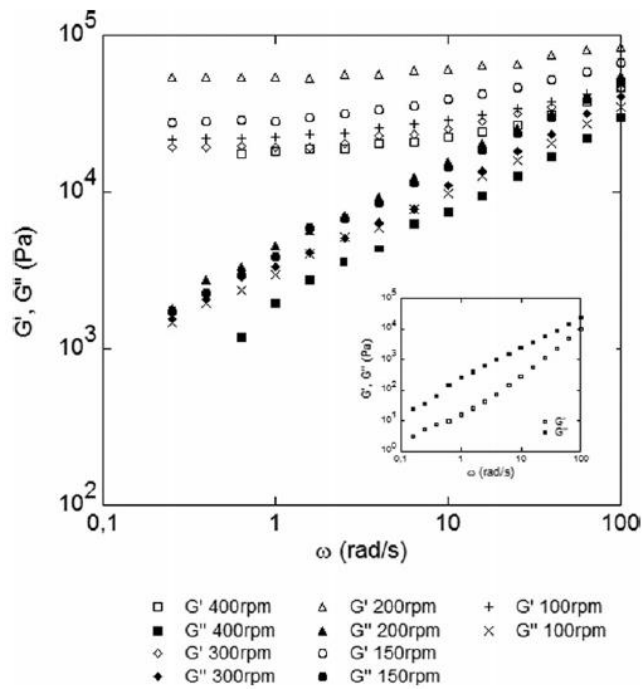
Figure 2.14 – Spectromechanical analysis of PEEK/ 3% MWCNT prepared with several rotor speeds (Guehenec et al. 2013)

[9] - Ashrafi et al., 2012

Ashrafi et al. (2012) investigated the PEEK/GF composites for evaluation of interlaminar properties with the short beam shear test. As shown in Table 2.9, they obtained that in comparison to the PEEK/GF laminate, those incorporating laser

SWCNT with compatibilizer (PEES) shows a 64% and 12% increase in the bending strength for loadings of 1% wt and 0.5% wt, respectively. They showed that for other laminates with arc grown CNTs, either no change or a reduction of bending was measured as compared to the base laminate.

Table 2.9 - Short beam bending strengths of different laminates and their failure modes (Ashrafi et al., 2012)

Laminate composites	Short beam bending strength, [MPa]	Failure modes
PEEK/GF	15.7 ± 1.5	Interlaminar failure in the outermost laminae; compression failure
PEEK/PEES/GF	14.8 ± 1.3	Interlaminar failure in the outermost laminae; compression failure
PEEK/laser SWCNT (1.0 wt.%)/ GF	12.3 ± 2.8	Interlaminar failure in several locations; compression failure (for 2/10 specimens)
PEEK/arc SWCNT (1.0 wt.%) + PEES/GF	11.7 ± 1.4	Interlaminar failure in several locations; inelastic deformation
PEEK/laser SWCNT (0.5 wt.%) + PEES/GF	17.5 ± 1.6	Interlaminar failure in several locations; inelastic deformation; fiber failure (for 2/10 specimens)
PEEK/laser SWCNT (1.0 wt.%) + PEES/GF	25.8 ± 4.3	Interlaminar failure in several locations (mostly in the middle) inelastic deformation; fiber failure (for 5/10 specimens)

[10] - Ogasawara et al., 2011

Ogasawara et al. (2011) showed that as MWCNT percentage increases, the mechanical properties of the nanocomposite increase, see Figure 2.15.
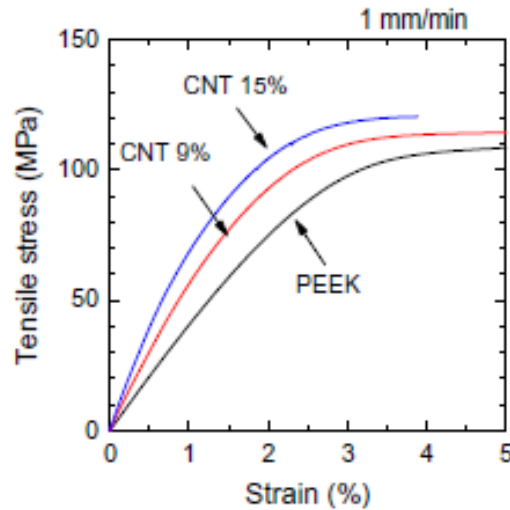
Figure 2.15 – Tensile stress–strain curves of PEEK and CNT/PEEK composites under a constant displacement rate of 1 mm/min (Ogasawara et al., 2011)

Ogasawara et al. (2011) investigated the loading/unloading behavior of the PEEK and the CNT/PEEK composite under a constant loading rate of 1.7 MPa/s, see Figure 2.16. Results are shown for stress ranges of 0–33 MPa and 0–100 MPa in Figure 2.16(a) and (b), respectively. It can be seen that for small stress range, PEEK shows a linear behavior and loading/unloading responses are the same. With the increase in CNT content, the modulus of the CNT/PEEK composite increases. The CNT/PEEK composite shows nonlinear loading/unloading behavior with hysteresis which is an indication of the viscoelastic behavior, Figure 2.16(a). For the larger stress range, the PEEK starts to show nonlinear behavior and hysteresis, Figure 2.16(b). The nonlinearity of the CNT/PEEK composite is increased and the viscoelastic effect is more pronounced for the larger stress range with the addition of CNT.

As seen from the above comparisons from several references, material properties of individual phases, processing of materials, interface properties and manufacturing methods can significantly affect the properties of nanocomposites. To this end, it is

expected to see a big scatter in results from different references. Therefore, for the correct numerical simulation of the composites, the structure of the considered material has to be known, especially the properties of the interface between the CNT and the polymer. Standard manufacturing and test methods have to be developed for the reliable end product.
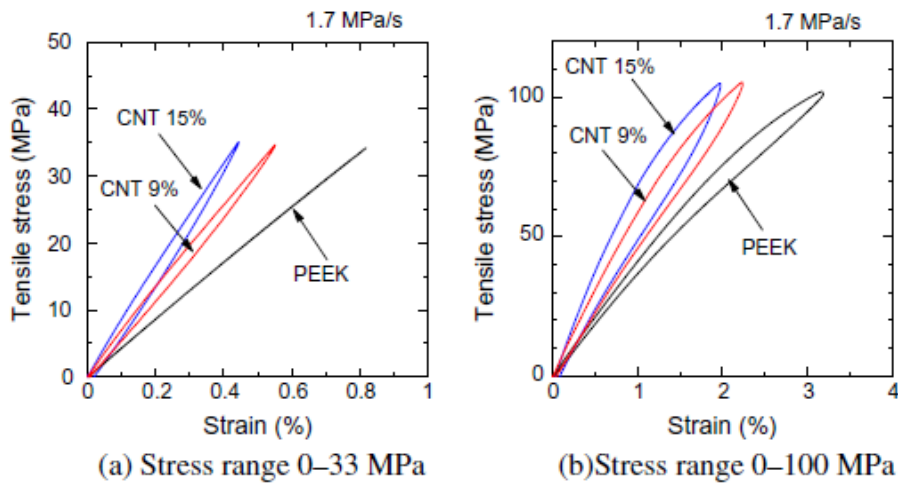
Figure 2.16 – Stress–strain curves of PEEK and CNT/PEEK composites under loading–unloading tensile tests (Ogasawara et al., 2011)

CHAPTER 3

NONLOCAL/GRADIENT ELASTICITY

In classical (local) elasticity, stress at a material point is considered as a local function of the strain at that point:

$$\boldsymbol{\sigma}(x) = \boldsymbol{C} : \boldsymbol{\varepsilon}(x) \tag{3.1}$$

$$\boldsymbol{\varepsilon} = \nabla_s \boldsymbol{u} = \frac{1}{2}(\nabla \boldsymbol{u} + (\nabla \boldsymbol{u})^T) \tag{3.2}$$

where, $\boldsymbol{\sigma}$ is the stress tensor, $\boldsymbol{C}$ is the fourth-order elasticity tensor, $\boldsymbol{\varepsilon}$ is the strain tensor, $\boldsymbol{u}$ is the displacement vector, ∇ is the gradient operator and $(\cdot)^T$ denotes the transpose. Equation (3.1) is applicable to structures in all dimensions from nanometer to meter since the local elasticity theory does not contain any information about the size of the structure. The local elasticity also cannot properly describe stress/strain singularities that may be present in heterogeneous media, crack tips, imperfections etc. (Askes and Aifantis, 2011). When the wavelength of a deformation field and the dominant micro-structural length scale of the material are comparable, the locality assumption is questionable as the material behavior at a point is influenced by the deformation of neighboring points (Forest, 1999). Furthermore, in the local elasticity, mathematical problems and mesh dependence in finite element simulations can be present if strain softening exist (Dreimeier et al., 2005). For nano/microstructures, atomistic simulations can be alternative. However, these simulations are computationally much more expensive than the continuum scale simulations. The time and length scales that can be modeled in atomistic simulations are also limited.

Because of the above reasons, gradient elasticity models have been proposed. The micropolar, micromorphic theories of Cosserat brothers (1909) and the higher order gradient theories of Toupin (1962) and Midlin (1964) are the early versions of the gradient theories. In the Cosserat theory, in addition to the material translational

displacement, $\boldsymbol{u}$, an independent rotational displacement quantity, $\boldsymbol{\theta}$, is defined and couple stresses (bending moment per unit area) are introduced as the work conjugate to the micro-curvature (the spatial gradient of $\boldsymbol{\theta}$). Toupin and Midlin proposed a theory that includes gradients of normal strain. In their review article, Askes and Aifantis (2011) even reported that Cauchy and Voigt studied on gradient theories.

The above theories require many additional material constants to be determined which are not feasible from an experimental point of view. Eringen (1983) and Aifantis (1984) developed further formulations of gradient type theories. Aifantis (1984) proposed a simple model of gradient plasticity for strain softening materials motivated by dislocation dynamics, to determine the width of shear bands. In the beginning of the 1990s, Aifantis proposed another simple model with only one additional constant for use in gradient elasticity (Aifantis, 1992).

In this section, Eringen's nonlocal elasticity and Aifantis's gradient elasticity models are explained in detail. The summation convention is used, that is a subscript index $(i, j, k \dots)$, unless stated otherwise, takes a value of 1-3 and repeated indices imply a summation over 1-3. A small bold character represents a vector, whereas a capital bold character represents a tensor. A Cartesian reference-frame is employed throughout the study.

3.1. ERINGEN'S NONLOCAL ELASTICITY

Compared to the local formulation of elasticity, Eqn. (3.1), the nonlocal formulation is considered to be function of points, $\tilde{x}$, in the neighborhood of the local point x:

$$\boldsymbol{\sigma} = \boldsymbol{\sigma}(x, \tilde{x}) \tag{3.3}$$

This means that long-range forces are applied at a material point. Eringen (1983) proposed an integral formulation for the calculation of nonlocal stress response at a point:

$$\boldsymbol{\sigma}(x) = \int_{\Omega} g(x, \tilde{x}) \, \boldsymbol{C} : \boldsymbol{\varepsilon}(\tilde{x}) \, d\tilde{v} \tag{3.4}$$

where, $\boldsymbol{\sigma}(x)$ is the nonlocal stress, $g(x, \tilde{x})$ is the attenuation (kernel) function defining the nonlocal response of the material which depends on the distance

$|x - \tilde{x}|$. Polizzotto (2001) gave the representations of some attenuation functions as in Figure 3.1. Eringen (2002) proposed to determine g on the basis of a dispersion analysis. Two of the generally used attenuation functions in literature are:

$$g_1(x, \tilde{x}) = \frac{1}{2\ell} e^{-|x - \tilde{x}|/\ell} \tag{3.5}$$

$$g_2(x, \tilde{x}) = \frac{1}{W(x)} e^{-(x - \tilde{x})^2/2\ell^2} \tag{3.6}$$

where, ℓ is the internal characteristic length related with the material internal structure. At the macroscopic level, ℓ can be considered as much smaller than the smallest dimension of the specimen. The internal characteristic length ℓ defines the influence distance of g.
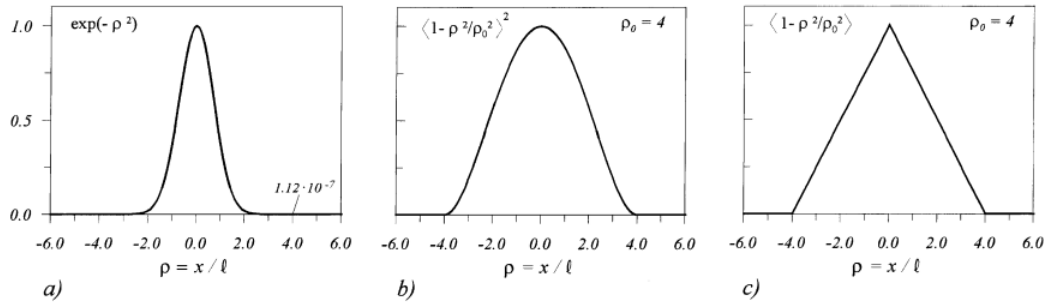
Figure 3.1 *– Plots of the attenuation function g(ρ); (a) error function, (b) bell shape function, (c) conical shape function, (Polizzotto, 2001)*

3.1.1. Attenuation Functions

By considering the attenuation function g_1 of Eqn. (3.5), the effects of the internal length scale parameter, ℓ, and x are shown in Figure 3.2. It can be seen from Figure 3.2(a) that if $\ell \to 0$, g_1 becomes Dirac delta function, $\delta(x - \tilde{x})$, which represents a complete local action. On the contrary, if ℓ increases, g_1 becomes more uniform, representing a nonlocal action and diffusion process. This causes non-zero g values at the boundaries, which means the material response at a point x is affected by the complete material domain. By changing x, the center of the g_1 is changed as seen in Figure 3.2(b).

The terms $1/2\ell$ and $1/W(x)$ in Eqns. (3.5) and (3.6), respectively, are used in order

to normalize the attenuation functions in the integral domain. Note that $1/2\ell$ is a constant term, whereas $1/W(x)$ is a function of the material point. Normality conditions for g_1 and g_2 are given as:

$$\int_{\Omega_\infty} g_1(x, \tilde{x}) dv' = \int_{\Omega_\infty} \frac{1}{2\ell} e^{\left(-\frac{|x - \tilde{x}|}{\ell}\right)} d\tilde{v} = 1 \qquad (3.7)$$

$$\int_{\Omega} g_2(x, \tilde{x}) dv = \int_{\Omega} \frac{1}{W(x)} e^{\left(-\frac{(x - \tilde{x})^2}{2\ell^2}\right)} d\tilde{v} = 1 \qquad (3.8)$$

Note that the integral domains for g_1 and g_2 are Ω_∞ and Ω, respectively. This means that for g_1, the normality condition is fulfilled for infinite domain and it cannot be met for finite domain boundaries. Whereas for g_2, normality condition can be fulfilled in any integral domain by defining $W(x)$ as follows:

$$W(x) = \int_{\Omega} e^{\left(-\frac{(x - \tilde{x})^2}{2\ell^2}\right)} d\tilde{v} \qquad (3.9)$$
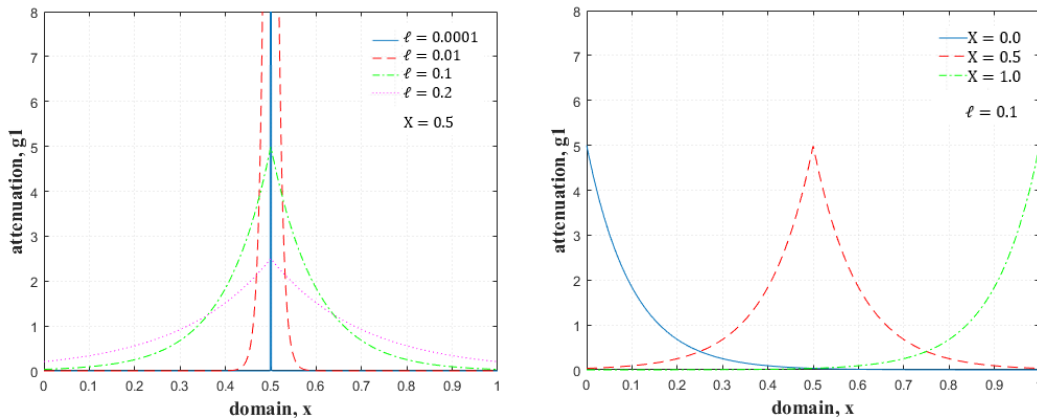
Figure 3.2 *– (a) Effect of ℓ, (b) effect of x on attenuation function g_1*

Figure 3.3 shows g_1 and g_2 curves for a unit volume in one dimension. As can be seen form Figure 3.3(a), the curves are symmetric. Both curves have almost the same peak value and the area under the curves are unity. Figure 3.3(b) shows g_1 and g_2 curves at the boundaries of the domain. Note that the maximum value of g_1 is the same at the boundary as in the middle of the domain and therefore the area under the curve halves. Whereas, the maximum value of g_2 increases at the boundary

compared to the middle and the area under the curve remains unity.

Figure 3.4 shows values of Eqns. (3.7) and (3.8) at every material point in the domain. Although the area under g_2 is constant and equal to unity, the area under g_1 is decreasing towards the domain boundaries. Therefore, if g_1 is used, the calculated field, i.e. σ, will decrease towards the boundaries.
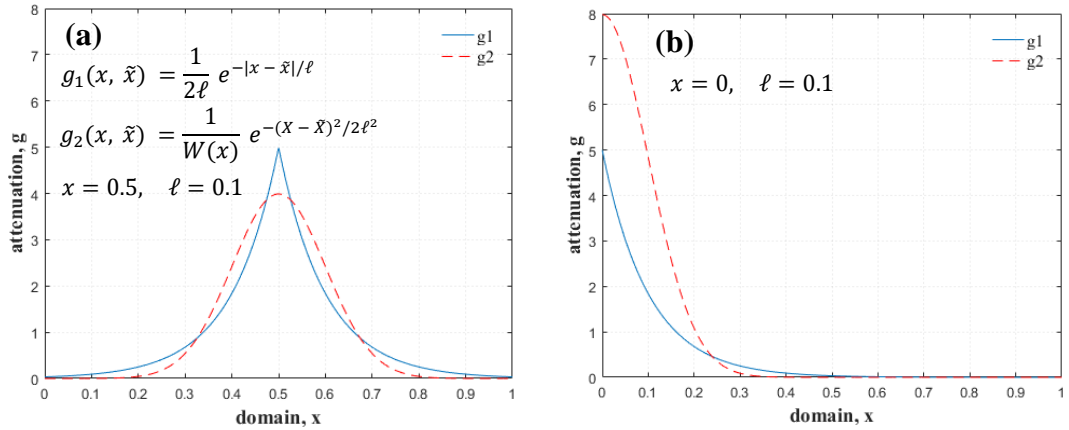
Figure 3.3 –*Attenuation functions g_1 and g_2 for, (a) x=0.5, ℓ=0.1, (b) x=0, ℓ =0.1*
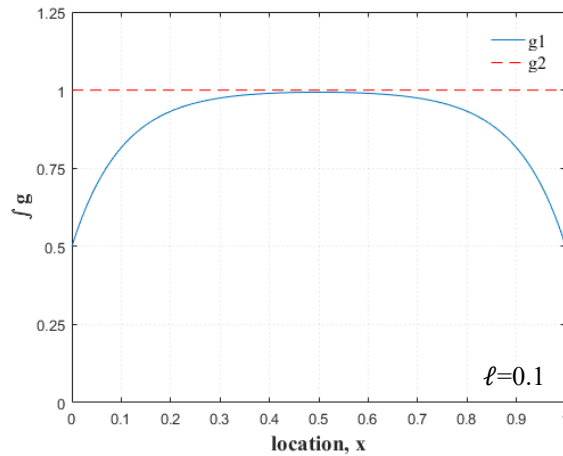
Figure 3.4 – *Area under attenuation functions, g_1 and g_2, for ℓ =0.1*

3.1.2. One-Dimensional Rod under Constant Load

In literature, the kernel function g_1 is used in several studies and the nonlocality at the boundaries is considered; Pisano and Fuschi (2003), Polizzotto et al. (2004), Polizzotto et al. (2006), Benvenuti and Simone (2013), Malagu et al. (2014).

If a 1D rod subjected to a constant load at one end and clamped at the other end, is considered as shown in Figure 3.5, a constant strain and a constant stress is obtained along the rod in the local elasticity. If g_1 is used in Eqn. (3.4) for a 1D rod then one obtains:

$$\bar{\sigma} = \frac{P}{A} = \int_0^L g_1(x, \tilde{x})\, E\varepsilon(\tilde{x})\, d\tilde{x} \qquad (3.10)$$

where, $\bar{\sigma}$ is the constant stress along the rod. It can be observed that a constant strain cannot be achieved along the rod, see Figure 3.6. The non-constant strain is due to the attenuation function considered which ceases to hold the normality condition at the boundaries. The above situation can be avoided by using a different attenuation function, i.e., g_2 in Eqn. (3.6), which fulfills the normality condition in the problem domain rather than in an infinite domain, see Figure 3.6.
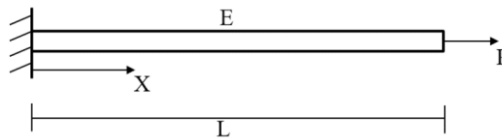
Figure 3.5 *–1D rod under constant end load*
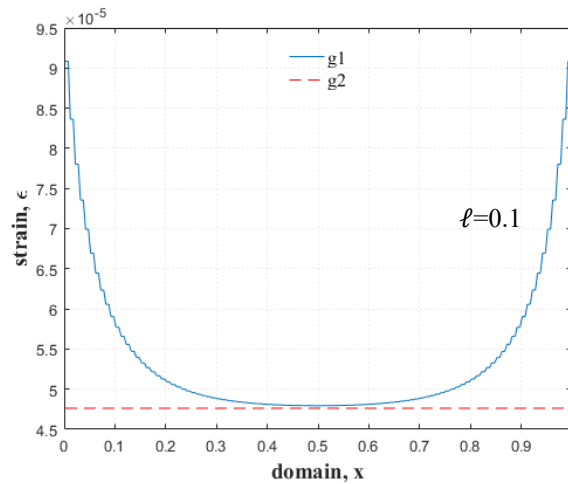
Figure 3.6 *–Strain ε along the rod under constant end load for two different attenuation functions*

3.1.2.1. Alternative Nonlocal Models

In Eringen (2002) another form of Eqn. (3.4) is given:

40

$$\boldsymbol{\sigma}(x) = \xi_1 \boldsymbol{C}:\boldsymbol{\varepsilon}(x) + \xi_2 \int_\Omega g(x,\tilde{x})\,\boldsymbol{C}:\boldsymbol{\varepsilon}(\tilde{x})\,d\tilde{v} \tag{3.11}$$

where, ξ_1 can be considered as the local part and ξ_2 can be considered as the nonlocal part of a two-phase material. When $\xi_1 = 1$ and $\xi_2 = 0$, Eqn. (3.11) reduces to the local formulation given in Eqn. (3.1), and when $\xi_1 = 0$ and $\xi_2 = 1$, Eqn. (3.11) reduces to the original nonlocal formulation given in Eqn. (3.4).

Pisano and Fuschi (2003) considered a bar of uniform cross-section $A = 1$ and finite length L, subjected to a boundary force $F = A\bar{\sigma}$ applied at the end sections so that a uniform tensile stress, $\bar{\sigma}$, is induced in the bar. The bar is made of a nonlocal homogeneous isotropic linear elastic material whose constitutive behavior complies with Eqn. (3.11) in 1D form. Then, Eqn. (3.11) can be modified as:

$$\varepsilon(x) = \frac{\bar{\varepsilon}}{\xi_1} - \frac{\xi_2}{\xi_1}\int_0^L g(x,\tilde{x})\,\varepsilon(\tilde{x})\,d\tilde{x} \tag{3.12}$$

where $\bar{\varepsilon} = \bar{\sigma}/E$. By assuming $g = g_1$ and converting (3.12) to Volterra integral equation of second kind, Pisano and Fuschi (2003) obtained a closed form solution for the strain:

$$\varepsilon(x) = \bar{\varepsilon} - \frac{\lambda l}{2}\bar{\varepsilon}\left[e^{(\lambda x\ell - x)/\ell} + e^{(\lambda\ell L - \lambda\ell x - L + x)/\ell}\right] \tag{3.13}$$

where $\bar{\varepsilon}$ is the uniform strain of the local solution, and $\lambda = -\xi_2/2\ell\xi_1$.

Benvenuti and Simone (2013) also gave the closed form solution in a different format as:

$$\varepsilon(x) = C_1\cosh(\kappa x) + C_2\sinh(\kappa x) + \frac{\bar{\varepsilon}}{\xi_1} - \frac{\kappa_1}{\kappa}(1 - \cosh(\kappa x)) \tag{3.14}$$

where

$$\kappa = \frac{1}{\ell}\sqrt{\frac{\xi_1 + \xi_2}{\xi_1}} \tag{3.15}$$

$$\kappa_1 = \frac{\xi_2\bar{\varepsilon}}{\xi_1^2\ell^2\kappa} \tag{3.16}$$

$$C_1 = C_2\kappa\ell \tag{3.17}$$

41

$$C_2 = \frac{\kappa_1/(\kappa\ell)(1 - \cosh(\kappa L)) - \kappa_1 \sinh(\kappa L)}{\kappa^2 \ell \sinh(\kappa L) + 2\kappa \cosh(\kappa L) + (1/\ell)\sinh(\kappa L)} \quad (3.18)$$

Benvenuti and Simone (2013) also considered some constraints on the values of ξ_1 and ξ_2. They showed that as $\ell \rightarrow 0$, g_1 becomes $\delta(x - \tilde{x})$, and therefore:

$$\xi_1 + \xi_2 = 1 \quad (3.19)$$

They also pointed out that micro/nano structures should behave stiffer than the macro structure, therefore:

$$\xi_1 \geq 1 \quad (3.20)$$

Figure 3.7 shows the analytical solutions of a 1D rod under constant end load by considering strain expressions given in Eqn. (3.13) and Eqn. (3.14), and constraints Eqn. (3.19) and (3.20) for $L = 100$, $\ell = 10$, $\bar{\varepsilon} = 1$, $\xi_1 = 1.5, 0.5$. As seen from Figure 3.7(a), if $\xi_1 > 1$, strain at the boundaries is lower than the strain in the middle, whereas, if $\xi_1 < 1$, the strain at the boundaries is higher than the strain in the middle, Figure 3.7(b). For both cases, strain in the middle of the rod approaches to $\bar{\varepsilon}$. The same problem was also analyzed with series solutions by Abdollahi and Boroomand (2013) and the result was compared with the solution of Pisano and Fuschi (2003). They showed that the solution of Pisano and Fuschi (2003) gives erroneous results. They modified (3.13) by minimizing the difference with the series solutions for some specific values of problem parameters, see Abdollahi and Boroomand (2013) for the details.
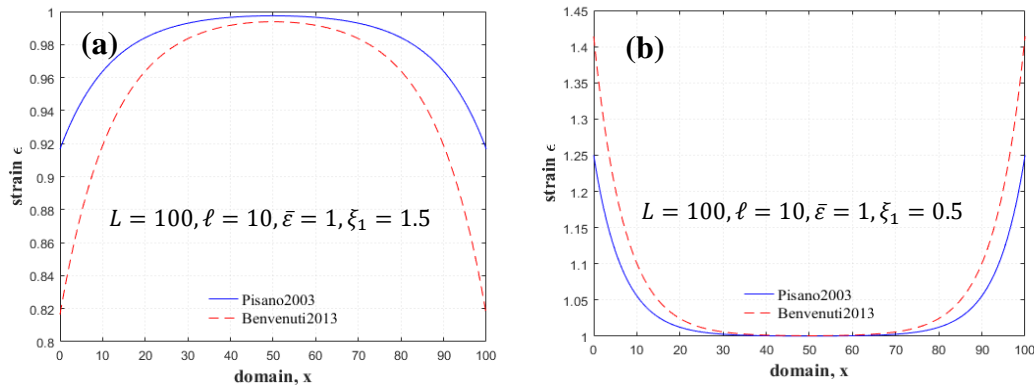
Figure 3.7 – *Analytical solutions of Pisano and Fuschi (2003) and Benvenuti and Simone (2013) for 1D rod under constant end load*

As seen from Figure 3.7, the nonlocal elasticity of the form in Eqn. (3.11) still has the property of decreasing strain towards the boundaries for constant load along the rod. Polizzotto et al. (2004) proposed a new formulation, which eliminates this deficiency. By taking the uniform strain, $\bar{\varepsilon}$, the stress at the boundaries of the domain can be written as:

$$\sigma(x) = W(x)E\bar{\varepsilon} \tag{3.21}$$

where:

$$W(x) = \int_x \frac{1}{2\ell} e^{\left(-\frac{|x - \tilde{x}|}{\ell}\right)} d\tilde{x} \tag{3.22}$$

It can be realized that the undistributed stress at the boundaries can be written as:

$$\sigma(x) = [1 - W(x)]E\varepsilon(x) \tag{3.23}$$

Therefore, the original Eringen model (3.4) can be modified as:

$$\sigma(x) = [1 - W(x)]E\varepsilon(x) + \int_\Omega g_1(x, \tilde{x})E\varepsilon(\tilde{x}) \, d\tilde{v} \tag{3.24}$$

The above equation implies that, in the inner domain where $W(x) = 1$, the local part $[1 - W(x)]E\varepsilon(x)$ does not contribute to stress response whereas at the boundaries, the local part increases to make the stress response constant along the domain. Note that, in Eqn. (3.24), E is constant through the domain, but it can be replaced with $E(x)$ changing through the domain. By comparing Eqn. (3.11) and Eqn. (3.24), it can be shown that Eqn. (3.11) satisfies the constant strain under constant stress condition if $\xi_1 = [1 - W(x)]$ and $\xi_2 = 1$. In Polizzotto et al. (2004), nonlocal formulations for non-homogeneous rods are also proposed.

There have been also some nonlocal models developed particularly for CNTs. Sudak (2003) developed a model for the column buckling of MWCNTs, based on the theory of nonlocal continuum mechanics. Peddieson et al. (2003) provided the Euler beam bending formulations of nonlocal elasticity. Polizzotto et al. (2004, 2006) provided alternative formulations for homogeneous and non-homogeneous 1D rods. Murmu and Pradhan (2009) studied the thermo-mechanical vibration of a single-

walled carbon nanotube embedded in an elastic medium based on nonlocal elasticity theory. Arash and Wang (2012) provided a review on recent studies on the application of the nonlocal continuum theory in modeling of carbon nanotubes and graphene sheets under static and dynamic loadings. Also an introduction to the nonlocal beam, plate, and shell models were given in Arash and Wang (2012). Malagu et al. (2014) investigated the application and performance of high-order approximation techniques to 1D nonlocal elastic rods. They compared the accuracy and convergence rate of the numerical solutions obtained by Lagrange, Hermite, B-spline finite elements and C1 generalized finite elements with the corresponding analytical solutions. Malagu et al. (2015) used an atomistic based nonlocal attenuation function and validated the nonlocal modeling of CNT under axial tensile load by using molecular mechanics approach. They investigated the effects of chirality and size on the results.

3.1.3. Some Remarks

Finite Deformation:

The nonlocal elasticity formulation for large strain framework is basically the same as the small strain formulation. The difference is to choose the strain/deformation measure on which the nonlocality integral will be applied. As an example, Dreimeier et al. (2005) applied large strain nonlocal elasticity for a nonhomogeneous 1D rod.

Thermodynamic Framework:

Discussions of the thermodynamic aspects and restrictions of the nonlocal elasticity can be found in Polizzotto (2001, 2003) and Polizzotto et al. (2006). He commented that, because the internal energy density at a point is dependent on the strain field in the nonlocal elasticity, the principle of local action of thermodynamics does not hold, and therefore the first principle of thermodynamics can only be written for the whole body.

Variational Formulation and FE Modeling:

Variational formulation and FE modeling of the nonlocal elasticity are provided in Polizzotto (2001) and Polizzotto et al. (2006) by considering the total potential energy. Polizzotto (2001) also provided variational formulations based on the complementary energy and the Hu-Washizu principle.

3.2. AIFANTIS'S STRAIN GRADIENT ELASTICITY

In the gradient elasticity, stress at a material point is not only a function of the strain but also function of the higher order derivatives of displacement, strain or stress. The strain gradient form can be given as:

$$\boldsymbol{\sigma} = \widehat{\boldsymbol{\sigma}}(\boldsymbol{\varepsilon}, \nabla^2 \boldsymbol{\varepsilon}) \tag{3.25}$$

where ∇^2 is the Laplacian, i.e., $\nabla^2 \boldsymbol{\varepsilon}$ denotes the divergence of the gradient of $\boldsymbol{\varepsilon}$. There are also higher order gradient models in literature. Askes et al. (2002) proposed a 4th order strain gradient, $\nabla^4 \boldsymbol{\varepsilon}$, model. They showed that although 2nd and 4th order gradient formulations give similar results in static applications, 4th order model gives more reliable results in dynamic applications at higher wave numbers. The strain gradient form of the gradient elasticity is given as (Altan and Aifantis, 1992):

$$\sigma_{ij} = C_{ijkl}(\varepsilon_{kl} - l^2 \nabla^2 \varepsilon_{kl}) \tag{3.26}$$

or, alternatively:

$$\sigma_{ij} = C_{ijkl}(1 - l^2 \nabla^2)\varepsilon_{kl} \tag{3.27}$$

where, ℓ is the internal length scale related with the material microstructure that can be linked to the inter particle distance in discrete models, grain size, etc. By assuming $\sigma_{ij}^0 = C_{ijkl}\varepsilon_{kl}$, the stress gradient form of the Aifantis model can be written as

$$\sigma_{ij} = \left(\sigma_{ij}^0 - l^2 \nabla^2 \sigma_{ij}^0\right) \tag{3.28}$$

where σ_{ij}^0 is the stress tensor in local elasticity. By considering $\varepsilon_{kl} = 1/2(u_{k,l} + u_{l,k})$ and the symmetry conditions of C_{ijkl}, the displacement gradient form of the Aifantis model can be written as:

$$\sigma_{ij} = C_{ijkl}(u_{k,l} - l^2\nabla^2 u_{k,l}) \tag{3.29}$$

In (3.26), C_{ijkl} is given as:

$$C_{ijkl} = \lambda\delta_{ij}\delta_{kl} + \mu(\delta_{ik}\delta_{jl} + \delta_{il}\delta_{jk}) \tag{3.30}$$

where, λ, μ are the Lamé constants and δ is the Kronecker delta. By inserting (3.30) into (3.26), stress can be written as:

$$\sigma_{ij} = \lambda\varepsilon_{kk}\delta_{ij} + 2\mu\varepsilon_{kl} - l^2\nabla^2(\lambda\varepsilon_{kk}\delta_{ij} + 2\mu\varepsilon_{kl}) \tag{3.31}$$

In tensor notation, (3.31) is written as:

$$\boldsymbol{\sigma} = \lambda\,\mathrm{tr}(\boldsymbol{\varepsilon})\mathbf{1} + 2\mu\boldsymbol{\varepsilon} - l^2\nabla^2(\lambda\,\mathrm{tr}(\boldsymbol{\varepsilon})\mathbf{1} + 2\mu\boldsymbol{\varepsilon}) \tag{3.32}$$

where, $\mathrm{tr}(.)$ is the trace operator and $\mathbf{1}$ is the 2nd order identity tensor. By considering the static equilibrium equation $\sigma_{ij,j} + b_i = 0$, (3.26) can be written as:

$$\frac{1}{2}C_{ijkl}\left(u_{k,lj} + u_{l,kj} - l^2(u_{k,lj} + u_{l,kj})_{,mm}\right) + b_i = 0 \tag{3.33}$$

where, b_i is the body load per unit volume. Because of the symmetry of the strain tensor, (3.33) can also be written as:

$$C_{ijkl}\left(u_{k,lj} - l^2(u_{k,ljmm})\right) + b_i = 0 \tag{3.34}$$

or, in tensor notation

$$\boldsymbol{C}:(\boldsymbol{u}'' - l^2\boldsymbol{u}'''') + \boldsymbol{b} = \boldsymbol{0} \tag{3.35}$$

3.2.1. Variational Formulation and FE modeling

The strain energy density for a linear gradient material is given by:

$$w = \frac{1}{2}\varepsilon_{ij}C_{ijkl}\varepsilon_{kl} + \frac{1}{2}l^2\varepsilon_{ij,m}C_{ijkl}\varepsilon_{kl,m} \tag{3.36}$$

$$= \frac{1}{2}\varepsilon_{ij}C_{ijkl}\varepsilon_{kl} + \frac{1}{2}l^2\eta_{ijm}C_{ijkl}\eta_{klm}$$

The stress tensor σ_{ij} and the higher order stress tensor (double stress) μ_{ijm} can be obtained by differentiating Eqn. (3.36) with respect to ε_{ij} and η_{ijm}, respectively:

$$\sigma_{ij} = \frac{\partial w}{\partial \varepsilon_{ij}} = C_{ijkl}\varepsilon_{kl} = \sigma_{ji} \tag{3.37}$$

$$\mu_{ijm} = \frac{\partial w}{\partial \eta_{ijm}} = \ell^2 C_{ijkl}\eta_{klm} = \ell^2 C_{ijkl}\varepsilon_{kl,m} = \ell^2\sigma_{ij,m} = \mu_{jim} \tag{3.38}$$

The total potential energy in 3D can be given as (Lam et al. 2003, Gao and Park, 2007, Papanicolopulos et al. 2009, Zibaei et al. 2014, Rudraraju et al. 2014, Zhou et al. 2016):

$$\Pi(\boldsymbol{u}) = \frac{1}{2}\int_{\Omega}(\boldsymbol{\sigma}:\boldsymbol{\varepsilon} + \boldsymbol{\mu}:\boldsymbol{\eta})dv - \int_{\Omega}\boldsymbol{b}\cdot\boldsymbol{u}dv$$
$$- \int_{\Gamma}(\boldsymbol{t}\cdot\boldsymbol{u} + \boldsymbol{q}\cdot\boldsymbol{Du})da - \int_{\Upsilon}\boldsymbol{r}\cdot\boldsymbol{u}dc \tag{3.39}$$

where, $\boldsymbol{\sigma}$ is the Cauchy stress, $\boldsymbol{\mu}$ is the double stress, $\boldsymbol{b}$ is the body load, $\boldsymbol{t}$ is the traction, $\boldsymbol{q}$ is the higher order traction, $\boldsymbol{u}$ is the displacement, $\boldsymbol{Du}$ is the normal derivative of the displacement, $\boldsymbol{r}$ is the line load. For clarity reasons, variational formulation and FE modeling of Aifantis model in 1D are provided below. For a 1D problem, σ and μ can be written as:

$$\sigma = E\varepsilon = Eu' \qquad \text{and} \qquad \mu = l^2E\eta = l^2E\varepsilon' = l^2Eu'' \tag{3.40}$$

where E is the Young's modulus. The first variation of the potential energy can be written as:

$$\delta\Pi(\boldsymbol{u}) = \frac{1}{2}\int_{\Omega}(\boldsymbol{\sigma}:\delta\boldsymbol{\varepsilon} + \boldsymbol{\mu}:\delta\boldsymbol{\eta})dv - \int_{\Omega}\boldsymbol{b}.\delta\boldsymbol{u}dv$$
$$- \int_{\Gamma}(\boldsymbol{t}.\delta\boldsymbol{u} + \boldsymbol{q}.\delta\boldsymbol{Du})da - \int_{\Upsilon}\boldsymbol{r}.\delta\boldsymbol{u}dc \tag{3.41}$$

The line integral in Eqn. (3.39) vanishes for 1D formulation and the boundary integral reduces to nodal forces. Then, the first variation of the total potential energy in 1D is expressed as:

$$\delta\Pi(u) = \frac{1}{2}\int_L (\sigma\delta\varepsilon + \mu\delta\eta)dv - \int_L b\delta u dv - (tA\delta u + qA\delta Du)|_\Gamma \qquad (3.42)$$

Using Eqns. (3.40) in (3.42) gives:

$$\delta\Pi(u)$$

$$= \int_0^L [EAu'\delta u' + l^2 EAu''\delta u'']dx - \int_0^L bA\delta u dx - (tA\delta u + qA\delta Du)|_\Gamma \qquad (3.43)$$

Integration of the higher order term by parts gives:

$$\delta\Pi(u) = \int_0^L [EA(u' - l^2 u''')\delta u']dx + (EAl^2 u''\delta u')|_\Gamma \qquad (3.44)$$

$$- \int_0^L bA\delta u dx - (tA\delta u + qA\delta Du)|_\Gamma$$

Integrating the first integral by parts gives:

$$\delta\Pi(u) = -\int_0^L [EA(u'' - l^2 u'''') + bA]\delta u dx \qquad (3.45)$$

$$+[EAl^2 u''\delta u' + EA(u' - l^2 u''')\delta u]|_\Gamma - (tA\delta u + qA\delta Du)|_\Gamma$$

In equilibrium, the first variation vanishes:

$$\delta\Pi(u) = 0 \qquad (3.46)$$

Eqn. (3.46) holds for any δu and $\delta u'$. Consequently, the equilibrium equation and the boundary conditions are obtained:

$$E(u'' - l^2 u'''') + b = 0 \qquad\qquad \forall x \in [0, L] \qquad (3.47)$$

$$E(u' - l^2 u''') = \bar{t} \qquad\qquad \text{on } \Gamma_t$$
$$\qquad\qquad\qquad\qquad\qquad\qquad\qquad\qquad (3.48)$$
$$u = \bar{u} \qquad\qquad \text{on } \Gamma_u$$

$$El^2 u'' = \bar{q} \qquad\qquad \text{on } \Gamma_q$$
$$\qquad\qquad\qquad\qquad\qquad\qquad\qquad\qquad (3.49)$$
$$u' = \overline{Du} = \bar{u}' \qquad\qquad \text{on } \Gamma_{Du}$$

where Γ_u and Γ_t are the boundaries on which axial displacements and tractions are prescribed, respectively. Γ_{Du} and Γ_q are the boundaries on which normal strains and double tractions are prescribed, respectively. In particular, $\Gamma_u \cup \Gamma_t = \Gamma$, $\Gamma_u \cap \Gamma_t = 0$, $\Gamma_{Du} \cup \Gamma_q = \Gamma$ and $\Gamma_{Du} \cap \Gamma_q = 0$ must hold. From Eqns. (3.47)-(3.49), it is worth

noting that, beside the prescribed axial forces, tA, and displacements, u, either double axial force, qA, or the axial strain, u', need to be specified at the boundary. It must be noted that, in gradient elasticity higher order stress or strain are required. Imposing $\delta\Pi = 0$, Eqn. (3.43) can be rewritten as:

$$\boldsymbol{K}\boldsymbol{u} = \boldsymbol{f} \qquad (3.50)$$

where, $\boldsymbol{K}$ is the stiffness tensor and $\boldsymbol{f}$ is the force vector:

$$\boldsymbol{K} = \overset{n_{el}}{\underset{e\,=\,1}{A}} \int_{x_1^e}^{x_2^e} \left(\boldsymbol{B}^T EA\boldsymbol{B} \ + \ l^2 \frac{d\boldsymbol{B}^T}{dx} EA \frac{d\boldsymbol{B}}{dx} \right) dx \qquad (3.51)$$

$$\boldsymbol{f} = \overset{n_{el}}{\underset{e\,=\,1}{A}} (\boldsymbol{f}_\Omega^e + \boldsymbol{f}_\Gamma^e) \ = \ \overset{n_{el}}{\underset{e\,=\,1}{A}} \left[\int_{x_1^e}^{x_2^e} \boldsymbol{N}^T bA dx \ + \ (\boldsymbol{N}^T tA - \boldsymbol{B}^T qA)|_\Gamma \right] \qquad (3.52)$$

where, $\boldsymbol{B}$ matrix includes the derivatives of the shape functions. Detailed FE formulation can be found in Shu et al. (1999), Papanicolopulos et al. (2009). The numerical approximation of u should be C^1-continuous within the domain because of the higher order derivative of u. The standard C^0 basis functions, such as Lagrangian basis functions, cannot be employed. Hermite and B-spline basis functions can be used to satisfy such continuity requirement, (Malagu et al., 2014). Alternatively, mixed finite element formulations, which require only C^0-continuity, can be employed (Askes and Gutierrez, 2006).

3.2.2. Staggered Gradient Elasticity

The gradient elasticity formulations include higher order derivatives of displacements, strains, stresses etc. Therefore, a higher order continuity, C^1 at least, of shape functions is required in finite element formulation. Askes et al. (2008) summarized the methods that fulfill this continuity requirement:

- Hermite polynomials and B-spline shape functions can be used (Malagu et al. 2014)

- Mixed finite elements can be used (Askes and Gutierrez, 2006)

- Meshless methods can be used

- Penalty methods can be used

- Continuous/discontinous Galerkin methods can be used

All of the above methods have their advantages and disadvantages. With respect to C^0 Laplacian finite elements, the main disadvantages of the above methods are computational burden, implementation difficulties and stability issues. Another way of implementing gradient elasticity is to change the problem formulation. In the staggered gradient elasticity, 4th order differential equation is rewritten as a two set of 2nd order differential equation which reduces the continuity requirement to C^0. Then, the 2nd order equations can be solved consecutively. There are displacement, strain and stress formulations of the staggered gradient elasticity as in the standard gradient case. Reader can refer to the reference Askes et al. (2008) for further details.

3.2.3. Sign of the gradient term in Aifantis Gradient Elasticity

Askes et al. (2002) considered two different second order gradient elasticity models. One is the usual Aifantis model:

$$\boldsymbol{\sigma} = \boldsymbol{C} : (\boldsymbol{\varepsilon} - l^2 \nabla^2 \boldsymbol{\varepsilon}) \qquad (3.53)$$

and the other is:

$$\boldsymbol{\sigma} = \boldsymbol{C} : (\boldsymbol{\varepsilon} + l^2 \nabla^2 \boldsymbol{\varepsilon}) \qquad (3.54)$$

They obtained Eqn. (3.54) with the homogenization of a discrete system with a Taylor Series expansion. They considered Eqn. (3.53) as phenomenological, but (3.54) as microstructural because it is developed from a discrete microstructure. They showed that the analytical solution of Eqn. (3.53) is exponential type, smoothing the heterogeneities in the strain field, whereas Eqn. (3.54) is harmonic type introducing heterogeneities in the strain field as shown in Figure 3.8.
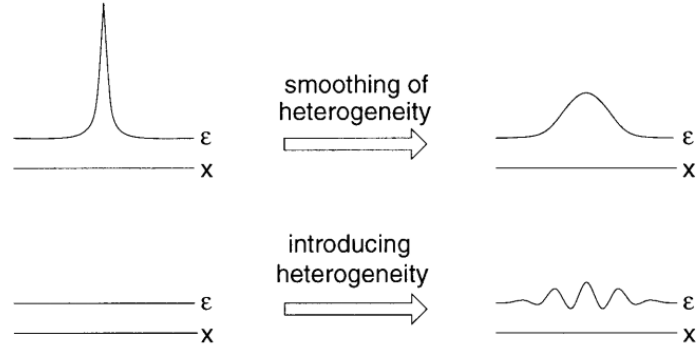
Figure 3.8 *–Two motivations for using higher-order gradients: smoothing or regularization of heterogeneities in the strain field (top) and the introduction of heterogeneities in the strain field (bottom), Askes et al. (2002)*

They commented that Eqn. (3.53) has a stable and unique solution, but has no physical basis because of the unmatched dispersion relations with the discrete model. On the other hand, Eqn. (3.54) has a physical basis but it is conditionally stable and may give non-unique results.

Askes et al. (2002) also introduced a fourth order gradient elasticity as an extension to Eqn. (3.54) which is derived from the homogenization of the microstructure:

$$\sigma = E(\varepsilon + \frac{1}{12}d^2\frac{\partial^2\varepsilon}{\partial x^2} + \frac{1}{12}d^4\frac{\partial^4\varepsilon}{\partial x^4} + \cdots) \qquad (3.55)$$

where d is the inter-particle distance. By omitting, the fourth order term and taking $d = l\sqrt{12}$, Eqn. (3.54) can be reproduced. They showed that that the 4th order model has the physical microstructural basis of the model Eqn. (3.54), and stability and uniqueness properties of the model Eqn. (3.53).

3.2.4. Relation to Eringen's Nonlocal Elasticity

Remember the Eringen nonlocal formulation of stress, Eqn. (3.4):

$$\sigma_{ij}^g(x) = \int_V g(x,t)\sigma_{ij}^c(\tilde{x})dV \qquad (3.56)$$

where, σ_{ij}^g is the nonlocal stress tensor, $\sigma_{ij}^c(t)$ is the local stress tensor and g is the attenuation function. It was shown in Eringen (1983) that the integral Eqn. (3.56) can be simplified to the following differential equation:

$$\sigma_{ij}^g - \ell^2 \sigma_{ij,kk}^g = \sigma_{ij}^c \qquad (3.57)$$

A similar stress based formulation can also be written for Aifantis model, Eqn. (3.28). Askes and Aifantis (2011) and Askes and Gitman (2010) explained the difference between the two formulations by comparing the balance equations. They explained that the Eringen model uses σ_{ij}^g for the equilibrium whereas the Aifantis model uses σ_{ij}^c for the equilibrium:

$$\sigma_{ij,j}^g + b_i = 0 \qquad \text{(Eringen)} \qquad (3.58)$$

$$\sigma_{ij,j}^c + b_i = 0 \qquad \text{(Aifantis)} \qquad (3.59)$$

Because the Aifantis model is uncoupled, it is simpler to implement. Askes and Gitman (2010) commented that the Eringen model was developed for dynamics, whereas the Aifantis model was developed for statics. They also compared wave dispersion results of both model with discrete lattice model results, and showed that the Eringen model is better suited for dynamic applications.

It was stated in Aifantis (2011) that by starting with an implicit constitutive equation of the form $f(\boldsymbol{\varepsilon}, \boldsymbol{\sigma}, \nabla^2\boldsymbol{\varepsilon}, \nabla^2\boldsymbol{\sigma}) = 0$ and assuming f is a linear isotropic tensor function of its arguments, the relevant representation theorem for f gives:

$$\text{tr}(\alpha_1\boldsymbol{\varepsilon} + \alpha_2\boldsymbol{\sigma})\mathbf{1} + \alpha_3\boldsymbol{\varepsilon} + \alpha_4\boldsymbol{\sigma} + \nabla^2[\text{tr}(\alpha_5\boldsymbol{\varepsilon} + \alpha_6\boldsymbol{\sigma})\mathbf{1} + \alpha_7\boldsymbol{\varepsilon} + \alpha_8\boldsymbol{\sigma}] = \mathbf{0} \quad (3.60)$$

where α_i are constants. It was stated that the Eringen model $\varepsilon_{ij} = C_{ijkl}^{-1}(1 - c\nabla^2)\sigma_{kl}$, the Aifantis model $\sigma_{ij} = C_{ijkl}(1 - c\nabla^2)\varepsilon_{kl}$, and implicit gradient model $(1 - c_1\nabla^2)\sigma_{ij} = C_{ijkl}(1 - c_2\nabla^2)\varepsilon_{kl}$ can be obtained by the special choices of α_i.

3.2.5. Mindlin Higher Order Gradient Elasticity in Small Strain Limit

The Midlin theory (Mindlin, 1964) is the general form of the gradient elasticity. In this theory, there are three different forms of higher deformation measures in

literature (Polizzotto, 2017, Askes and Aifantis, 2011):

- In Form I, higher order deformation measure is considered as the second gradient of displacement: $\eta_{ijk} = \partial_k \partial_j u_i = u_{i,jk}$

- In Form II, higher order deformation measure is considered as the first gradient of strain: $\eta_{ijk} = \partial_k \varepsilon_{ij} = 1/2(u_{i,jk} + u_{j,ik})$

- In Form III, higher order deformation measure is divided into two parts, the gradient of macroscopic rotation $\chi_{ij} = \frac{1}{2}\epsilon_{jlk}u_{k,il}$ and the symmetric part of the second gradient of macroscopic displacement $\eta_{ijk} = \frac{1}{3}(u_{i,jk} + u_{j,ik} + u_{k,ij})$.

In this study, the strain gradient elasticity of Form II is considered. Further information on different forms can be found in Askes and Aifantis (2011), Polizzotto (2017) and Gusev and Lurie (2017).

In Form II gradient elasticity, the strain energy density w is a function of both strain and strain gradient:

$$w = w(\varepsilon_{ij}, \eta_{ijk}) \qquad (3.61)$$

$$\varepsilon_{ij} = \frac{1}{2}(u_{i,j} + u_{j,i}), \qquad \eta_{ijk} = \varepsilon_{ij,k} = \frac{1}{2}(u_{i,jk} + u_{j,ik}) \qquad (3.62)$$

where, $\boldsymbol{u}$ is the displacement vector, ε_{ij} is the 2nd order strain tensor, η_{ijk} is the 3rd order strain gradient tensor. Note that $\varepsilon_{ij} = \varepsilon_{ji}$ and $\eta_{ijk} = \eta_{jik}$, that is strain gradient is symmetric with respect to first two indices in Form II. It is worth to note that the symmetry condition for Form I formulation is different. In Form I, η_{ijk} is symmetric with respect to last two indices. If a linear gradient elasticity is considered, w is expressed in the general quadratic form (Gusev and Lurie, 2017):

$$w = \frac{1}{2}C_{ijkl}\varepsilon_{ij}\varepsilon_{kl} + B_{ijklm}\varepsilon_{ij}\eta_{klm} + \frac{1}{2}A_{ijklmn}\eta_{ijk}\eta_{lmn} \qquad (3.63)$$

where C_{ijkl}, B_{ijklm} and A_{ijklmn} are the components of the 4th, 5th and 6th order elasticity tensors. In addition to the Cauchy stress σ_{ij}, which is work conjugate of strain tensor ε_{ij}, in the classical theory, the gradient theory also includes a double stress tensor μ_{ijk}, which is work conjugate to the strain gradient η_{ijk}. The stress

tensors σ_{ij} and μ_{ijk} can be obtained by differentiating Eqn. (3.63) with respect to ε_{ij} and η_{ijk}, respectively:

$$\sigma_{ij} = \frac{\partial w}{\partial \varepsilon_{ij}} = C_{ijkl}\varepsilon_{kl} + B_{ijklm}\eta_{klm} \tag{3.64}$$

$$\mu_{ijk} = \frac{\partial w}{\partial \eta_{ijk}} = B_{lmijk}\varepsilon_{lm} + A_{ijklmn}\eta_{lmn} \tag{3.65}$$

The components of the elasticity tensors $\boldsymbol{A}$, $\boldsymbol{B}$ and $\boldsymbol{C}$ obey the conditions (Gusev and Lurie, 2017):

$$C_{ijkl} = C_{klij}, \qquad A_{ijklmn} = A_{lmnijk} \tag{3.66}$$

and strain symmetry conditions (Gusev and Lurie, 2017):

$$C_{ijkl} = C_{ijlk} = C_{jikl}, \quad B_{ijklm} = B_{jiklm} = B_{ijlkm},$$

$$A_{ijklmn} = A_{jiklmn} = A_{ijkmln} \tag{3.67}$$

Since tensors $\boldsymbol{C}$, $\boldsymbol{B}$ and $\boldsymbol{A}$ obey strain symmetry conditions, stresses $\boldsymbol{\sigma}$ and $\boldsymbol{\mu}$ are also symmetric:

$$\sigma_{ij} = \sigma_{ji}, \qquad \mu_{ijk} = \mu_{jik} \tag{3.68}$$

Substituting $\varepsilon_{ij} = (u_{i,j} + u_{j,i})/2$ into constitutive laws Eqns. (3.64) and (3.65) and using symmetry conditions (3.67) one obtains:

$$\sigma_{ij} = C_{ijkl}u_{k,l} + B_{ijklm}u_{k,lm} \tag{3.69}$$

$$\mu_{ijk} = B_{lmijk}u_{l,m} + A_{ijklmn}u_{l,mn} \tag{3.70}$$

By taking into account the symmetry considerations Eqns. (3.66) and (3.67), for a general centrosymmetric isotropic linear elastic solid, the strain energy density can be expressed as (Mindlin 1964, Zhou et al. 2016):

$$w = \frac{1}{2}\lambda\varepsilon_{ii}\varepsilon_{jj} + \mu\varepsilon_{ij}\varepsilon_{ij} + a_1\eta_{ijj}\eta_{ikk} + a_2\eta_{iik}\eta_{kjj}$$

$$+a_3\eta_{iik}\eta_{jjk} + a_4\eta_{ijk}\eta_{ijk} + a_5\eta_{ijk}\eta_{kji} \tag{3.71}$$

where, λ and μ are the classical Lame constants and a_i are the additional material constants of dimension stress times length squared. The derivation of Eqn. (3.71)

from the most general Mindlin form is given in Abali et al. (2015). A discussion on the derivation of higher-order isotropic tensors and their application in the formulation of enhanced continuum models can be found in Suiker and Chang (2000). The stress tensors σ_{ij} and μ_{ijk} for isotropic case can be obtained as:

$$\sigma_{ij} = \frac{\partial w}{\partial \varepsilon_{ij}} = \lambda \varepsilon_{kk} \delta_{ij} + 2\mu \varepsilon_{ij} \tag{3.72}$$

$$\mu_{ijk} = \frac{\partial w}{\partial \eta_{ijk}} = \frac{1}{2} a_1 \left(\delta_{ij}\eta_{kpp} + 2\delta_{jk}\eta_{ppi} + \delta_{ik}\eta_{jpp} \right) + 2a_2 \delta_{jk}\eta_{ipp}$$

$$+ a_3 \left(\delta_{ij}\eta_{ppk} + \delta_{ik}\eta_{ppj} \right) + 2a_4 \eta_{ijk} + a_5 \left(\eta_{kji} + \eta_{jki} \right) \tag{3.73}$$

Polizzotto (2017) provided the conditions on the coefficients of Eqn. (3.73) for the positive definiteness of the strain energy.

Because the requirement of the determination of the additional five elastic constants, Eqn. (3.73) is undesirable from experimental point of view. By imposing some restrictions (further symmetry conditions, deformation modes etc.), the number of the coefficients have been reduced in literature. By assuming that the strain energy is independent of the anti-symmetric part of the rotation gradient, Lam et al. (2003) proposed a strain gradient isotropic elasticity model for couple stresses with only three coefficients. Gusev and Lurie (2015) formulated a simplified isotropic model of strain gradient elasticity with two coefficients. Zhou et al. (2016) proposed that only three material constants are required instead of five coefficients by using hydrostatic-deviatoric and symmetric-antisymmetric decompositions. Polizzotto (2017) classified the gradient elasticity models according to considered number of coefficients as:

- Generalized model (5 independent coefficients)
- Gradient-symmetric model (4 independent coefficients)
- Hemi-collinear model (3 independent coefficients)
- Collinear model (2 independent coefficients)
- Micro-affine model (1 independent coefficient)

Micro-affine model coincides with the generally used Aifantis model when the following identification is made:

$$A_{ijklmn} = \ell^2 \delta_{il} C_{jkmn} \tag{3.74}$$

The strain energy density w of the Aifantis model includes only one additional material constant:

$$w = \frac{1}{2} \lambda \varepsilon_{ii} \varepsilon_{jj} + \mu \varepsilon_{ij} \varepsilon_{ij} + c \left(\frac{1}{2} \lambda \, \eta_{iik} \eta_{jjk} + \mu \, \eta_{ijk} \eta_{ijk} \right) \tag{3.75}$$

where, $c \ (= \ell^2)$ is a constant of length squared. For $c = 0$, Eqn. (3.75) reduces to the classical isotropic linear elasticity. The stress tensors σ_{ij} and μ_{ijk} can be obtained by differentiating (3.75) with respect to ε_{ij} and η_{ijk}, respectively:

$$\sigma_{ij} = \frac{\partial w}{\partial \varepsilon_{ij}} = \lambda \varepsilon_{ll} \delta_{ij} + 2\mu \varepsilon_{ij} \tag{3.76}$$

$$\mu_{ijk} = \frac{\partial w}{\partial \eta_{ijk}} = c \big(\lambda \varepsilon_{ll} \delta_{ij} + 2\mu \varepsilon_{ij} \big)_{,k} = c \sigma_{ij,k} \tag{3.77}$$

Aifantis also (2011) showed that the Aifantis model can be obtained from the Mindlin model by choosing the constants in Eqn. (3.71) as:

$$a_1 = a_2 = a_5 = 0, \qquad a_3 = \lambda c/2, \qquad a_4 = \mu c \tag{3.78}$$

The physical interpretation of the double stress components for Form I and Form II formulations of gradient elasticity are given by Polizzotto (2016, 2017). The variational formulation of the strain gradient elasticity is provided by Gao and Park (2007).

3.2.6. Some Remarks

Discussions for the thermodynamic aspects and restrictions of the gradient elasticity can be found in Polizzotto (2003). He commented that, in local continuum theories, the first principle of thermodynamics is applicable in a pointwise form, and in the gradient theory, the first principle can be enforced only in the whole domain and the long-distance energy interchanges must be taken into account.

In the micromorphic elasticity, the strain energy is written as (Ferretti et al. 2014):

$$W = W(\varepsilon_{ij}, \gamma_{ij}, \eta_{ijk}) \tag{3.79}$$

$$\gamma_{ij} = \varepsilon_{ij} - \varphi_{ij} \qquad (3.80)$$

$$\eta_{ijk} = \varphi_{ij,k} \qquad (3.81)$$

where, γ_{ij} is the relative deformation, φ_{ij} micro deformation. If the relative deformation is zero, then $\varphi_{ij} \rightarrow \varepsilon_{ij}$ and $\eta_{ijk} \rightarrow \varepsilon_{ij,k}$ which is the second gradient formulation of Form II of Mindlin theory.

Shu et al. (1999) developed finite elements of Fleck—Hutchinson phenomenological strain gradient theory which fits within the Toupin—Mindlin framework. The developed elements are of the mixed type that use displacements and displacement gradients as nodal degrees of freedom. These elements require C^0 continuity in displacement based FE implementation rather than the usual C^1 continuity of the usual gradient elasticity. Although, they simplified the formulation by C^0 continuous finite elements, stability issues are present for the developed finite elements.

In order to illustrate the size effect in materials, Aifantis (1999) considered the gradient elasticity by adopting a simple strength of materials approach for torsion and bending of solid bars. He considered the first and second gradient of the strain in torsion and bending formulations. He showed that the first or the second gradient of the strain components is dominant according to the loading condition and material.

Askes and Gutiérrez (2006) discussed mixed finite element method and the order of shape functions for unkowns for gradient elasticity.

Davoudi et al. (2009) considered the stress field of a screw dislocation inside an embedded nanowire within the theory of strain-gradient elasticity. They showed that the stress singularity is removed around the dislocation and all stress components are continuous and smooth across the interface, in contrast to the singular stress field of the classical theory of elasticity.

There are several studies concerning strain gradient formulations of rods/bars/beams and shells/plates. Beskou and Beskos (2010) provided a review on the gradient elastic response of bars, beams, plates and shells under static loading with the Aifantis model.

Aifantis (2011) provided a review article comparing different theories including the Eringen's nonlocal stress gradient model, the Aifantis strain gradient model, the Mindlin higher order model. He also gave several example applications of strain gradient elasticity.

In addition to statics formulations, there have also been dynamic formulations of the Aifantis gradient elasticity including Laplacian of acceleration in literature. In their review article, Askes and Aifantis (2011) provided static and dynamic formulations and applications of gradient elasticity.

Although static applications are concerned in this study, the gradient elasticity is also utilized in dynamics. In dynamics, wave dispersion is studied generally with the gradient elasticity, see Askes and Aifantis (2011), Askes and Gitman (2010).

Akgöz and Civalek (2016) investigated static bending response of SWCNTs embedded in an elastic medium on the basis of higher-order shear deformation microbeam models in conjunction with modified strain gradient theory.

Barretta et al. (2017) studied the internal length scale parameter ℓ by comparing molecular structural mechanics and gradient elasticity results of CNTs under axial and bending loads. They commented that ℓ depends on CNT diameter, length, boundary conditions, chirality etc. They also stated that nonlocal effects diminish as the geometrical parameters are increased, converging to the same value in all considered cases.

Barretta et al. (2017) studied the bending of armchair carbon nanotubes by means of the gradient elasticity. They determined the internal length scale parameter employed in the Bernoulli-Euler and the Timoshenko gradient formulations with molecular structural mechanics simulations with different loading and kinematic boundary conditions.

Detailed information on the irreducible forms and mechanical interpretations of the strain gradients and higher order stiffness tensors can be found in Aufray (2013), Aufray et al. (2013), Lazar (2016), Gusev and Lurie (2017), Polizzotto (2017).

Several authors provided the variational formulation of gradient elasticity in the large deformation framework, see Rudraraju et al. (2014), Zibaei et al. (2014), Abali et al. (2015). The variational procedure for the large strain Mindlin model is the

same as in the small strain case, which is discussed in previous section. Therefore, some of the discussions are not given for the large strain gradient elasticity.

CHAPTER 4

A MODULUS GRADIENT MODEL FOR AN AXIALLY LOADED INHOMOGENEOUS ELASTIC ROD

In the previous chapter, several non-classical elasticity formulations are introduced. The details are given for the Eringen model of nonlocal elasticity and the Aifantis model of gradient elasticity. It is seen that, these formulations involve higher order strain/stress fields and nonstandard boundary conditions which are difficult to understand intuitively. They also have complex variational and finite element formulations/implementations.

In this chapter, a new simple gradient elasticity formulation, E-grad model (Gülaşık et al. 2018a), is proposed. In the new formulation, similar to the relation between local and gradient fields of displacement/strain/stress in the gradient models of Aifantis (Askes et al. 2008), a differential relation is proposed for the elastic modulus variation of a one-dimensional inhomogeneous rod.

Before giving the details of the proposed model, in Section 4.1, the gradient elasticity of Aifantis is briefly reviewed and its analytical solution is presented. Then, in Section 4.2, the E-grad model is introduced. In Section 4.3, the results of Aifantis's and E-grad models are presented and discussed for a one-dimensional inhomogeneous rod.

4.1.   REVIEW OF AIFANTIS'S GRADIENT ELASTICITY MODEL

In this section, Aifantis's gradient elasticity theory is briefly explained in the displacement form.

4.1.1.   Problem Definition and Governing Differential Equations

Aifantis (1992) proposed a simple gradient elasticity model with only one more additional constant compared to the classical elasticity. In his strain gradient

elasticity formulation, stress at a material point is not only a function of the strain but also function of the higher order derivative of the strain. The simplest form of gradient elasticity is given in indicial notation as:

$$\sigma_{ij} = C_{ijkl}\left(\varepsilon_{kl} - \ell^2 \varepsilon_{kl,mm}\right) \tag{4.1}$$

Eqn. (4.1) represents the strain gradient form of the Aifantis's model. Using the classical strain-displacement relations $\varepsilon_{kl} = 1/2(u_{k,l} + u_{l,k})$ and the symmetry conditions of C_{ijkl}, the displacement gradient form of the Aifantis's model is derived from Eqn. (4.1) as:

$$\sigma_{ij} = C_{ijkl}\left(u_{k,l} - \ell^2 u_{k,lmm}\right) \tag{4.2}$$

Insertion of Eqn. (4.2) into the static equilibrium equation $\sigma_{ij,j} + b_i = 0$ results in:

$$\frac{1}{2}C_{ijkl}\left(u_{k,lj} + u_{l,kj} - \ell^2\left(u_{k,lj} + u_{l,kj}\right)_{,mm}\right) + b_i = 0 \tag{4.3}$$

where, b_i is the body load per unit volume. Neglecting the body forces in a one-dimensional problem, Eqn. (4.3) can be written as:

$$u_{x,xx} - \ell^2 u_{x,xxxx} = 0 \tag{4.4}$$

The analytical solution of this differential equation is given in Askes et al. (2008) as:

$$u(x) = a_1 + a_2 x + a_3 e^{\frac{x}{\ell}} + a_4 e^{-\frac{x}{\ell}} \tag{4.5}$$

As a model problem, a 3-phase rod with different Young's moduli subjected to a tip displacement is considered, Figure 4.1, and solutions are provided further. The displacement field in Eqn. (4.5) can be written for each phase of the rod as:

$$0 < x < L_M \qquad u_1(x) = c_1 + c_2 x + c_3 e^{\frac{x}{\ell}} + c_4 e^{-\frac{x}{\ell}} \tag{4.6}$$

$$L_M < x < L_M + L_I \qquad u_2(x) = c_5 + c_6 x + c_7 e^{\frac{x}{\ell}} + c_8 e^{-\frac{x}{\ell}} \tag{4.7}$$

$$L_M + L_I < x < 2L_M + L_I \qquad u_3(x) = c_9 + c_{10}x + c_{11}e^{\frac{x}{\ell}} + c_{12}e^{-\frac{x}{\ell}} \tag{4.8}$$

The coefficients $c_1 \ldots c_{12}$ in in Eqns. (4.6)-(4.8) are solved for the considered displacement/strain/traction boundary conditions along the rod. Once the coefficients are obtained, displacement, strain and stress fields can be computed.
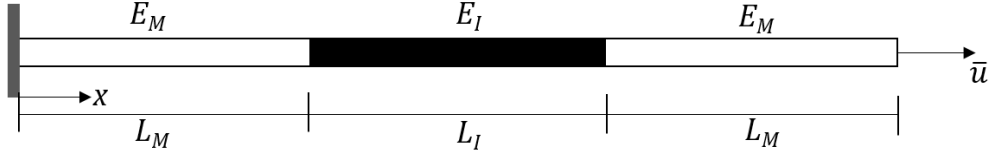
Figure 4.1 *– 3-phase rod subjected to prescribed tip displacement*

4.1.2. Boundary Conditions

The considered boundary conditions are given below. These conditions correspond to continuity of displacement u, displacement gradient $u_{,x}$, traction t and higher order traction q along the interfaces. In addition, at the two ends of the rod the displacement u and its second derivative $u_{,xx}$ are assumed to be prescribed.

$$x = 0, \qquad u_1 = 0 \quad \rightarrow \quad c_1 + c_3 + c_4 = 0 \tag{4.9}$$

$$x = 0, \qquad u_{1,xx} = 0 \rightarrow \quad c_3 + c_4 = 0 \tag{4.10}$$

$$x = L_M, \qquad u_1 = u_2 \quad \rightarrow \quad \begin{aligned} &c_1 + c_2 L_M + c_3 e^{\frac{L_M}{\ell}} + c_4 e^{-\frac{L_M}{\ell}} \\ &= c_5 + c_6 L_M + c_7 e^{\frac{L_M}{\ell}} + c_8 e^{-\frac{L_M}{\ell}} \end{aligned} \tag{4.11}$$

$$x = L_M, \qquad u_{1,x} = u_{2,x} \rightarrow \quad \begin{aligned} &c_2 + \frac{1}{\ell} c_3 e^{\frac{L_M}{\ell}} - \frac{1}{\ell} c_4 e^{-\frac{L_M}{\ell}} \\ &= c_6 + \frac{1}{\ell} c_7 e^{\frac{L_M}{\ell}} - \frac{1}{\ell} c_8 e^{-\frac{L_M}{\ell}} \end{aligned} \tag{4.12}$$

$$x = L_M, \qquad t_1 = t_2 \quad \rightarrow \quad E_M c_2 = E_I c_6 \tag{4.13}$$

$$x = L_M, \qquad q_1 = q_2 \quad \rightarrow \quad \begin{aligned} &E_M \left[c_3 e^{\frac{L_M}{\ell}} + c_4 e^{-\frac{L_M}{\ell}} \right] \\ &= E_I \left[c_7 e^{\frac{L_M}{\ell}} + c_8 e^{-\frac{L_M}{\ell}} \right] \end{aligned} \tag{4.14}$$

$$x = L_M + L_I, \qquad u_2 = u_3 \quad \rightarrow \quad \begin{aligned} &c_5 + c_6(L_M + L_I) + c_7 e^{\frac{L_M+L_I}{\ell}} \\ &\qquad\qquad + c_8 e^{-\frac{L_M+L_I}{\ell}} \\ &= c_9 + c_{10}(L_M + L_I) + c_{11} e^{\frac{L_M+L_I}{\ell}} \\ &\qquad\qquad + c_{12} e^{-\frac{L_M+L_I}{\ell}} \end{aligned} \tag{4.15}$$

$$x = L_M + L_I, \quad u_{2,x} = u_{3,x} \rightarrow \quad \begin{aligned} & c_6 + \frac{1}{\ell}c_7 e^{\frac{L_M+L_I}{\ell}} - \frac{1}{\ell}c_8 e^{-\frac{L_M+L_I}{\ell}} \\ & = c_{10} + \frac{1}{\ell}c_{11}e^{\frac{L_M+L_I}{\ell}} - \frac{1}{\ell}c_{12}e^{-\frac{L_M+L_I}{\ell}} \end{aligned} \tag{4.16}$$

$$x = L_M + L_I, \quad t_2 = t_3 \quad \rightarrow \quad E_I c_6 = E_M c_{10} \tag{4.17}$$

$$x = L_M + L_I, \quad q_2 = q_3 \quad \rightarrow \quad \begin{aligned} & E_I\left[c_7 e^{\frac{L_M+L_I}{\ell}} + c_8 e^{-\frac{L_M+L_I}{\ell}}\right] \\ & = E_M\left[c_{11}e^{\frac{L_M+L_I}{\ell}} + c_{12}e^{-\frac{L_M+L_I}{\ell}}\right] \end{aligned} \tag{4.18}$$

$$x = 2L_M + L_I, \quad u_3 = \bar{u} \quad \rightarrow \quad \begin{aligned} & c_9 + c_{10}(2L_M + L_I) + c_{11}e^{\frac{2L_M+L_I}{\ell}} \\ & + c_{12}e^{-\frac{2L_M+L_I}{\ell}} = \bar{u} \end{aligned} \tag{4.19}$$

$$x = 2L_M + L_I, \quad u_{3,xx} = 0 \quad \rightarrow \quad c_{11}e^{\frac{2L_M+L_I}{\ell}} + c_{12}e^{-\frac{2L_M+L_I}{\ell}} = 0 \tag{4.20}$$

Because the model of Aifantis is a simplification of the more general Mindlin model, some additional fields and also gradient enhanced versions of classical fields are present. The mentioned fields are summarized together with the standard displacement, strain and stress fields below:

$$u(x) = a_1 + a_2 x + a_3 e^{\frac{x}{\ell}} + a_4 e^{-\frac{x}{\ell}} \tag{4.21}$$

$$\varepsilon(x) = u_{,x} = a_2 + \frac{1}{\ell}a_3 e^{\frac{x}{\ell}} - \frac{1}{\ell}a_4 e^{-\frac{x}{\ell}} \tag{4.22}$$

$$\eta(x) = \varepsilon_{,x} = u_{,xx} = \frac{1}{\ell^2}a_3 e^{\frac{x}{\ell}} + \frac{1}{\ell^2}a_4 e^{-\frac{x}{\ell}} \tag{4.23}$$

$$e(x) = \varepsilon - \ell^2 \varepsilon_{,xx} \tag{4.24}$$

$$\sigma(x) = E\varepsilon \tag{4.25}$$

$$\mu(x) = \ell^2 E\eta = \ell^2 E\varepsilon_{,x} \tag{4.26}$$

$$\sigma^g(x) = E(\varepsilon - \ell^2 \varepsilon_{,xx}) = Ee \tag{4.27}$$

$$t(x) = E(u_{,x} - \ell^2 u_{,xxx}) = E(\varepsilon - \ell^2 \varepsilon_{,xx}) = \sigma^g \tag{4.28}$$

$$q(x) = \ell^2 E u_{,xx} = \mu \tag{4.29}$$

where, η is the strain gradient field, e is the effective (gradient) strain feld, σ is the

stress field, μ is the higher order stress field, σ^g is the effective (gradient) stress field, t is the traction (gradient enhanced), q is the higher order traction. The details of the variational formulation, boundary conditions, higher order and enhanced fields of the gradient elasticity formulation can be found in Polizzotto (2003), Gao and Park (2007) and Askes et al. (2008).

4.2. E-MODULUS GRADIENT (E-GRAD) MODEL

In gradient elasticity theories, there are additional and enhanced vector and tensor fields which are difficult to interpret. The boundary conditions also require special attention which also need to be changed according to the type of formulation, i.e., displacement gradient, strain gradient, or stress gradient elasticity formulations (Askes et al., 2008).

In this section, as in the Aifantis's gradient formulations, a gradient formulation is applied to the elasticity modulus of an inhomogeneous rod (Gülaşık et al. 2018a):

$$E^g - \ell^2 E^g_{,xx} = E^c \qquad (4.30)$$

where, E^g is the gradient enhanced continuous Young's modulus field, E^c is classical discontinuous Young's modulus field of inhomogeneous material and ℓ is the internal length scale parameter. As a result of Eqn. (4.30), a continuous modulus variation of E^g is obtained along the inhomogeneous rod compared to step-wise variation of E^c in classical elasticity theory. E-grad model also leads to a continuous variation in displacement, strain and stress fields along the rod. Furthermore, E-grad model does not need introduction of several additional enhanced gradient fields and the boundary conditions are easier to interpret in comparison to gradient models available in literature.

It is important to note that, higher-order fields are indeed needed for the correct simulation of some singular elasticity problems. For example, Rudararaju et al. (2014) removed the singularities in a homogeneous elastic material deformed by an edge loading by using higher-order gradient elasticity theory.

4.2.1. Problem Definition and Governing Differential Equations

The solution of Eqn. (4.30) is given as:

$$E^g(x) = E^c + a_1 e^{\frac{x}{\ell}} + a_2 e^{-\frac{x}{\ell}} \tag{4.31}$$

where, a_1 and a_2 are the constants to be determined with the use of the boundary conditions for modulus change along the rod. Note that for a homogeneous rod, $a_1 = a_2 = 0$ and $E^g = E^c$.

In addition to differential Eqn. (4.30), the constitutive and balance equations are given, respectively, as:

$$\sigma^g(x) = E^g(x)\varepsilon(x) \tag{4.32}$$

$$\sigma^g_{,x} + b = 0 \tag{4.33}$$

where, b is the body force. In Eqn. (4.32) the constitutive relation is written using the gradient enhanced Young's modulus E^g which depends on spatial position x along the rod. Neglecting the body forces, Eqn. (4.33) can be extended as:

$$E^g_{,x}(x)\varepsilon(x) + E^g(x)\varepsilon_{,x}(x) = 0 \tag{4.34}$$

$$E^g_{,x}(x)u_{,x}(x) + E^g(x)u_{,xx}(x) = 0 \tag{4.35}$$

Using Eqns. (4.31) and (4.35), the displacement field is obtained as:

$$u(x) = \frac{k_1 \ell \, tan^{-1}\left(\dfrac{2c_1 e^{\frac{x}{\ell}} + E^c}{\sqrt{4c_1 c_2 - (E^c)^2}}\right)}{\sqrt{4c_1 c_2 - (E^c)^2}} + k_2 \tag{4.36}$$

where, k_1 and k_2 are the constants to be determined with the use of boundary conditions for the displacement.

The same 3-phase rod in Figure 4.1 is also considered for the E-grad formulation. The Young's modulus equations for each phase of the rod can be written with the help of Eqn. (4.31):

$$0 < x < L_M \qquad E^g_1(x) = E_M + c_1 e^{\frac{x}{\ell}} + c_2 e^{-\frac{x}{\ell}} \tag{4.37}$$

$$L_M < x < L_M + L_I \qquad E^g_2(x) = E_I + c_3 e^{\frac{x}{\ell}} + c_4 e^{-\frac{x}{\ell}} \tag{4.38}$$

$$L_M + L_I < x < 2L_M + L_I \qquad E_3^g(x) = E_M + c_5 e^{\frac{x}{\ell}} + c_6 e^{-\frac{x}{\ell}} \tag{4.39}$$

Then the displacement fields for each phase of the rod are obtained from Eqn. (4.36) as:

$$0 < x < L_M \qquad u_1(x) = \frac{k_1 \ell \, tan^{-1}\left(\dfrac{2c_1 e^{\frac{x}{\ell}} + E_M}{\sqrt{4c_1 c_2 - E_M^2}}\right)}{\sqrt{4c_1 c_2 - E_M^2}} + k_2 \tag{4.40}$$

$$L_M < x < L_M + L_I \qquad u_2(x) = \frac{k_3 \ell \, tan^{-1}\left(\dfrac{2c_3 e^{\frac{x}{\ell}} + E_I}{\sqrt{4c_3 c_4 - E_I^2}}\right)}{\sqrt{4c_3 c_4 - E_I^2}} + k_4 \tag{4.41}$$

$$L_M + L_I < x < 2L_M + L_I \qquad u_3(x) = \frac{k_5 \ell \, tan^{-1}\left(\dfrac{2c_5 e^{\frac{x}{\ell}} + E_M}{\sqrt{4c_5 c_6 - E_M^2}}\right)}{\sqrt{4c_5 c_6 - E_M^2}} + k_6 \tag{4.42}$$

The coefficients $c_1, \dots, c_6$ and $k_1, \dots, k_6$ in Eqn. (4.37)-(4.42) are determined according to given modulus and displacement boundary conditions along the rod. Once the coefficients are obtained, displacement, strain and stress fields can be computed.

4.2.2. Boundary Conditions

The considered E-modulus boundary conditions for the Eqns. (4.37)-(4.39) are as follows. The modulus and the first derivative of the modulus are assumed to be continuous at the interfaces. Furthermore, at the start and the end of the domain E^g is assumed to be equal to the corresponding local modulus:

$$x = 0 \qquad E_1^g = E_M \tag{4.43}$$

$$x = L_M \qquad E_1^g = E_2^g \tag{4.44}$$

$$x = L_M \qquad \left(E_1^g\right)_{,x} = \left(E_2^g\right)_{,x} \tag{4.45}$$

$$x = L_M + L_I \qquad E_2^g = E_3^g \tag{4.46}$$

$$x = L_M + L_I \qquad \left(E_2^g\right)_{,x} = \left(E_3^g\right)_{,x} \tag{4.47}$$

$$x = 2L_M + L_I \qquad E_3^g = E_M \tag{4.48}$$

The boundary conditions for the displacement, u, in Eqns. (4.40)-(4.42), are given next. Displacement continuity and strain continuity are assumed at the interfaces. The displacement is equal to the prescribed displacement at each end.

$$x = 0 \qquad u_1 = 0 \tag{4.49}$$

$$x = L_M \qquad u_1 = u_2 \tag{4.50}$$

$$x = L_M \qquad (u_1)_{,x} = (u_2)_{,x} \tag{4.51}$$

$$x = L_M + L_I \qquad u_2 = u_3 \tag{4.52}$$

$$x = L_M + L_I \qquad (u_2)_{,x} = (u_3)_{,x} \tag{4.53}$$

$$x = 2L_M + L_I \qquad u_3 = \bar{u} \tag{4.54}$$

4.2.3. Finite Element Implementation

The variational formulations of Eqns. (4.30) and (4.33) are needed for the finite element formulation. Therefore, Eqn. (4.30) is multiplied with a weight function and integrated over the domain:

$$\int_L w\left(E^g - \ell^2 E_{,xx}^g\right)dL = \int_L w E^c \, dL \tag{4.55}$$

Integrating by parts the second term of the left integral gives:

$$\int_L \left(w E^g + \ell^2 w' E_{,x}^g\right)dL = \int_L w E^c \, dL + \ell^2 w E_{,x}^g\Big|_0^L \tag{4.56}$$

The last term on the right side of the above equation is the boundary term. By considering E^g to be specified at the boundaries, $x = 0$ and $x = L$, the last term of the above equation vanishes. w and E^g are interpolated as:

$$w = N_E \bar{w} \tag{4.57}$$

$$E^g = N_E \bar{E}^g \tag{4.58}$$

where, N_E is the interpolation function, $\bar{w}$ and $\bar{E}^g$ are nodal values. Inserting Eqns. (4.57) and (4.58) into Eqn. (4.56) gives:

$$\bar{w} \int_L (N_E^T N_E + \ell^2 B_E^T B_E) dL \, \bar{E}^g = \bar{w} \int_L N_E^T E^c dL \qquad (4.59)$$

where, $B_E = \partial N_E / \partial x$. Eqn. (4.59) can be written in matrix form as:

$$K_E \bar{E}^g = F_E \qquad (4.60)$$

where, K_E and F_E are the stiffness matrix and load vector for modulus formulation and are given as:

$$K_E = \int_L (N_E^T N_E + \ell^2 B_E^T B_E) \, dL \qquad (4.61)$$

$$F_E = \int_L N_E^T E^c dL \qquad (4.62)$$

The second equation to discretize is Eqn. (4.35). The FEM formulation of this equation is well-known from one-dimensional elasticity and only the final form is given:

$$K_u \bar{u} = F_u \qquad (4.63)$$

$$K_u = \int_L \bar{E}^g B_u^T B_u \, dL \qquad (4.64)$$

$$F_u = \int_L N_u^T b \, dL \qquad (4.65)$$

where, K_u and F_u are the stiffness matrix and load vector for displacement formulation. As can be seen, Eqns. (4.60) and (4.63) are decoupled. Therefore, after the solution of Eqn. (4.60), Eqn. (4.63) can be solved for the nodal displacements.

4.3. RESULTS

In this section, a comparative study is carried out with Aifantis's gradient elasticity model and E-grad model. Only analytical results are given for Aifantis's model, whereas both analytical and finite element results are given for E-grad model. The considered material parameters are given in Table 4.1. In the table, 'I' stands for the inclusion and 'M' stands for the matrix. Three different ℓ values are considered in the sequel. The Young's modulus values for the matrix and the inclusion correspond to a typical thermoplastic polymer, e.g. PEEK, and carbon nanotubes (CNTs),

respectively.

Table 4.1 – *Problem parameters for 3-phase rod*

L_M [mm]	L_I [mm]	ℓ $[10^{-5}$mm]	E_M [MPa]	E_I [MPa]	$\bar{u}$ [mm]
1x10^{-3}	1x10^{-3}	1, 5, 10	3x10^3	1000x10^3	1 x10^{-5}

4.3.1. Aifantis's Gradient Elasticity Model

Aifantis's model results are given for the 3-phase rod in Figure 4.1 with the parameters in Table 4.1. Using the boundary conditions in Eqns. (4.9)-(4.20), the coefficients in Eqns. (4.6)-(4.8) are found and unknown fields in Eqns. (4.21)-(4.29) are obtained.

Figure 4.2 shows the corresponding displacement field for three different values of ℓ. As expected, displacement variation in the inclusion is much lower than the matrix regions. It can be seen that, with Aifantis's model, a smoother field is obtained along the rod by removing the sharp kinks at the interfaces. By increasing ℓ, the displacement values are increased near the interfaces in the matrix. As $\ell \to 0$, local solution is recovered.
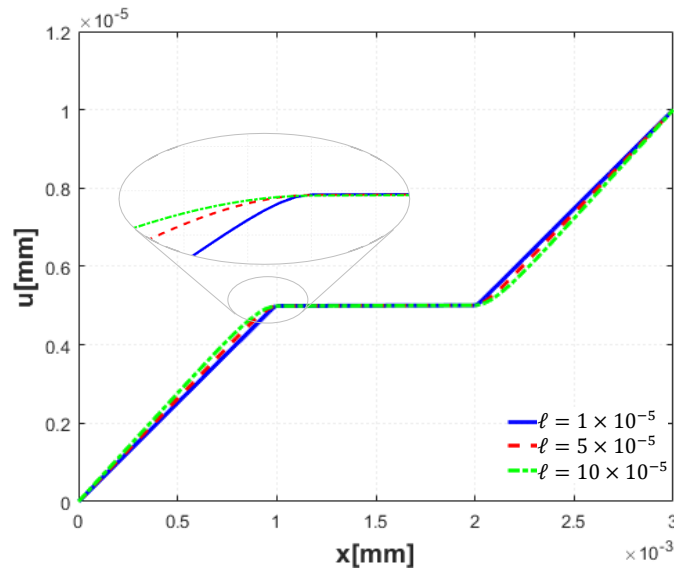
Figure 4.2 – *Analytical displacement, u, results of Aifantis's model for*
$\ell=1\times10^{-5}$, 5×10^{-5}, 10×10^{-5} mm.

Figure 4.3 (a)-(c) show ε, η and e variations along the rod, respectively. Figure 4.3 (a) shows that as ℓ decreases, local solution of ε is recovered. As ℓ increases, the strain discontinuities at the interfaces disappear and ε values increase in CNT and matrix regions. As η is the gradient of the strain, Figure 4.3 (b) shows jumps at the interfaces and these jumps decrease with the increase in ℓ. Figure 4.3 (c) shows a stepwise distribution of e along the rod which is caused because of the stepwise change in modulus values. As in the ε field, e increases in CNT and matrix regions.
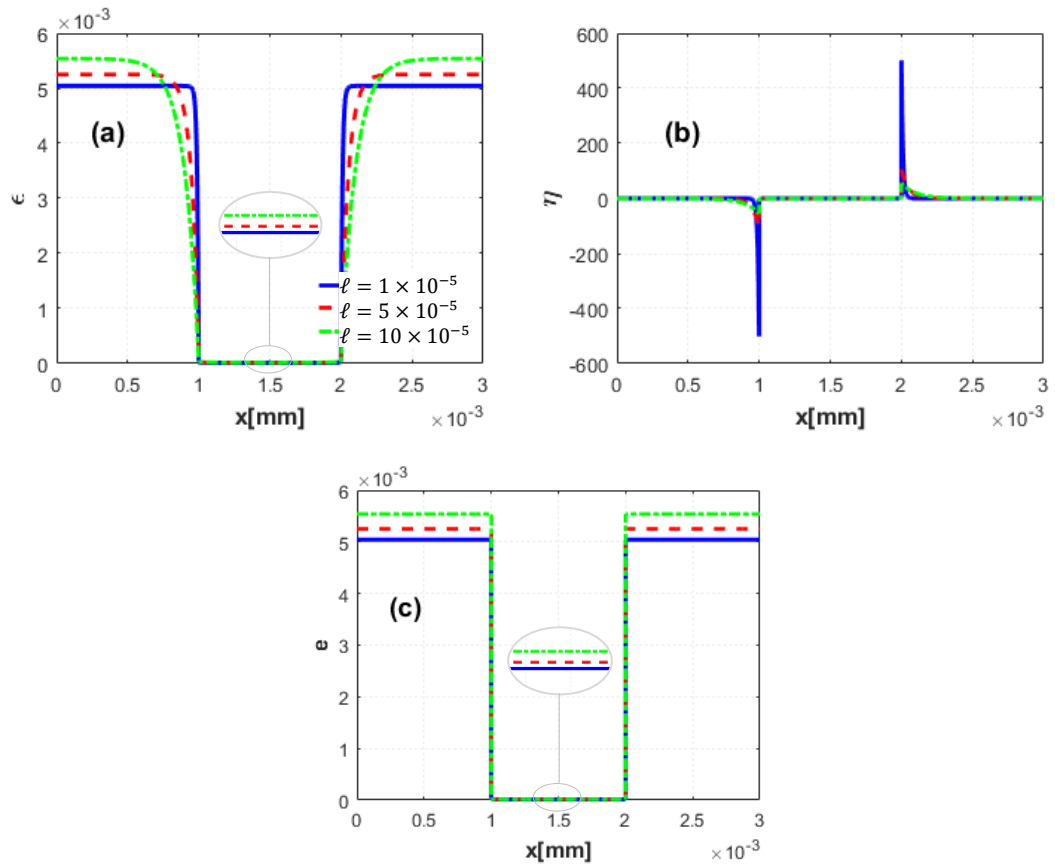
Figure 4.3 *– Analytical results of Aifantis's model for $\ell=1\times10^{-5}$, 5×10^{-5}, 10×10^{-5} mm. (a) Strain ε, (b) strain gradient η and (c) effective strain e.*

Figure 4.4 (a)-(c) show σ, μ and σ^g variations along the rod, respectively. Figure 4.4 (a) shows that σ exhibits jumps at the interfaces and generally increases with l along the rod. On the other hand, μ stays almost constant along the rod except at the interfaces, see Figure 4.4 (b). Figure 4.4 (c) shows that σ^g is constant along the rod

as expected and increases with the increase in ℓ which is sign of the size effect. Tractions t and q are actually σ^g and μ values at the interfaces, therefore t and q fields are the same with σ^g and μ fields in Figure 4.4 (b)-(c).
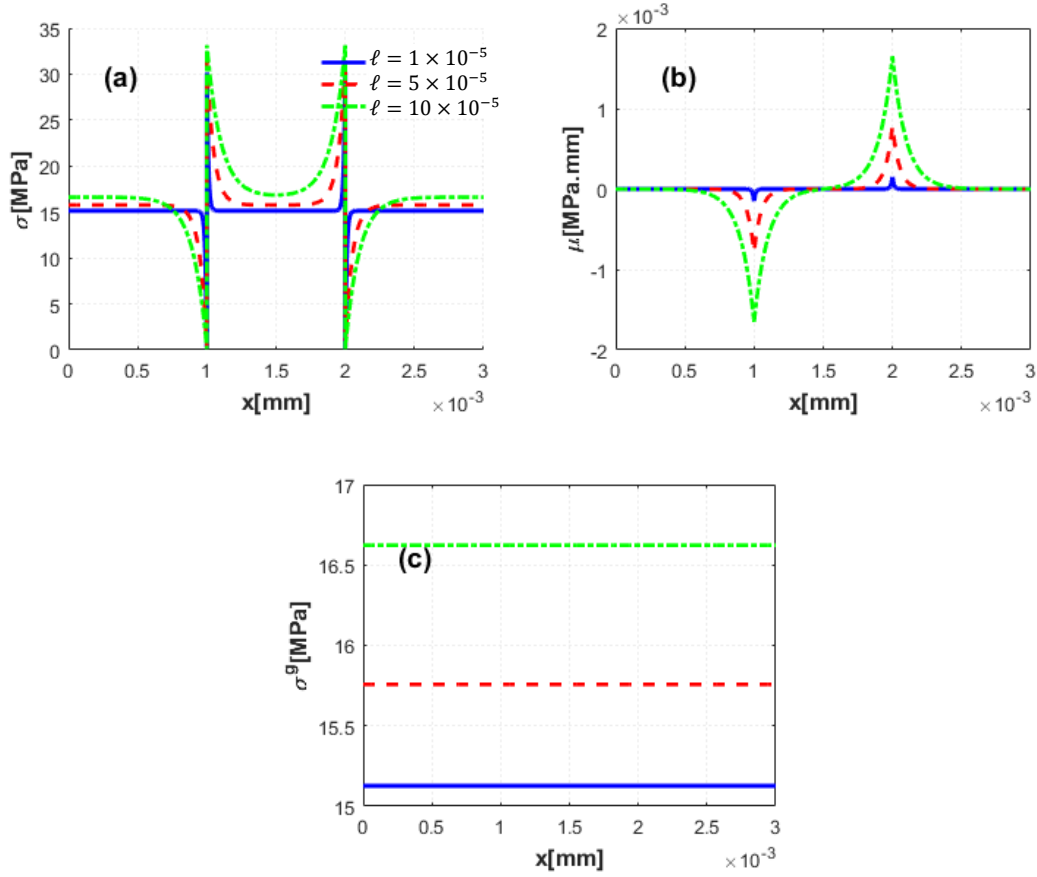
Figure 4.4 –*Analytical results of Aifantis's model for ℓ=1×10⁻⁵, 5×10⁻⁵, 10×10⁻⁵ mm. (a) Stress σ, (b) higher order stress μ, and (c) effective stress σ^g.*

4.3.2. E-grad Model

The coefficients of the analytical solutions of the displacements in Eqns. (4.40)-(4.42) of the E-grad model are obtained from the boundary conditions in Eqns. (4.43)-(4.54). Both analytical and FEM results of E^g, u, ε and σ^g along the rod are given in Figure 4.5 for $l = 10 \times 10^{-5}$ together with the local solution. The solution of gradient enhanced modulus is obtained from Eqn. (4.60) by using 300 linear elements. Then, Eqn. (4.63) is solved for the displacements using the same mesh consisting of 300 linear elements. Naturally, the solution of Eqn. (4.63) requires the

construction of the stiffness matrices. In this construction, the nodal values of the modulus obtained from Eqn. (4.60) are interpolated to two integration points of the linear elements and the stiffness matrices are evaluated with full integration. Having solved the nodal displacements then the strain and stress fields are calculated. As a result of linear shape functions, the strain field is constant inside an element, while the Young's modulus varies linearly due to linear interpolation in Eqn. (4.58). Therefore, the uniform stress state cannot be generated inside a linear element if two integration points are used. This indeed leads to oscillations around the interface between two phases which will be shown in the next section. Therefore, after solving Eqn. (4.60) and Eqn. (4.63), for the visualization purposes the stress is evaluated only at the reduced integration points of the elements. It can be seen that analytical and FEM results are the same and continuity in E^g, u and ε fields are achieved along the rod.
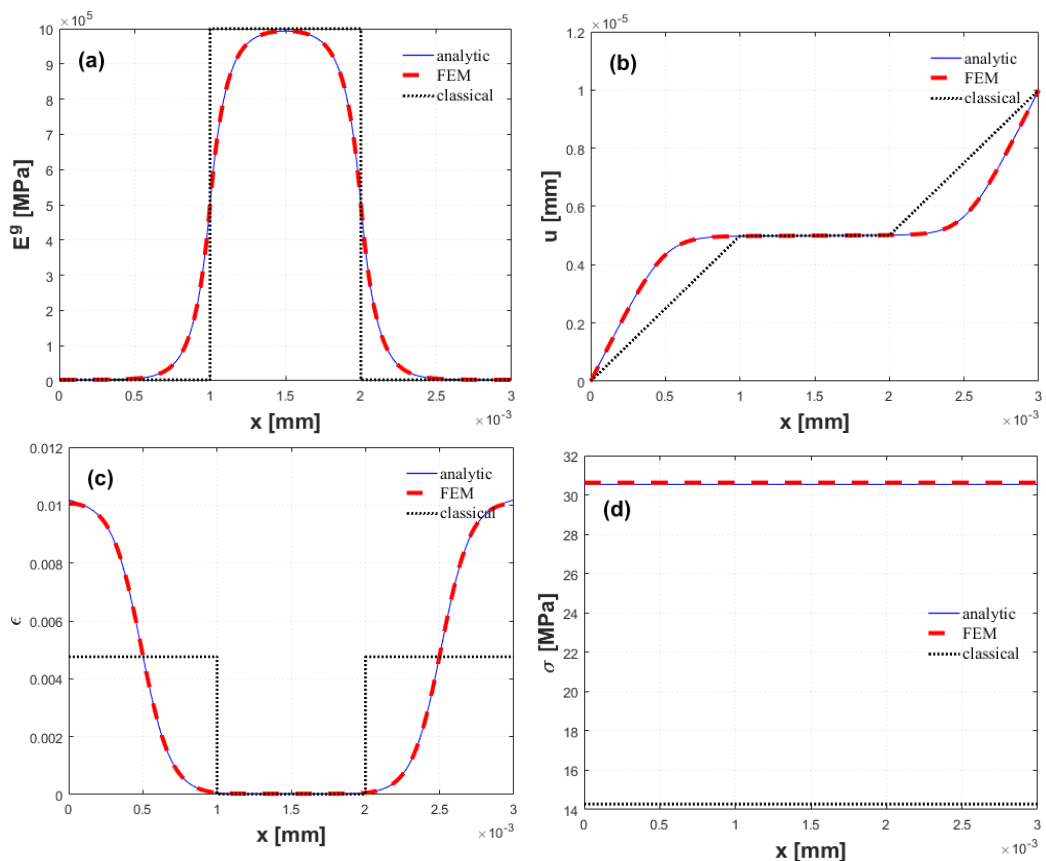
Figure 4.5 – *Analytical and FEM results of E-grad model for ℓ=10×10⁻⁵ mm together with the local solution, (a) Gradient enhanced Young's modulus E^g, (b) displacement u, (c) strain ε, (d) stress σ.*

Figure 4.6 shows FEM results of E-grad model for E^g, u, ε and σ along the rod for different ℓ values. In the figure, the classical elasticity results are also given and it can be seen that as ℓ decreases, all E^g, u, ε and σ fields converge to the classical elasticity solution as expected. Figure 4.6(a) shows that, a smooth transition in E^g values is achieved at the interfaces. The E^g values at both ends and in the middle of the rod remain the same as classical values. Figure 4.6(b) shows that, a continuous displacement field is obtained along the rod by removing the kinks at the interfaces. As expected, the displacement in the inclusion is much lower than the matrix regions. The displacement values in the matrix, particularly near the interfaces, increase by increasing ℓ. As $\ell \rightarrow 0$, the local solution is recovered. Figure 4.6 (c) shows that, with an increase in ℓ, the strain values in the matrix close to the interfaces decease and strain values in the matrix near the boundaries increase. There is also an increase in the strain for the inclusion. Figure 4.6 (d) shows that, as ℓ increases, the stress for the E-grad model increases which is the sign of the size effect.

Figure 4.7 compares the results of the Aifantis's model and the proposed E-grad model for u, ε and σ fields along the rod for $\ell = 10 \times 10^{-5}$. It can be seen that the effects of ℓ on E-grad model results are much stronger than the Aifantis's model. Figure 4.7(a) shows that, the matrix near the interface exhibits much larger displacements for E-grad model than the Aifantis's formulation, although the displacement at the ends are the same. As already shown in Figure 4.3(c), the effective strain, e, in the Aifantis's model shows a stepwise behavior whereas the strain in the E-grad model shows a continuous behavior along the rod. The strains in the matrix for the E-grad model decrease near the interfaces and significantly increase towards to both ends, see Figure 4.7(b). The strain in the E-grad model at the boundaries is 0.010054 whereas it is 0.005541 for the Aifantis's formulation, which means almost a %100 increase. The same behavior in strain is also seen in the uniform stress values in Figure 4.7(c); the stress is 30.62 MPa for the E-grad model whereas it is 16.62 MPa for the Aifantis's model.
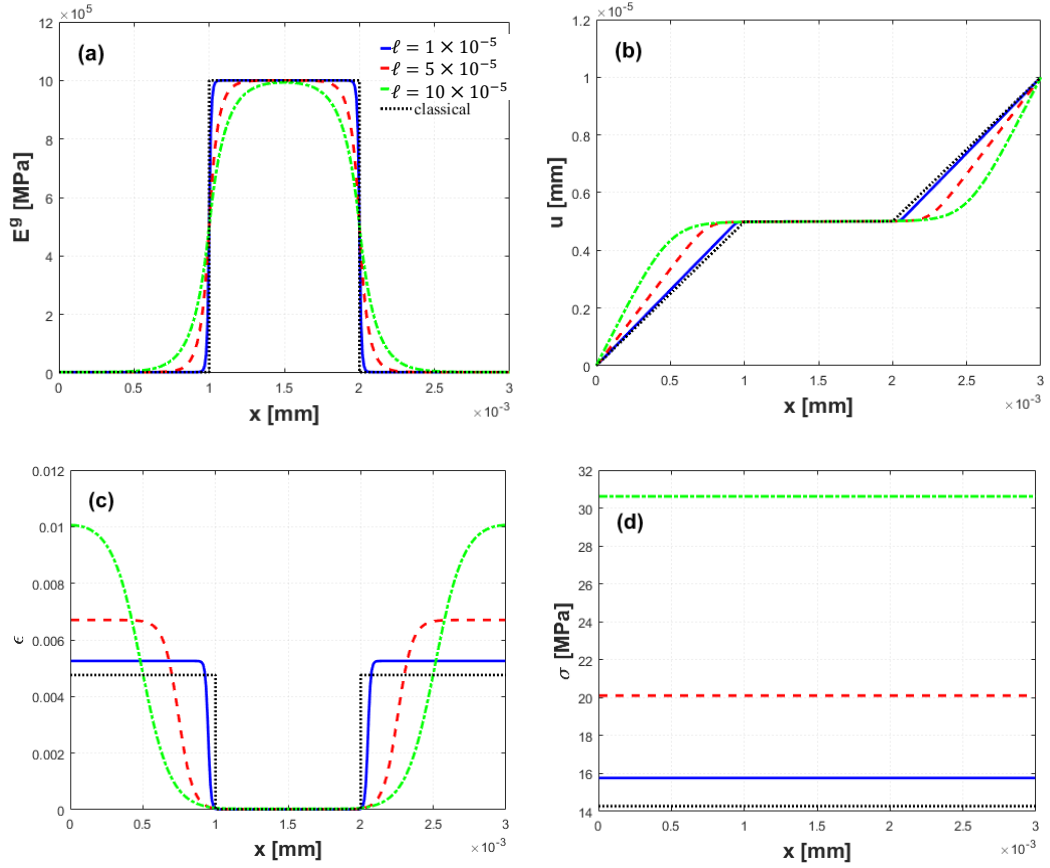
Figure 4.6 – *FEM results for E-grad model for ℓ=0, 1×10⁻⁵, 5×10⁻⁵, 10×10⁻⁵ mm. (a) gradient enhanced Young's modulus E^g, (b) displacement u, (c) strain ε, (d) stress σ.*

4.3.2.1. Oscillation in the Stress Field and Effect of Mesh Refinement

When the fully integrated finite elements are used, oscillations in the stress field are observed as mentioned in the previous section. This is because of the interpolation orders of the modulus-field (E) and the displacement field (u). The displacement is linear and therefore, the strain is constant inside an element, while E is linear inside an element. Thus, the stress evaluated as $\sigma = E\varepsilon$ cannot be uniform inside a linear element if two integration points are used. This indeed leads to oscillations around the interface between two phases.

A study is performed to show how the oscillations change is investigated with element size and interpolation order, see Figure 4.8. In the first case, linear

interpolations are used for the modulus-field (E) and the displacement field (u), and the stress is visualized at full integration points, see Figure 4.8(a). In the second case, quadratic interpolations are used for the modulus-field (E) and the displacement field (u), and the stress is again visualized at full integration points, see Figure 4.8(b). As can be seen from the figures as the number of elements increases the magnitude of the oscillations decreases. Furthermore, the use of quadratic interpolation function reduces the magnitude of oscillations about one order of magnitude. Please note that the minimum and maximum values of the stress axis is 29.6 MPa and 31.6 MPa for Figure 4.8(a), while they are 30.4 MPa and 30.65 MPa for Figure 4.8(b).
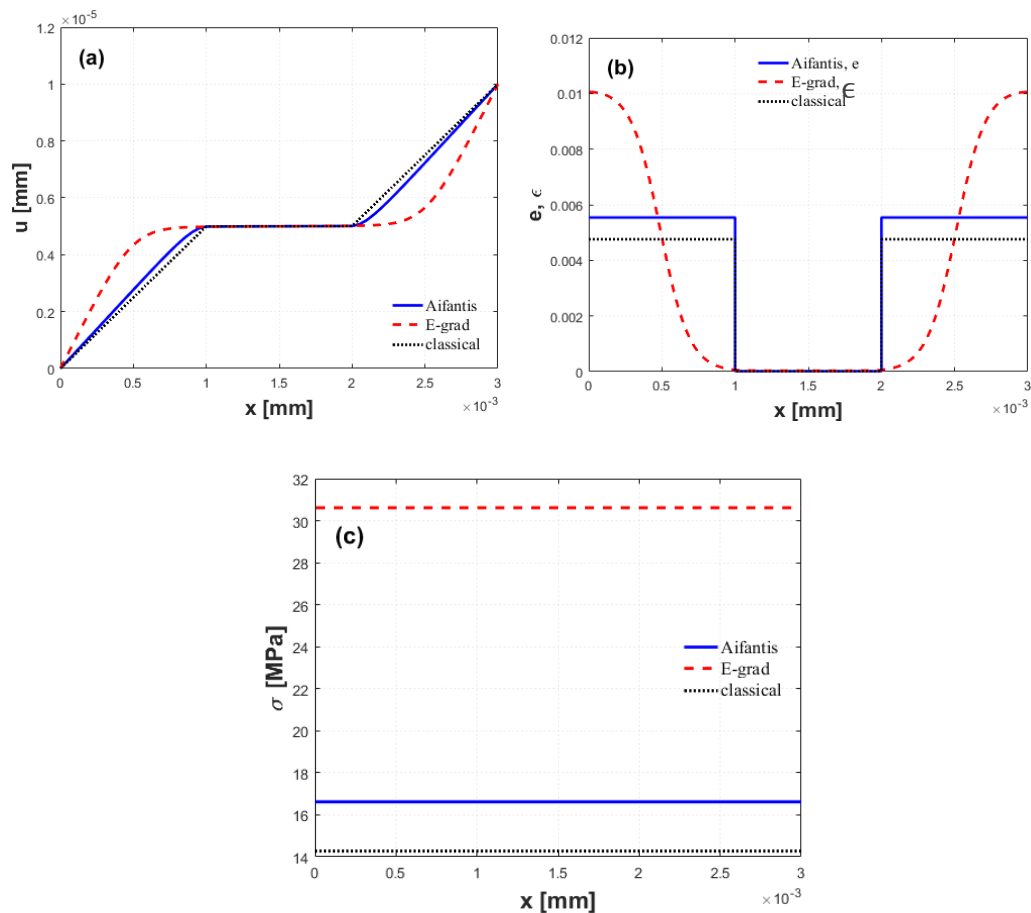
Figure 4.7 – *Comparison of the Aifantis's model and E-grad model results for ℓ= 10×10⁻⁵ mm. (a) displacement u, (b) strain ε, (c) stress σ.*

A case where the modulus-field (E) is interpolated with 300 linear shape functions while the displacement field (u) is interpolated with 150 quadratic shape functions

is also investigated, Figure 4.9. Therefore, the nodes of both meshes coincide. First the nodal E values are determined and then they are interpolated to full integration points of the mesh consisting of 150-quadratic elements for the solution of the displacement field. Finally, the stress is visualized by using full integration points of the quadratic mesh. The solution obtained by this procedure is compared with the one in which both fields are interpolated with quadratic functions (QQ), see Figure 4.9. As can be seen form the figure, E, u and ε fields are almost the same, while there is a small shift in the stress field.
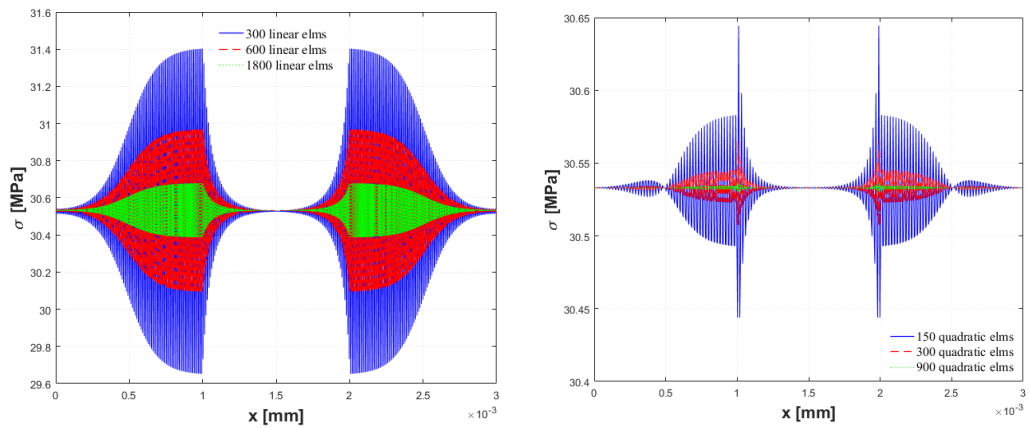
Figure 4.8 – FEM results for E-grad model for ℓ=10×10⁻⁵ mm. (a) σ for 300/600/1800 linear elements, (b) σ for 150/300/900 quadratic elements
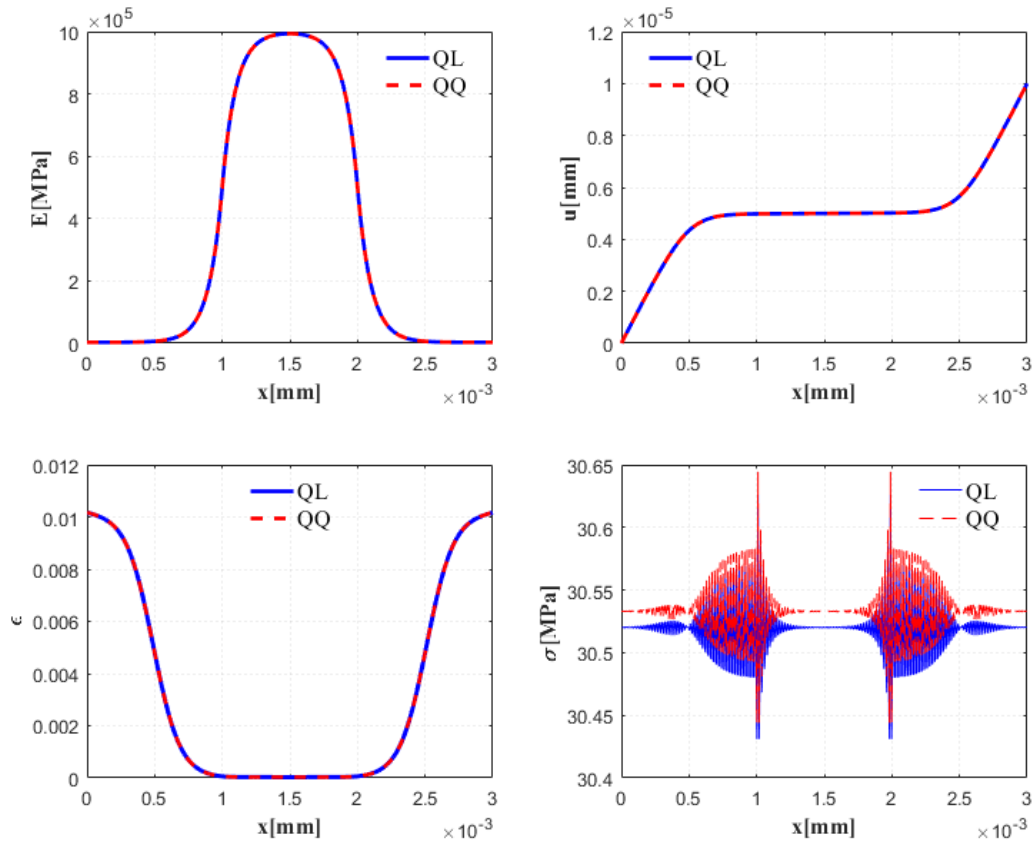
Figure 4.9 *– Comparison of FEM results for E-grad model for a linear interpolation of E, a quadratic interpolation of u and a quadratic interpolation of E, a quadratic interpolation of u. (a) Gradient enhanced Young's modulus E^g, (b) displacement u, (c) strain ε, (d) stress σ. Results are shown for $\ell=10\times10^{-5}$ mm.*

CHAPTER 5

A MODULUS GRADIENT MODEL FOR INHOMOGENEOUS MATERIALS WITH ISOTROPIC LINEAR ELASTIC CONSTITUENTS

In this chapter, E-grad model for a one-dimensional inhomogeneous linear elastic rod proposed in the previous chapter is extended to a more general three-dimensional framework (Gülaşık et al. 2018b). Furthermore, a two-dimensional axisymmetric finite element formulation is given and a model problem is studied in detail.

The governing partial differential equations of the proposed gradient elasticity model and related boundary conditions are discussed in Section 5.1. In Section 5.2, the weak forms of the differential equations and an axisymmetric finite element implementation of the model are provided. In Section 5.3, a soft cylindrical rod with a stiff spherical inclusion is solved and a comparison with experimental results of a polyimide/silica nanocomposite is given.

5.1.   DESCRIPTION OF THE MODEL

Let $\mathcal{M}$ be a set of elastic constants for an isotropic linear elastic material:

$$\mathcal{M} = \{E^g, G^g, \nu^g, \kappa^g, \lambda^g\} \tag{5.1}$$

where E^g is the Young's modulus, G^g is the shear modulus, ν^g is the Poisson's ratio, κ^g is the bulk modulus and λ^g is the Lame's constant. Obviously only two of the five elastic constants given above are independent for an isotropic linear elastic material. Three-dimensional generalization of the differential Eqn. (4.30) can be written for any material parameter $M^g \in \mathcal{M}$ as (Gülaşık et al. 2018b):

$$M^g - \operatorname{div}\left(\boldsymbol{\ell}^2 \nabla M^g\right) = M^c \tag{5.2}$$

In the above relations, the superscript g stands for the gradient enhancement of the considered field and the superscript c stands for the local values of the considered field. In Eqn. (5.2), $\boldsymbol{\ell}^2$ is a second-order positive definite symmetric internal length

scale tensor, which can be expressed in the spectral form as:

$$\boldsymbol{\ell}^2 = \sum_\alpha \ell_\alpha^2 \boldsymbol{n}_\alpha \otimes \boldsymbol{n}_\alpha \qquad (5.3)$$

where ℓ_α^2 are the eigenvalues and $\boldsymbol{n}_\alpha$ are the eigenvectors of $\boldsymbol{\ell}^2$. If an ellipsoidal inclusion is considered in a matrix, then the eigenvectors $\boldsymbol{n}_\alpha$ and the eigenvalues ℓ_α^2 can be related to the principal directions and the corresponding radii of the ellipsoid. Therefore, the above form of $\boldsymbol{\ell}^2$ allows different length scale parameters in different directions which accounts for different microstructure variations in various directions. On the other hand, if a spherical inclusion is considered then the eigenvalues ℓ_α^2 can be considered as identical and hence the internal length scale tensor $\boldsymbol{\ell}^2$ becomes diagonal.

Gitman et al. (2010) proposed a similar internal length scale tensor and obtained anisotropic versions of the Aifantis/Eringen models in stress gradient form. Although, the structure of the formulations shows similarities, the internal length scale tensor is directly applied to the stress tensor in Gitman et al. (2010), while it is applied to the elastic material parameters in the proposed model. A detailed discussion on the anisotropy in strain gradient elasticity models can be found in Polizzotto (2018) in which different forms of internal length and moduli tensors are discussed.

It is well known that there are two independent material constants for an isotropic linear elastic material. Therefore, for an inhomogeneous material consisting of isotropic linear elastic constituents, it is required to specify two differential equations for two of the elastic constants belonging to the set $\mathcal{M}$. In this study, Eqn. (5.2) is written for the Young's modulus E^g and the shear modulus G^g, and the formulation is designated as E/G gradient model.

Other than Eqn. (5.2) for the E/G model, the balance equation is required for the description of a mechanical problem as

$$\operatorname{div} \boldsymbol{\sigma}^g + \boldsymbol{b} = \boldsymbol{0} \qquad (5.4)$$

where $\boldsymbol{b}$ is the body force vector and $\boldsymbol{\sigma}^g$ is the stress tensor obtained by a linear elastic constitutive relation

$$\boldsymbol{\sigma}^g = \mathbb{C}^g : \boldsymbol{\varepsilon}^g \tag{5.5}$$

where $\mathbb{C}^g$ is the fourth order isotropic linear elasticity tensor which can be described in terms of two independent elastic constants E^g and G^g. In Eqn. (5.5) $\boldsymbol{\varepsilon}^g$ is the infinitesimal strain tensor, i.e., the symmetric gradient of the displacement vector. The obtained E^g and G^g fields for the E/G model are used in Eqn. (5.5) to compute the corresponding stress field.

To discuss the boundary conditions for the governing partial differential equations (5.2) and (5.4), an inhomogeneous domain Ω consisting of two phases Ω_i and Ω_m such that $\Omega = \Omega_i \cup \Omega_m$ is considered as shown in Figure 5.1. The inclusion Ω_i is considered to be completely embedded into the matrix Ω_m. For the differential equation (5.2) the boundary $\partial\Omega$ of the domain is divided into two distinct sets such that $\partial\Omega = \partial\Omega_M \cup \partial\Omega_{\nabla M}$ and $\emptyset = \partial\Omega_M \cap \partial\Omega_{\nabla M}$, see Figure 5.1(a). Here $\partial\Omega_M$ denotes the boundary where the material parameters are prescribed, i.e., $M^g = \bar{M}^g$, and $\partial\Omega_{\nabla M}$ denotes the boundary where the fluxes of the material parameters are prescribed, i.e., $(\boldsymbol{\ell}^2 \nabla M^g) \cdot \boldsymbol{n} = \bar{M}_n^g$. Here $\boldsymbol{n}$ is the outward unit normal to the boundary. Similarly, for the differential equation (5.4) the boundary $\partial\Omega$ is divided such that $\partial\Omega = \partial\Omega_u \cup \partial\Omega_t$ and $\emptyset = \partial\Omega_u \cap \partial\Omega_t$ where $\partial\Omega_u$ and $\partial\Omega_t$ correspond to the essential boundary where displacements are prescribed, i.e., $\boldsymbol{u} = \bar{\boldsymbol{u}}$ and the natural boundary where tractions are prescribed, i.e., $\boldsymbol{\sigma}\boldsymbol{n} = \bar{\boldsymbol{t}}$, respectively, see Figure 5.1(b).
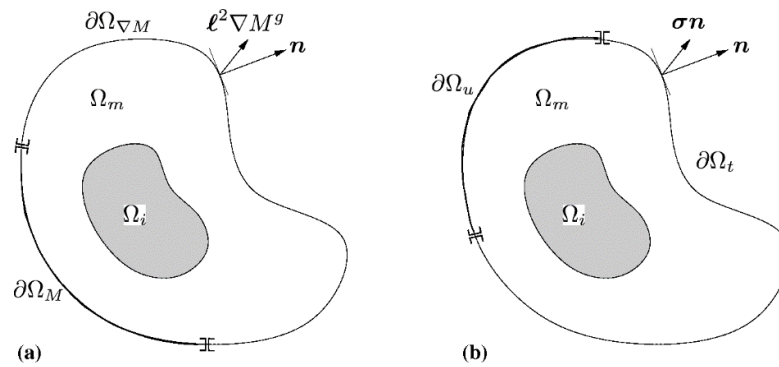
Figure 5.1 – *An inhomogeneous domain Ω consisting of a matrix phase Ω_m and an inclusion phase Ω_i. (a) Decomposition of the boundary $\partial\Omega = \partial\Omega_M \cup \partial\Omega_{\nabla M}$ into two distinct sets for the differential equation (5.2), (b) decomposition of the boundary $\partial\Omega = \partial\Omega_u \cup \partial\Omega_t$ into two distinct sets for the differential equation (5.4).*

5.2.   FINITE ELEMENT IMPLEMENTATION

A two-dimensional axisymmetric finite element implementation of Eqn. (5.2), M^g field, and Eqn. (5.4) is discussed below. However, the derivation from the strong form to the weak form is given for general three-dimensional problems. In order to obtain the weak form, Eqn. (5.2) is multiplied by a scalar test function w and integrated over the domain:

$$\int_\Omega w[M^g - \mathrm{div}\,(\boldsymbol{\ell}^2 \nabla M^g)]dV = \int_\Omega wM^c dV \qquad (5.6)$$

After application of the integration by parts to the second term of left hand side, one obtains:

$$\int_\Omega [wM^g + \nabla w \cdot (\boldsymbol{\ell}^2 \nabla M^g)]dV = \int_\Omega wM^c dV + \int_{\partial\Omega} w(\boldsymbol{\ell}^2 \nabla M^g) \cdot \boldsymbol{n}\, dS \qquad (5.7)$$

where $\boldsymbol{n}$ is the outward unit normal. If an axisymmetric problem is considered and the inclusion is spherical then $\boldsymbol{\ell}^2$ becomes two-dimensional and diagonal, i.e.:

$$\boldsymbol{\ell}^2 = \begin{bmatrix} \ell_r & 0 \\ 0 & \ell_z \end{bmatrix} \qquad (5.8)$$

then Eqn. (5.7) can be written as[1]:

$$\int_\Omega \left(wM^g + w_{,r}\ell_r^2 M_{,r}^g + w_{,z}\ell_z^2 M_{,z}^g\right)2\pi r dA$$

$$= \int_\Omega wM^c 2\pi r dA + \int_{\partial\Omega} w\ell_r^2 M_{,r}^g n_r 2\pi r dS + \int_{\partial\Omega} w\ell_z^2 M_{,z}^g n_z 2\pi r dS \qquad (5.9)$$

where $dA = drdz$, r and z are the radial and axial coordinates, and ℓ_r and ℓ_z denote the length scale parameters in r and z directions. In Eqn. (5.9) n_r and n_z are r and z components of the outward unit normal $\boldsymbol{n}$. In following discussions, the boundary conditions are assumed to be one of the two following cases. Either M^g is specified as equal to M^c at the boundary $\partial\Omega_M$, and therefore $w = 0$, or homogeneous Neumann boundary conditions are assumed, and therefore $M_{,r}^g = M_{,z}^g = 0$ at the

---

[1]*If $\boldsymbol{\ell}^2$ is assumed as a diagonal tensor then the governing differential equation (5.2) for axisymmetric problems becomes $M^g - \frac{1}{r}\frac{\partial}{\partial r}\left(r\ell_r^2 \frac{\partial M^g}{\partial r}\right) - \frac{\partial}{\partial z}\left(\ell_r^2 \frac{\partial M^g}{\partial z}\right) = M^c$.*

boundary $\partial\Omega_{\nabla M}$. Thus, the last two boundary terms in Eqn. (5.9) vanish in the finite element formulation. The test function w and the primary field M^g are interpolated as:

$$w = N\bar{w} \tag{5.10}$$

$$M^g = N\bar{M}^g \tag{5.11}$$

where, $\bar{w}$ and $\bar{M}^g$ are the nodal values of the corresponding fields. Insertion of interpolations Eqn. (5.10) and Eqn. (5.11) into Eqn. (5.9), gives:

$$\bar{w}^T \int_\Omega (N^T N + \ell_r^2 B_r^T B_r + \ell_z^2 B_z^T B_z) 2\pi r dA \, \bar{M}^g = \bar{w}^T \int_\Omega N^T M^c 2\pi r dA \tag{5.12}$$

In Eqn. (5.12), $B_r = \partial N/\partial r, B_z = \partial N/\partial z$ and superscript T represents the transpose of the matrix. For arbitrary nodal variations $\bar{w}$ satisfying homogeneous essential boundary conditions, Eqn. (5.12) can be written in the following form:

$$K_M \bar{M}^g = F_M \tag{5.13}$$

where:

$$K_M = \int_\Omega (N^T N + \ell_r^2 B_r^T B_r + \ell_z^2 B_z^T B_z) 2\pi r dA \tag{5.14}$$

$$F_M = \int_\Omega N^T M^c 2\pi r dA \tag{5.15}$$

Here,K_M denotes the coefficient matrix and F_M denotes the right-hand side vector. M^g in Eqn. (5.11) is:

$$M^g(r,z) = N_1(r,z)\bar{M}_1^g + N_2(r,z)\bar{M}_2^g + N_3(r,z)\bar{M}_3^g + N_4(r,z)\bar{M}_4^g \tag{5.16}$$

for 4-node axisymmetric quadrilateral elements. Clearly, Eqn. (5.16) can also be written as:

$$M^g(r,z) = [N_1(r,z) \ \ N_2(r,z) \ \ N_3(r,z) \ \ N_4(r,z)] \begin{Bmatrix} \bar{M}_1^g \\ \bar{M}_2^g \\ \bar{M}_3^g \\ \bar{M}_4^g \end{Bmatrix} \tag{5.17}$$

The matrices N, B_r and B_z in Eqn. (5.12) are then given as:

$$N = [N_1(r,z) \quad N_2(r,z) \quad N_3(r,z) \quad N_4(r,z)] \tag{5.18}$$

$$B_r = \begin{bmatrix} \dfrac{\partial N_1}{\partial r} & \dfrac{\partial N_2}{\partial r} & \dfrac{\partial N_3}{\partial r} & \dfrac{\partial N_4}{\partial r} \end{bmatrix} \tag{5.19}$$

$$B_z = \begin{bmatrix} \dfrac{\partial N_1}{\partial z} & \dfrac{\partial N_2}{\partial z} & \dfrac{\partial N_3}{\partial z} & \dfrac{\partial N_4}{\partial z} \end{bmatrix} \tag{5.20}$$

The second equation to discretize is the balance equation. The finite element formulation of this equation is well-known. Therefore, only final equations are given without the details of the intermediate steps. The final form of the weak form is given as:

$$\bar{w}^T \int_\Omega (B_u^T \mathbb{C} B_u) 2\pi r dA\, \bar{u} = \bar{w}^T \int_\Omega N^T b 2\pi r dA + \bar{w}^T \int_{\partial\Omega} N^T \bar{t} 2\pi r dS \tag{5.21}$$

where B_u is the strain-displacement matrix, $\mathbb{C}$ is the elasticity matrix, b is the body load and $\bar{t}$ is the boundary traction. For arbitrary nodal variations $\bar{w}$ satisfying homogeneous essential boundary conditions, the above given weak form simplifies to:

$$K_u \bar{u} = F_u \tag{5.22}$$

where $\bar{u}$ is the nodal displacement vector, K_u denotes the stiffness matrix, and F_u stands for the load vector. The explicit integrals defining K_u and F_u are written as:

$$K_u = \int_\Omega (B_u^T \mathbb{C} B_u) 2\pi r dA \tag{5.23}$$

$$F_u = \int_\Omega N^T b 2\pi r dA + \int_{\partial\Omega_t} N^T \bar{t}\, 2\pi r dS \tag{5.24}$$

The first part of the above equation, F_u, is the load vector due to body forces and the second part is due to boundary tractions.

5.3. RESULTS

A cylindrical composite specimen with a spherical inclusion at the center is considered as a model problem as shown in Figure 5.2. The matrix (M) is considered as soft and the spherical inclusion (I) is considered as stiff with the material parameters in Table 5.1. Generic material properties are specified for the matrix

$E_M = 1000$ MPa, $G_M = 384.62$ MPa and the inclusion $E_I = 10000$ MPa, $G_I = 4000$ MPa. These parameter sets correspond to the Poisson's ratios of $\nu_M = 0.3$ and $\nu_I = 0.25$ for the matrix and the inculsion, respectively. The results are provided for $\ell_r = \ell_z = \ell = 0, 0.1 \times 10^{-6}, 0.3 \times 10^{-6}$ mm. Because of the symmetry of the geometry, the problem is modeled as an axisymmetric quarter model as seen in Figure 5.3. The mesh of the model is created by the preprocessor of Abaqus®. The mesh consists of 19061 4-node axisymmetric quadrilateral elements. The mesh size around the interface is chosen to be lower than 0.1×10^{-6} mm to guarantee that the discretization can resolve the length-scale ℓ. Four different paths are defined ($z = 0, z = L, r = 0, r = R$) on the mesh for the visualization of relevant fields.

Table 5.1 – *Problem parameters for the rod with a spherical inclusion*

E_M [MPa]	G_M [MPa]	E_I [MPa]	G_I [MPa]	$\ell = \ell_x = \ell_y$ [mm] $\times 10^{-6}$	$\bar{u}_z$ [mm] $\times 10^{-6}$
1000	384.62	10000	4000	0, 0.1, 0.3	1.25

As mentioned previously, the E/G model, which includes the gradient formulations of the Young's modulus and the shear modulus, is considered for the numerical example. The E/ν model, which includes the gradient formulations of the Young's modulus and the Poisson's ratio, has also been investigated. Since the results of the two formulations are turned out to be the same, only the results of the E/G model are presented.

Two different sets of boundary conditions have to be specified for the problem; one for the gradient-enhanced material parameters E^g, G^g and one for the displacement and/or traction $\boldsymbol{u}$ and/or $\boldsymbol{t}$, see Figure 5.3. The boundary conditions for the material parameters read:

$$E^g(r = R, z) = E_M, \quad G^g(r = R, z) = G_M,$$
$$E^g(r, z = L) = E_M, \quad G^g(r, z = L) = G_M, \qquad (5.25)$$
$$E^g(r = 0, z = 0) = E_I, \quad G^g(r = 0, z = 0) = G_I$$

while the mechanical boundary conditions are:

$$u_z(r, z = 0) = 0, \quad u_r(r = 0, z) = 0,$$

$$u_z(r, z = L) = \bar{u}_z = 1.25 \times 10^{-6} \text{ mm}, \quad t(r = R, z) = 0$$

(5.26)
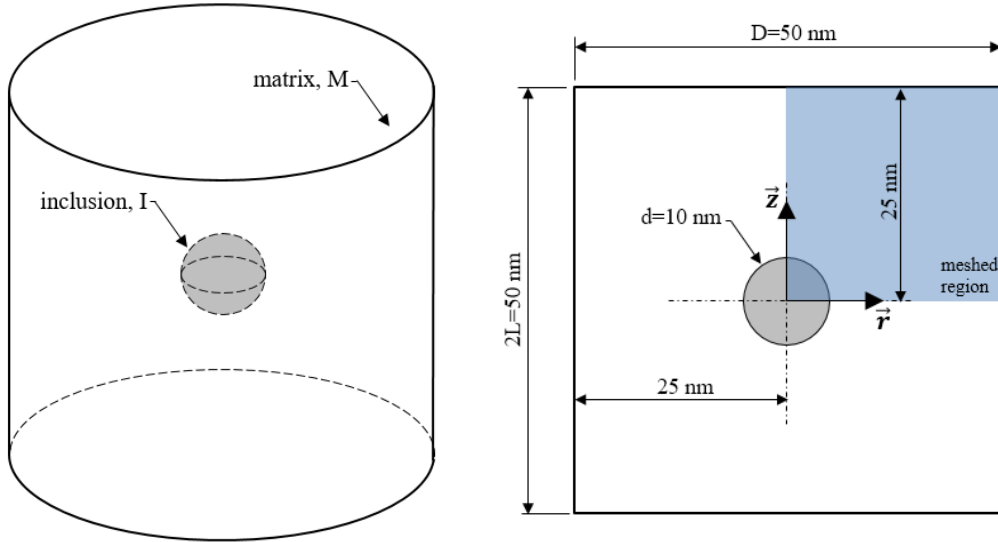
Figure 5.2 *– (a) Cylindrical rod with a spherical inclusion, (b) a central section in the plane of the rod. The axisymmetric quarter model is highlighted in blue.*

Figure 5.4 shows E^g and G^g variations over the quarter domain for the gradient formulation for $\ell = 0.3 \times 10^{-6}$ mm. It can be seen that both E^g and G^g values start with the inclusion properties and gradually decrease to matrix properties without discontinuity at the interface.
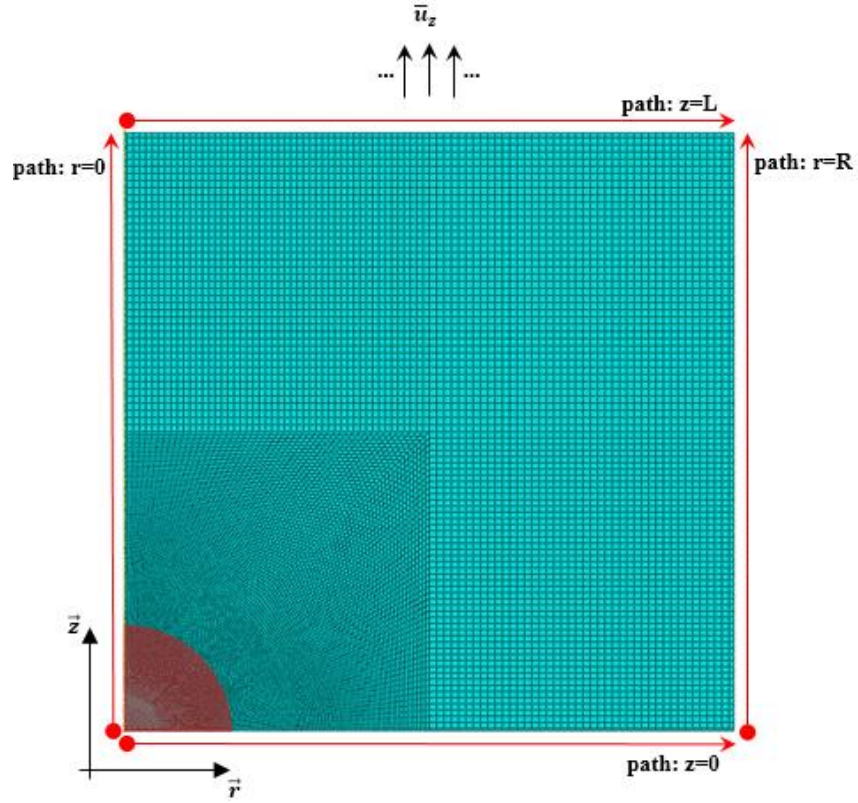
Figure 5.3 – Axisymmetric finite element mesh of the problem generated by Abaqus®
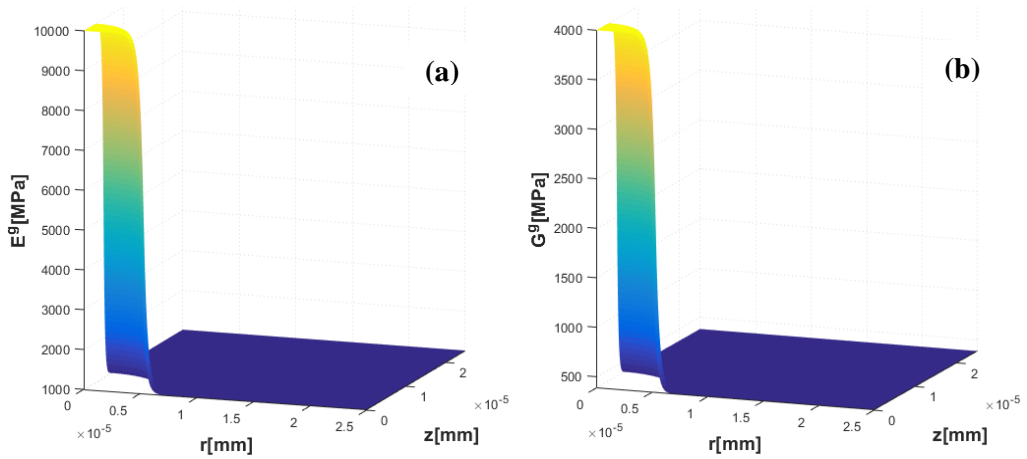
Figure 5.4 – Variations of (a) E^g and (b) G^g fields for the E/G model for $\ell=0.3\times10^{-6}$ mm.

5.3.1. Effect of Length Scale Parameter

In this section, variations of E^g, G^g, u, ε and σ fields are shown along the predefined paths $z = 0, z = L, r = 0$ and $r = R$ (Figure 5.3). Three different ℓ values, i.e., $\ell = 0, 0.1 \times 10^{-6}$ and 0.3×10^{-6} mm, are considered. Note that $\ell=0$ corresponds to the local solution. In Figure 5.5 to Figure 5.13, r represents the radial direction and z represents the longitudinal direction.

Figure 5.5 shows E^g and G^g variations along the path $z = 0$. It can be seen that discontinuous step-like variation of elastic constants in the case of the local model changes to a continuous and diffuse variation for the E-grad model.
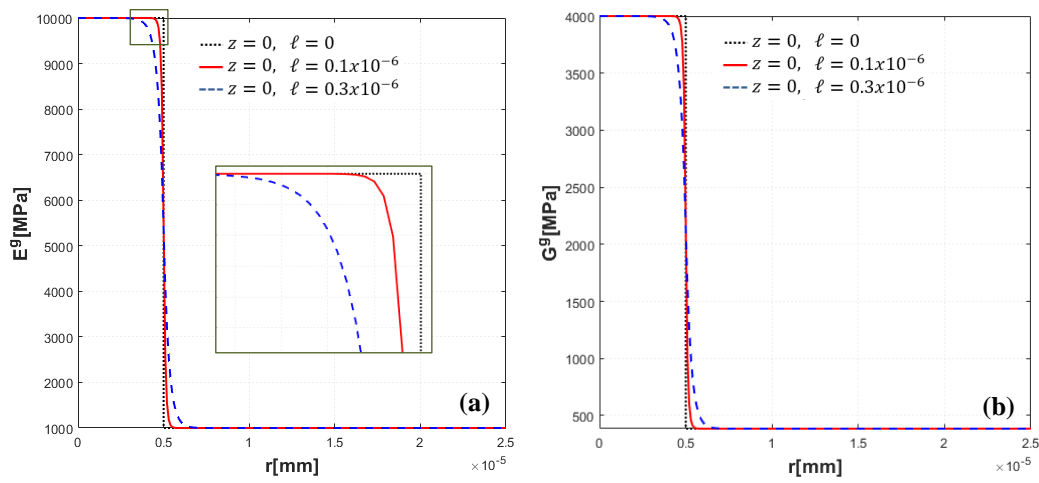
Figure 5.5 – Variations of (a) E^g and (b) G^g along the path $z = 0$ for $\ell=0$, 0.1×10^{-6}, 0.3×10^{-6} mm.

Figure 5.6 (a) depicts u_r^g (radial displacement) along the path $z = 0$. Although the displacement magnitudes are almost the same throughout the domain, they are lower for the gradient model representing a stiffer behavior. Figure 5.6 (b) demonstrates that u_r^g along the path $z = L$ are almost the same for different ℓ values because the path $z = L$ is far away from the inclusion. Since the path $z = L$ is far away from the inclusion the strain ε_z^g corresponding to this path is almost constant as can be seen in Figure 5.6 (b). Figure 5.7(a) shows u_z^g (longitudinal displacement) along the path $r = 0$. Displacement magnitudes are also smaller for the gradient model similar to u_r^g along the path $z = 0$. Variations of u_z^g along the path $r = R$ are almost the same

for different ℓ values representing a homogeneous deformation state, see Figure 5.7 (b).
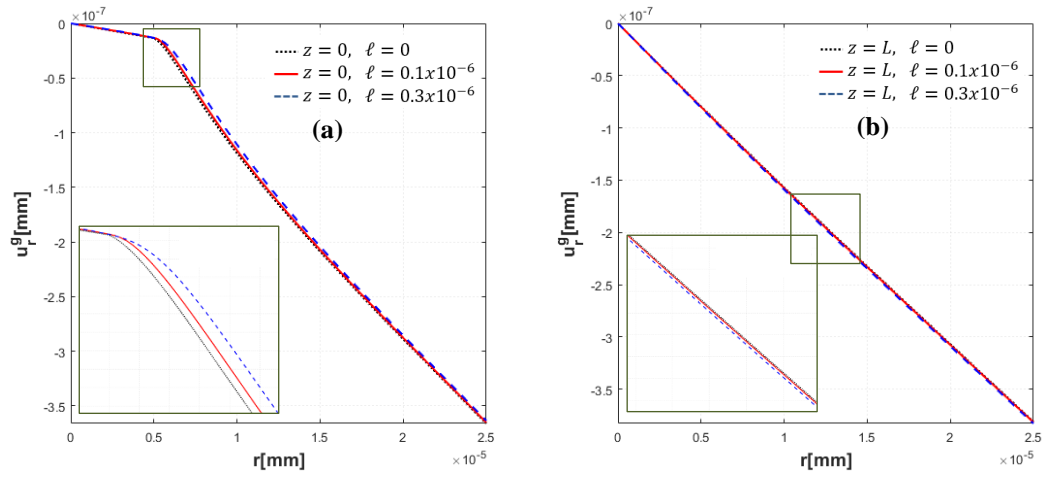
Figure 5.6 *– (a) u_r^g along the path $z = 0$, (b) u_r^g along the path $z = L$, for $\ell=0$, 0.1×10^{-6}, 0.3×10^{-6} mm.*
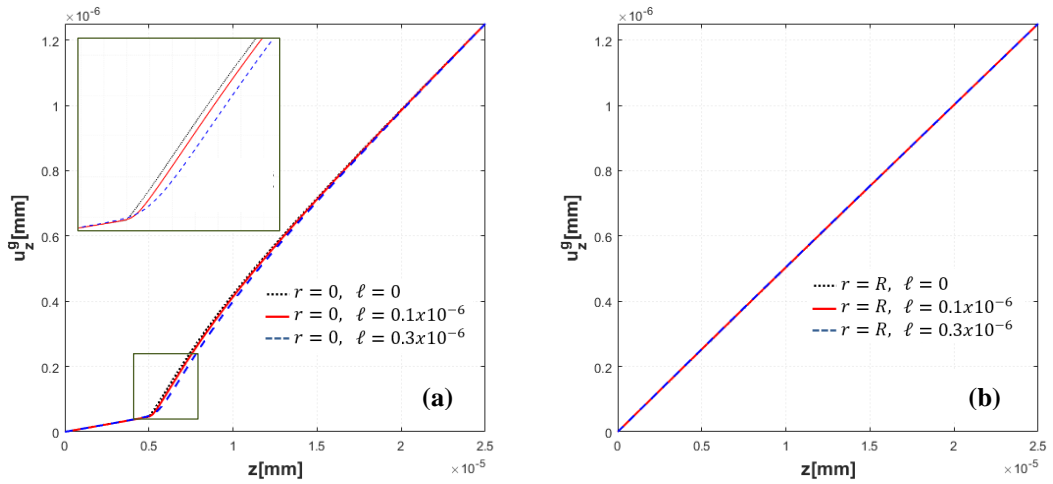
Figure 5.7 *– (a) u_z^g along the path $r = 0$, (b) u_z^g along the path $r = R$, for $\ell=0$, 0.1×10^{-6}, 0.3×10^{-6} mm.*

Figure 5.8(a) presents ε_r^g (radial normal strain) along the path $z = 0$ which is compressive due to Poisson effect. It can be seen that the magnitude of the strain is minimum at the center of the inclusion and slightly increases until the material interface. After the interface the magnitudes of strains significantly increase and

reach to a maximum value which are followed by a decrease and a saturation behavior. The responses are similar for all three ℓ values considered. Maximum value of the strain magnitude (minimum value of compression) slightly decreases with an increase of ℓ. Figure 5.8 (b) shows ε_z^g (longitudinal normal strain) along the path $z = 0$ which is parallel to the loading axis. The increase in ℓ causes higher strains in the inclusion (near the interface) and lower strains in the matrix. The longitudinal normal strain ε_z^g approaches to the macroscopic tensile strain 0.05 for $r > 10$ nm. The strain components ε_r^g and ε_z^g for the path $z = L$ are not shown, because they are almost constant and do not depend on ℓ.

Figure 5.9 (a) illustrates ε_r^g along the path $r = 0$ which is very similar to ε_r^g along the path $z = 0$, see Figure 5.8 (a). Figure 5.9 (b) shows ε_z^g along the path $r = 0$. It is seen that normal strain is very low inside the inclusion and rapidly raises after the interface reaching a value $\varepsilon_z^g \approx 0.08$ which is larger than the macroscopic tensile strain 0.05. After the maximum value, ε_z^g starts to decrease and drops almost to macroscopic value. In general, it can be concluded that the increase in ℓ causes a more diffused strain profile around the interface. In other words, strain magnitudes increase in the inclusion and decrease in the matrix with the increase in ℓ. Since the strain components ε_r^g and ε_z^g for the path $r = R$ are almost constant and do not depend on ℓ, they are not shown.
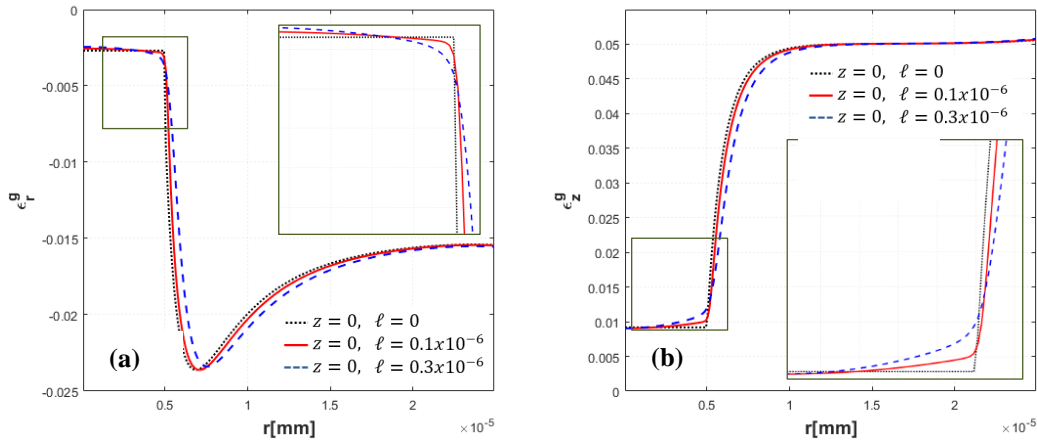
Figure 5.8 – (a) ε_r^g along the path $z = 0$, (b) ε_z^g along the path $z = 0$, for $\ell=0$, 0.1×10^{-6}, 0.3×10^{-6} mm.
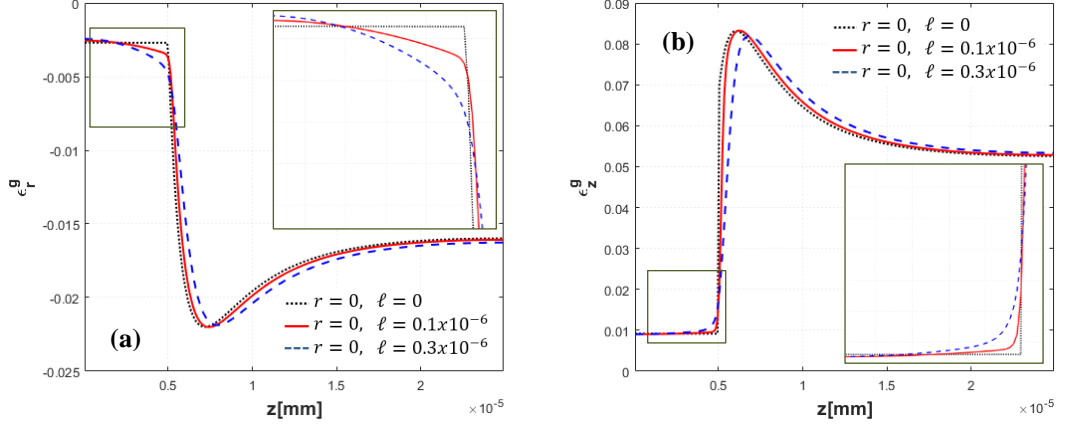
Figure 5.9 – (a) ε_r^g along the path $r = 0$, (b) ε_z^g along the path $r = 0$, for $\ell=0$, 0.1×10^{-6}, 0.3×10^{-6} mm.

Figure 5.10(a) demonstrates σ_r^g (radial normal stress) along the path $z = 0$ which is compressive throughout the domain. The stress magnitude is higher and almost constant in the inclusion for $\ell = 0$ (the local model), but it decreases for larger ℓ values. On the other hand, the stress magnitude is not constant in the inclusion for the gradient model and decreases towards the material interface. The normal stress σ_r^g curves approaches to the same value as one goes away from the interface ($r > 20$ nm) along the path $z = 0$. Figure 5.10(b) shows σ_z^g (longitudinal normal stress) along the path $z = 0$ which is tensile throughout the domain. The stress magnitude is lower and almost constant in the inclusion for the local model, whereas it increases with increasing ℓ. This effect is more pronounced especially close to the interface and for higher ℓ values. Before reaching to the material interface, the stress σ_z^g reaches to a peak value and then decreases. The normal stress σ_z^g curves almost coincide as one goes away from the interface ($r > 10$ nm) along the path $z = 0$.

Figure 5.11(a) depicts σ_r^g along the path $r = 0$. The stress of the local model is compressive and constant in the inclusion. However, for the gradient models the stress σ_r^g shows considerable variation in the inclusion. An increase in ℓ causes a decrease in stress magnitude close to the center, and increase towards the material interface. At the material interface, the local model demonstrates a sharp tensile stress peak, while the proposed gradient model diffuses the stress and lowers the

peak value. The normal stress σ_r^g curves almost coincide away from the interface ($z > 10$ nm) along the path $r = 0$. Figure 5.11(b) presents σ_z^g along the path $r = 0$. The stress σ_z^g of the local model is tensile and constant in the inclusion, while it shows a slight variation for the gradient model. After the material interface, stress has a peak value which is almost the same for the local model and the gradient model. After the peak value, stress curves shift to the right with increasing value of ℓ. The stresses σ_z^g of all models approach to the same value for $z > 20$ nm.
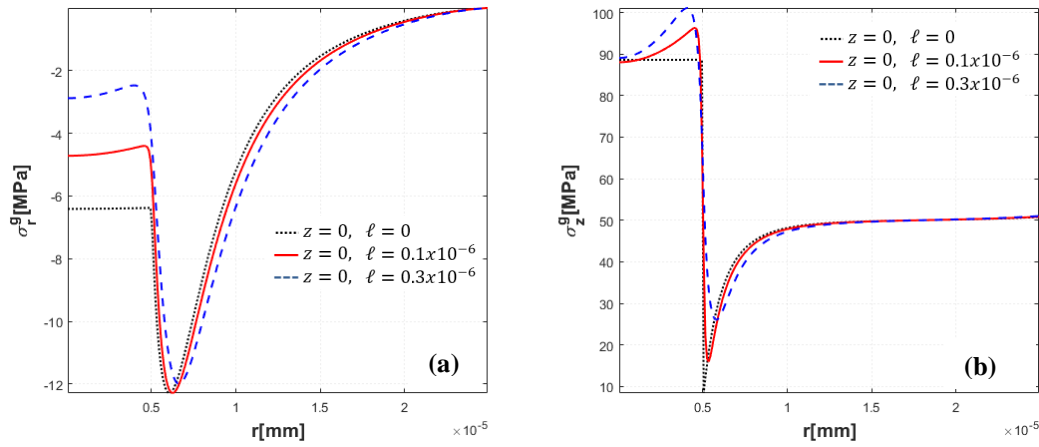
Figure 5.10 – (a) σ_r^g along the path $z = 0$, (b) σ_z^g along the path $z = 0$, for $\ell=0, \, 0.1 \times 10^{-6}, \, 0.3 \times 10^{-6}$ mm.
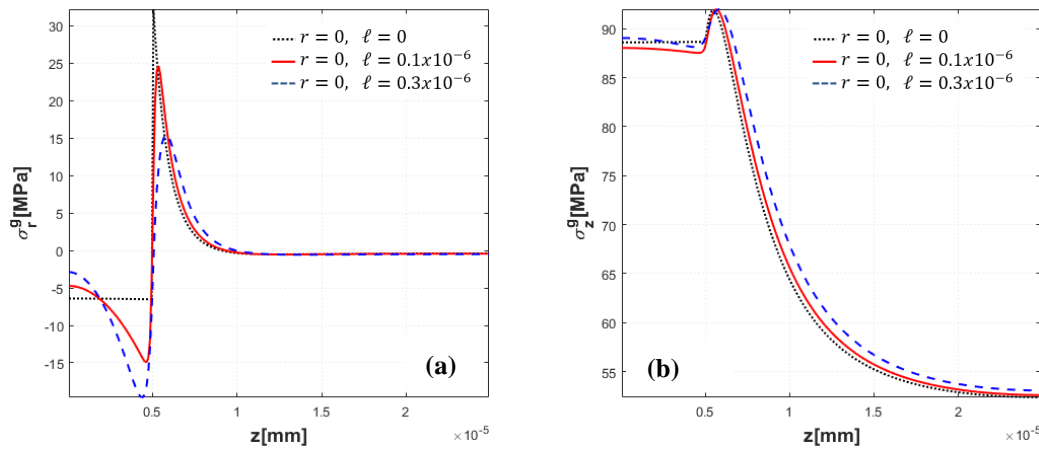
Figure 5.11 – (a) σ_r^g along the path $r = 0$, (b) σ_z^g along the path $r = 0$, for $\ell=0, \, 0.1 \times 10^{-6}, \, 0.3 \times 10^{-6}$ mm.

Figure 5.12 (a) and (b) show σ_r^g and σ_z^g stress contours, respectively, for the local elasticity solution, while the contours of σ_r^g and σ_z^g components of stress for the proposed model are given in Figure 5.12 (c) and (d), respectively. It can be seen from the figures that the stress field around the inclusion is smoothed for the proposed gradient model while it is very similar to local elasticity solution away from the inclusion.
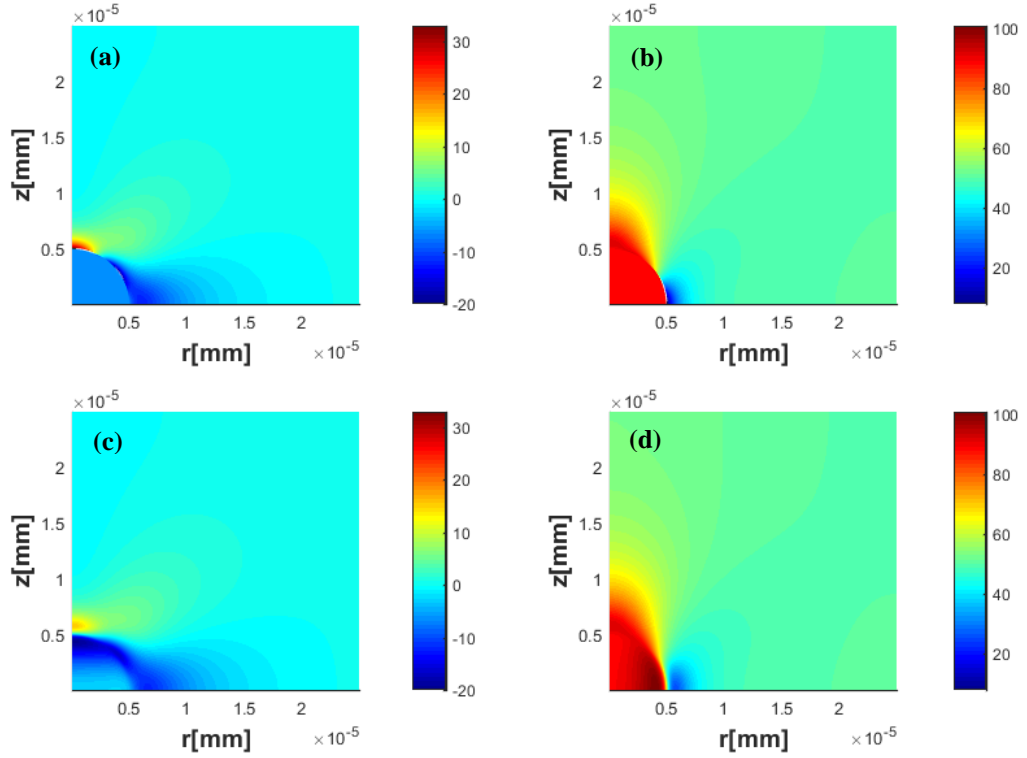
Figure 5.12 – (a) Variation of σ_r^g for $\ell = 0$, (b) variation of σ_z^g for $\ell = 0$, (c) variation of σ_r^g for $\ell=0.3\times10^{-6}$ mm and (d) variation of σ_z^g for $\ell=0.3\times10^{-6}$ mm.

The proposed gradient model removes or smoothens the discontinuities or sharp changes at the interfaces for the fields E^g, G^g, and thus also for $u^g, \varepsilon^g, \sigma^g$. Furthermore, the results converge to local solution for vanishing ℓ. It can also be seen from Figure 5.5 to Figure 5.12 that the E-grad model affects the region close to the material interface and the results converges to the local solution far from the material interface even for large ℓ values.

5.3.2. Comparison with Literature

In this section, a numerical example from literature (Wang et al., 2016) is considered and solved by the E-grad model for comparison. Wang et al. (2016) proposed a micromechanics based annular coated inclusion model and compared the results with the experiments conducted with a polyimide/silica nanocomposite (Abbate et al., 2004). The relevant elastic parameters of Wang et al. (2016) for the proposed gradient model and the considered length scale parameter ℓ are given in Table 5.2. These parameter sets correspond to the Poisson's ratios of $\nu_M = \nu_I = 0.4$ for the matrix and the inculsion, respectively. The elastic parameters given in Table 5.2 are identical with the values used in the coated inclusion model of Wang et al. (2016). However, the annular coated inclusion model requires three additional constants. These constants are the thickness for the interphase, which is a transition region from the nano-inclusion to the matrix, and the two elastic constants of the isotropic linear elastic interphase. The length scale parameter ℓ of the proposed gradient model can be related to the thickness of the interphase of the annular coated inclusion model.

A representative volume element in the form of a cylinder similar to Figure 4. is considered in this study to compare to the micromechanical model of Wang et al. (2016). In Abbate et al. (2004) test results are given for various volume fractions. In the axisymmetric finite element simulations corresponding volume fractions are obtained by keeping the radius of the inclusion constant at 35 nm and by changing the radius and the length of the cylindrical rod while keeping the aspect ratio the same. The geometric parameters of the models are given in Table 5.3.

Table 5.2 – Material parameters for literature problem

E_M [MPa]	G_M [MPa]	E_I [MPa]	G_I [MPa]	$\ell = \ell_r = \ell_z$ [mm] $\times 10^{-6}$
1960	700	88700	31679	0-6

Table 5.3 – Geometry parameters for literature problem

% VF	r_I [mm] × 10^{-6}	R [mm] × 10^{-6}	$2L$ [mm] × 10^{-6}
4.28	35	87.5	175
8.04	35	70.7	141.4
10.7	35	64.4	128.8
14.3	35	58.5	116.9

As shown in previous chapter, the proposed E-grad model shows a gradual decrease in elastic parameters in the inclusion and a gradual increase in elastic parameters in the matrix. This is not realistic for polymer nanocomposite materials where the polymer close to nano-inclusion becomes denser and stiffer, while the properties of the nano-inclusion is not affected (Malagù, et al., 2017). Therefore, different from the previous section, in current examples E and G values are specified as boundary condition at the material interface and Eqn. (5.13) is solved only for polyimide matrix while material parameters of the inclusion region are set to constant values given in Table 5.2. This is done in order to ensure that no softening takes place in the silica inclusion, because it is seen from the SEM micrographs that silica particles do not degrade in the nanocomposite. Furthermore, Abbate et al. (2004) commented that an adhesion is developed between the polyimide matrix and the silica inclusion, while weak van der Waals type adhesion is observed in some other studies (Malagu et al., 2017). Therefore, stiffening of the matrix at the interface is considered as reasonable for this nanocomposite. Figure 5.13(a) shows that the material properties obtained with the E-grad model when the boundary condition is applied to the interface. As can be seen from the figure, E^g is constant in the inclusion and varies only in the matrix region. Figure 5.13(b) presents that, for high values of ℓ and high volume fractions, modulus cannot diffuse out before reaching the external boundary of the geometry.
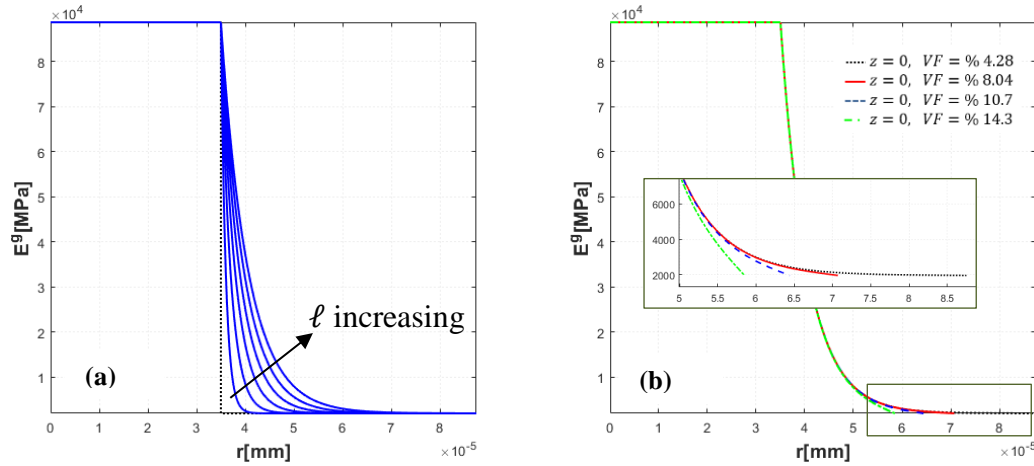
Figure 5.13 *– Variation of E^g along the path $z = 0$, (a) for VF=%4.28 and $0 \leq \ell$ $\leq 6 \times 10^{-6}$ mm, (b) for VF=%4.28, %8.04, %10.7, %14.3 and $\ell = 6 \times 10^{-6}$ mm*

Figure 5.14 compares the Young's modulus values computed by the E-grad model, the micromechanics model of Wang et al. (2016) and the test results of Abbate et al. (2004). The Young's modulus is computed with the proposed approach for seven different ℓ values and for different volume fractions. A response very similar to the coated inclusion model is obtained by varying the length scale ℓ. Different solid curves in Figure 5.14 correspond to the responses of the annular coated inclusion model for various interphase thicknesses. In the annular coated inclusion model, the overall modulus of the composite increases as the interphase thickness increases provided that the stiffness of the interphase is larger than the matrix. A nonlinear behavior is observed with increasing volume fraction of the inclusion at constant ℓ. The nonlinearity is more pronounced for higher values of ℓ. If ℓ value is chosen in the range $3 \times 10^{-6} < \ell < 4 \times 10^{-6}$ mm then a reasonable agreement with the experiment is achieved. It can be seen that for low volume fractions, ℓ makes small difference while its effect becomes more significant with increasing volume fraction of the inclusion.

The results obtained by the proposed approach capture the experimentally measured values of the nanocomposite modulus. Moreover, the put forward gradient model, based on a relatively basic modeling consideration and a computationally efficient approach, is able to predict the computationally more expensive and complex

micromechanically-based model's results
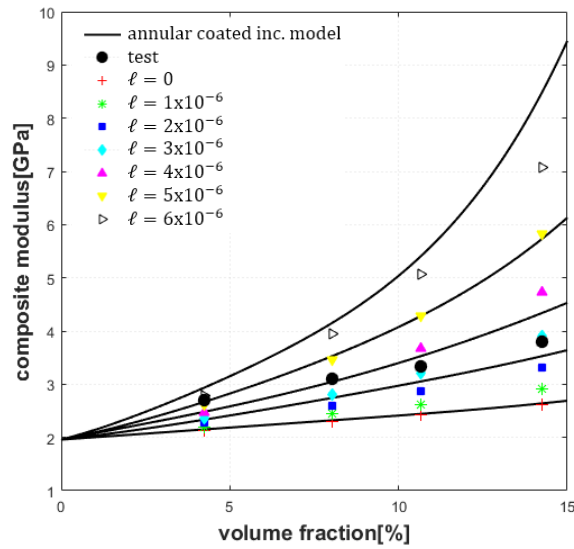
Figure 5.14 *– Variation of the macroscopic Young's modulus of the nanocomposite with volume fraction for various length scales, $0 \leq \ell \leq 6 \times 10^{-6}$ mm. The solid curves correspond to the results of the annular coated inclusion model (Wang et al., 2016) for interphase thicknesses of 0, 10, 15, 20 and 25 nm, while the black circles are the experimental results (Abbate et al., 2004).*
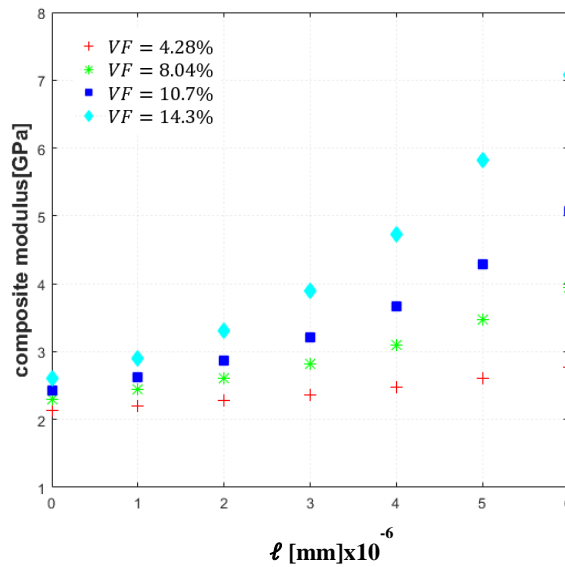
Figure 5.15 *– Variation of the macroscopic Young's modulus of the nanocomposite with ℓ for various volume fractions VF=%4.28, %8.04, %10.7, %14.3*

97

Figure 5.15 compares the Young's modulus values computed by the proposed model with increasing ℓ for different inclusion volume fractions of the considered literature problem. It can be seen that, composite modulus values increase with increasing inclusion volume fraction for constant ℓ. The composite modulus also increases with increasing ℓ for constant volume fraction. Although, a slight nonlinearity is seen for the lowest volume fraction, it is more pronounced for higher volume fractions.

5.3.3. Generation of Anisotropy

As stated in previous sections, by assuming different ℓ values in r and z directions, different modulus variations can be obtained in the considered directions. Figure 5.16 shows E-modulus variations in $z = 0$ and $r = 0$ for the problem in previous section at 4.28% volume fraction, for different combinations of length scale parameters ℓ: (case 1) $\ell_r = \ell_z = 1 \times 10^{-6}$ mm, (case 2) $\ell_r = 1 \times 10^{-6}$mm, $\ell_z = 6 \times 10^{-6}$ mm and (case 3) $\ell_r = 6 \times 10^{-6}$ mm, $\ell_z = 1 \times 10^{-6}$ mm. As can be seen from the figure, by changing ℓ, different modulus variations are obtained in different directions. By assuming the load case in the previous section, the Young's modulus of the nanocomposite is computed and the results are shown in Table 5.4. Note that, different modulus values are obtained for each combination. As expected, higher modulus is obtained with the increase in ℓ. Because the loading is in z direction, ℓ_z has a more pronounced effect in composite modulus. As a result of the difference in ℓ_r and ℓ_z values, anisotropic macroscopic behavior is obtained even for a nanocomposite having a spherical inclusion and consisting of isotropic linear elastic constituents.

Table 5.4 – *Macroscopic Young's modulus of the nanocomposite in z-direction for different combinations of the length scale parameters ℓ_r and ℓ_z*

VF = 4.28 %	ℓ_r [mm] × 10^{-6}	ℓ_z [mm] × 10^{-6}	E [GPa]
case 1	1	1	2.20
case 2	1	6	2.48
case 3	6	1	2.42
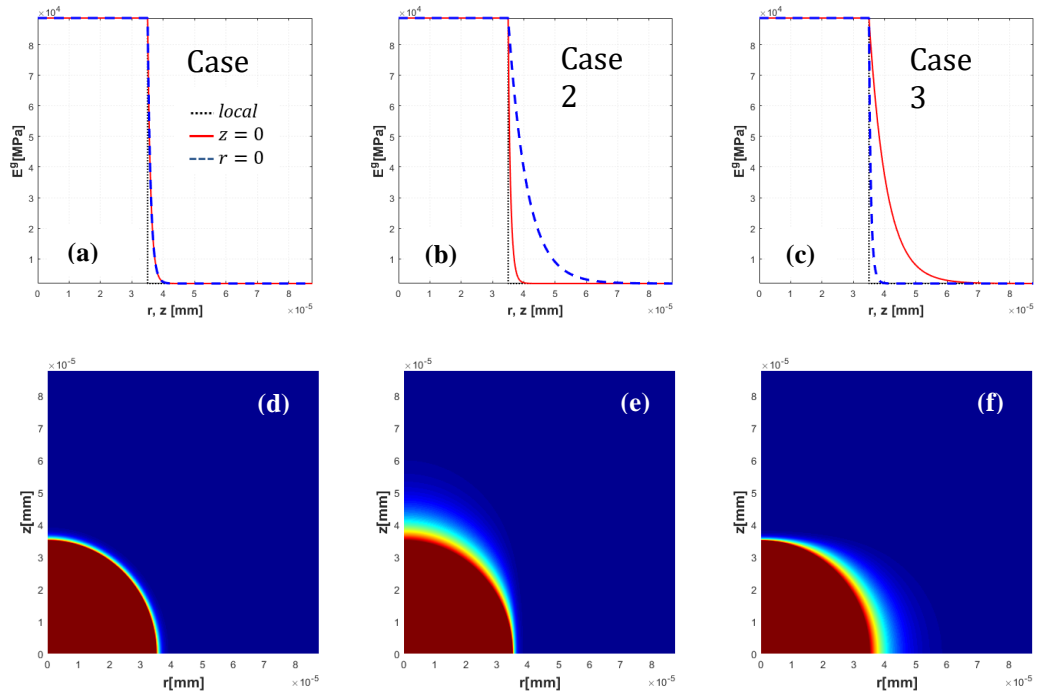
Figure 5.16 – *Variation of E^g along the path $r = 0$ and $z = 0$ for (a) $\ell_r=\ell_z=1\times10^{-6}$ mm, (b) $\ell_r=1\times10^{-6}$ mm, $\ell_z=6\times10^{-6}$ mm, (c) $\ell_r=6\times10^{-6}$ mm, $\ell_z=1\times10^{-6}$ mm. Variation of E^g in the entire domain for (d) $\ell_r=\ell_z=1\times10^{-6}$ mm, (e) $\ell_r=1\times10^{-6}$ mm, $\ell_z=6\times10^{-6}$ mm, (f) $\ell_r=6\times10^{-6}$ mm, $\ell_z=1\times10^{-6}$ mm*

CHAPTER 6

MODELING THE STATISTICAL DISTRIBUTION OF FIBERS IN A MATRIX

As stated before, an ideal candidate for a nano-reinforcement material is CNT. There are experimental and computational studies discussing the effect of CNTs in polymers, metals, ceramics (Bai and Allaoui, 2003, Wang et al., 2013, Bakshi et al. 2011). In addition to continuum formulations (Wernik and Meguid, 2010, Tserpes et al., 2008), atomistic simulations (Arash et al., 2015, Jensen et al., 2016, Malagu et al., 2017) are also carried out to model the CNT reinforced nano-composites.

CNTs are generally distributed in a matrix material in different orientations. To account for this orientation distribution, atomistic and micromechanical models are used in literature (Odegard et al., 2003, Arash et al., 2015, Malagu et al., 2017). For the modeling of orientation of collagen fibers in arterial layers, Gasser et al. (2006) proposed a Gaussian like distribution function in a structural tensor formulation. Later, this model is used to model different biological tissues: human cornea (Pandolfi and Holzapfel, 2008), articular cartilage (Ateshian et al., 2009), posterior scleral (Girard et al., 2009). Pandolfi and Vasta (2012) and Cortes and Elliot (2014) and also proposed higher order corrections to the structural tensor model with fiber distribution. In biological tissues collagen fibers do not carry compressive load and the fibers under compression are disregarded with a tension-compression switch (Gasser et al., 2006, Holzapfel and Ogden, 2015, Latorre and Montans, 2016).

Malagu et al. (2017) studied a CNT reinforced polymer both in molecular dynamics and micromechanics. In this study, some further investigations are made based on the work of Malagu et al. (2017). To this end, E-grad model proposed in previous chapters is used for the modeling of a representative volume element. Then, by distributing the RVEs statistically, nanocomposite material properties are obtained.

6.1. PROBLEM DESCRIPTION

6.1.1. Local Assumption

In the work of Malagu et al. (2017) on CNT reinforced polymer composites, different regions around the CNT were identified by using molecular dynamics (MD) simulations, see Figure 6.1. As can be seen from Figure 6.1, after the CNT layer, an empty space is present which is a result of the Van der Walls interaction. They named this region as the interface ('if' in the figure). After the interface, Malagu et al. (2017) observed ordered polymer layers. They named these ordered layers as the interphase ('ip' in the figure). After the interphase, the bulk polymer matrix is present. By MD simulations, it was shown that during deformation almost all the internal energy is carried by the interphase and the bulk polymer while the CNT and the interface have stored negligible energy. Therefore, they commented that the interphase region is mainly responsible for the strengthening mechanism for non-functionalized CNT reinforced polymer composites.

Figure 6.1 *– Side and cross section views of considered geometry for the MD model in Malagu et al. (2017) (not to scale)*

By neglecting the CNT and interface regions, Malagu et al. (2017) considered the interphase as an equivalent fiber embedded in the bulk polymer, see Figure 6.2. They considered the interphase as a homogeneous material and by equating the strain energy of MD and strain energy FE models, they obtained the Young's modulus E and the Poisson's ratio v of the interphase for various CNT diameters, see Table 6.1. As can be seen from the table, the Young's modulus of interphase E_{IP_Malagu} is

significantly higher than the bulk polymer E_M. Furthermore, when compared with the bulk polymer, the Young's modulus of the interphase increases with the CNT diameter while v decreases. Note that, the shear modulus values in Table 6.1 are computed from E and v.

Figure 6.2 *– Side view of considered geometry for the FE model in Malagu et al. (2017) (not to scale)*

Table 6.1 *– Calculated homogenized interphase elastic constants in Malagu et al. (2017)*

CNT	E_{IP_Malagu} [MPa]	v_{IP_Malagu}	G_{IP_Malagu} [MPa]	E_M [MPa]	v_M	G_M [MPa]
(8×8)	6249	0.300	2403			
				3040	0.36	1118
(12×12)	7195	0.283	2803			

6.1.2. E-grad model

Although Malagu et al. (2017) considered the interphase as a homogeneous material with constant tensile modulus E, and shear modulus G, they also found in the MD simulations that the density of the interphase decreases from the interface to the bulk polymer. This behavior has been seen in other studies as well, see Wei et al. (2004), Karatrantos et al. (2016). Therefore, it is reasonable to assume that the Young's modulus decreases from the interface to the bulk polymer rather than being constant in the interphase. In this section, the gradual variation of E is considered by using

103

the E-grad model discussed before.

In order to determine the values of E and G for the E-grad model at the inner and outer boundaries of the interphase region, it is assumed that E and G at the inner surface of the interphase, which is in contact with the interface, gradually decrease from $E = E_I$ and $G = G_I$ to the value of the bulk polymer $E = E_M$ and $G = G_M$ at the outer surface of the interphase as shown in Figure 6.3. The values of E_M and G_M are governed by the material parameters of the bulk polymer, while the values of E_I and G_I at the inner surface of the interphase are not yet known and are found as follows. The volumes under the E and G surfaces obtained by the E-grad model over the interphase are computed, and these volumes are divided by the volume of the interphase. The integral is taken over the circular tubular cross-sectional area of the interphase with the inner and outer radii of the interphase. This way the average values of E and G of the E-grad model for the interphase are obtained. Then these values are equated to the corresponding Young's modulus and shear modulus values of the effective fiber obtained in Malagu et al. (2017), as shown in Table 6.1. With an iterative study, it is seen that, for values of ℓ_r greater than 5×10^{-7} mm, the E^g curve is almost horizontal at the interphase-bulk matrix intersection. Therefore, $\ell_r = 5 \times 10^{-7}$ mm is selected as the highest value, see Figure 6.5.
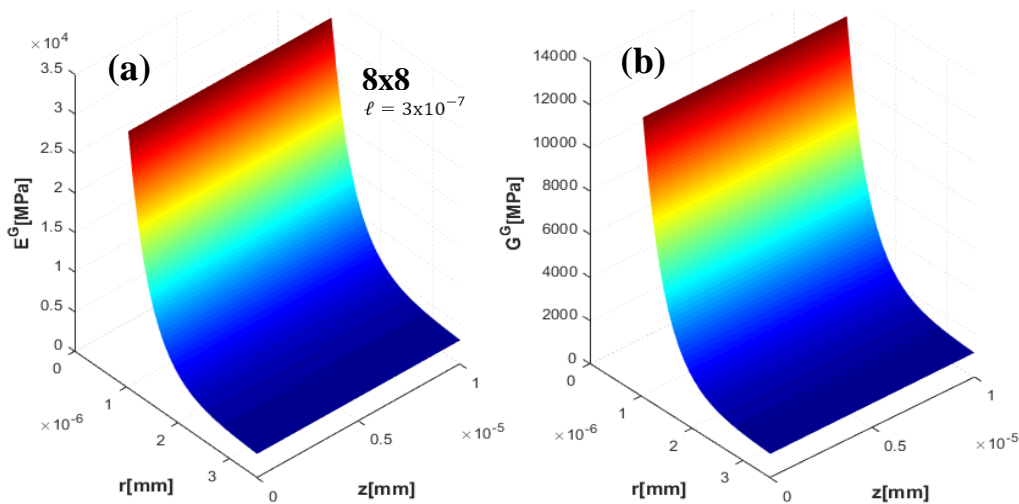
Figure 6.3 – (a)E, (b) G variations for $\ell_r = 3 \times 10^{-7}$ mm for (8×8) CNT with E-grad model

A detailed investigation of the problem with the E-grad model is provided further.

The geometry, FE mesh, boundary conditions for E-field and boundary conditions for the mechanical problem are given in Figure 6.4. An axisymmetric FE model is considered. The problem parameters are provided in Table 6.2 for (8×8) and (12×12) CNTs. Two different length scale parameters are considered for the E-grad model, $\ell_r = 3 \times 10^{-7}$ mm and $\ell_r = 5 \times 10^{-7}$ mm. For both values of ℓ_r, E_I and G_I are determined as explained above. It is assumed that E does not vary in the axial direction and ℓ_z is considered to be 0. The calculated E_I and G_I values are also provided in Table 6.2. It can be seen that E_I and G_I values are higher for the lower ℓ_r. For the (12×12) CNT, E_I values are higher compared to the (8×8) CNT. Note that the calculated E_I values at the inner surface of the interface are much higher than the local values, i.e., uniform material properties of the interphase given in Table 6.1. In literature, it is reported that while low density polyethylene (PE) has elastic modulus in the 0.1-1 GPa range, while highly crystalline ultra-high molecular weight PE fibers can have moduli as high as 117 GPa (Coleman et al. 2006, Callister 2003). Therefore, very high E values at the inner surface of the interphase are reasonable.
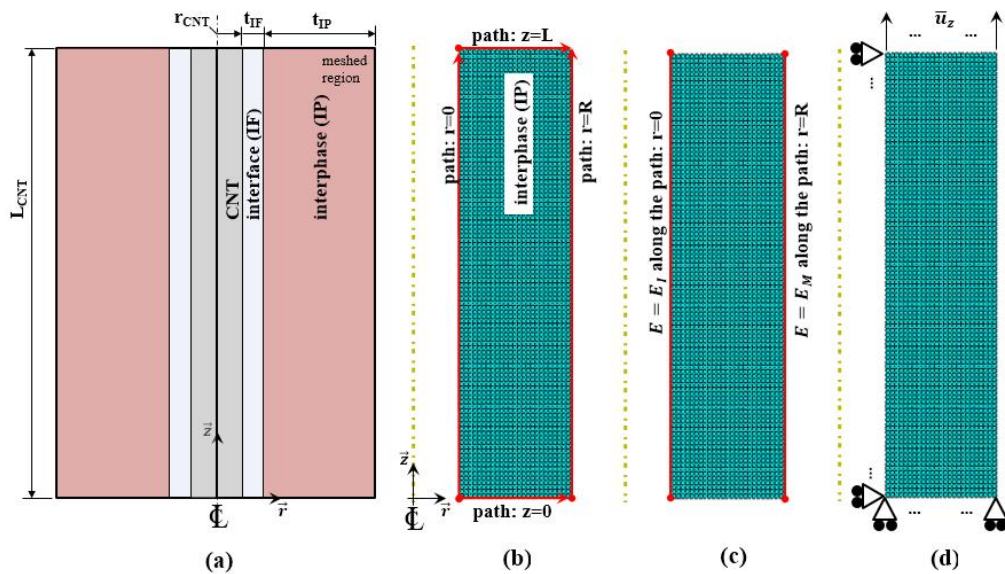
Figure 6.4 *– 2D axisymmetric E-grad model (a) geometry, (b) FE mesh, (c) boundary conditions for E field solution, (d) boundary conditions for mechanical problem*

Table 6.2 – Material parameters for the 2D axisymmetric E-grad model.

	ℓ_r [mm] x10⁻⁷	ℓ_z [mm] x10⁻⁷	L_{CNT} [mm] x10⁻⁷	r_{CNT} [mm] x10⁻⁷	t_{IF} [mm] x10⁻⁷	t_{IP} [mm] x10⁻⁷	$E_{r0} = E_I$ [MPa]	$G_{r0} = G_I$ [MPa]	$E_{rR} = E_M$ [MPa]	$G_{rR} = G_M$ [MPa]
(8×8)	3	0	100	5.4	5	25	55000	21912	3040	1118
	5	0	100	5.4	5	25	32500	12974	3040	1118
(12×12)	3	0	100	10.1	5	25	64000	26230	3040	1118
	5	0	100	10.1	5	25	38250	15612	3040	1118

Figure 6.5 shows the variations of E and G along the path $z = 0$ for $\ell_r = 3 \times 10^{-7}$ mm, $\ell_r = 5 \times 10^{-7}$ mm and the uniform values of E and G found in Malagu et al. (2017). For the lower value of ℓ_r, E starts from a higher value and shows a steep decrease at the beginning and converges to the Young's modulus of the bulk polymer E_M =3040 MPa. For the higher value of ℓ_r, E starts from a lower value and does not show a decrease as steep as the former one.

Figure 6.6 compares the variation of E for the (8×8) and (12×12) CNTs along the path $z = 0$. Although, similar trends are seen for both CNTs, the modulus values of the (12×12) CNT at the inner surface of the interphase is higher than the modulus values of the (8×8) CNT. Note that the radius of the (12×12) CNT is higher than the radius of the (8×8) CNT. The interface and interphase thicknesses are considered to be equal for both CNTs as reported by Malagu et al. (2017).
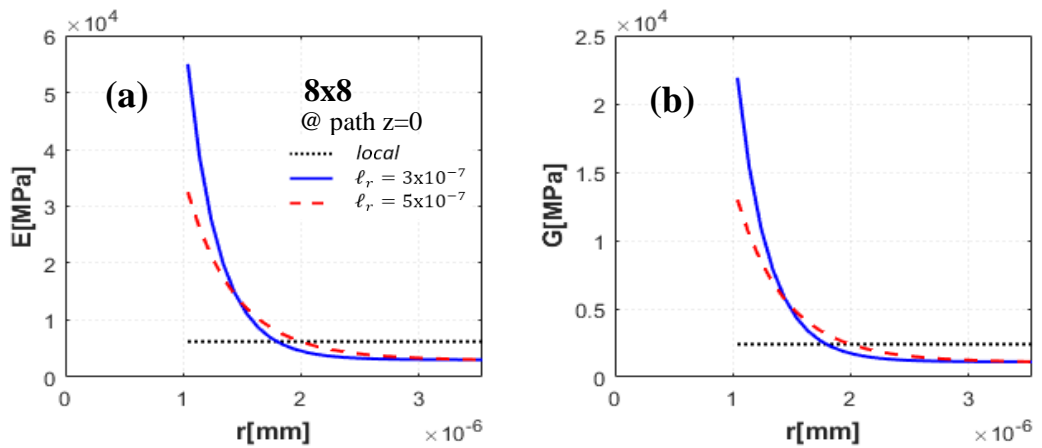
Figure 6.5 – *Variation of (a)E, (b) G for ℓ$_r$=0, 3×10^{-7}, 5×10^{-7} mm along the path $z = 0$. (8 × 8) CNT is considered*

u, ε and σ fields for (8×8) CNT

Having determined the distributions of the Young's modulus and the shear modulus, a tensile test is conducted by applying a prescribed displacement $\bar{u} = L_{CNT}/100$ in the z-direction, as shown in Figure 6.4(d).

Figure 6.7(a) shows the variation of radial displacement u_r along the path $r = R$. For all the cases u_r values are constant along the path. u_r values of the E-grad model

are higher than the local one. Furthermore, u_r has the highest magnitude for $\ell_r = 3 \times 10^{-7}$ mm. The variation of u_r along the path $z = 0$ is depicted in Figure 6.7(b). Although, there is small difference between the results, for the E-grad model u_r values are higher than the local one at the outer surface. For $\ell_r = 3 \times 10^{-7}$mm, u_r has the highest magnitude.
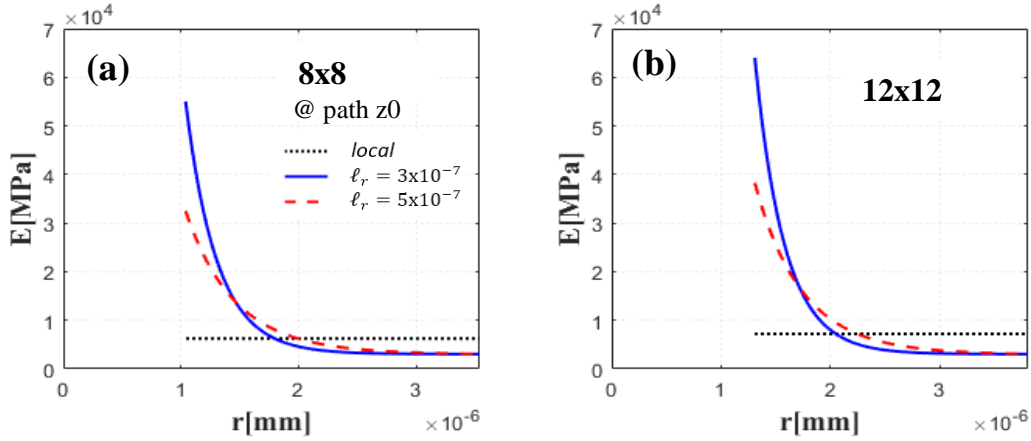
Figure 6.6 *–Variation of E along the path* $z = 0$ *for (a)* (8×8) *CNT, (b)* (12×12) *CNT for* $\ell_r=0$, 3×10^{-7}, 5×10^{-7} *mm are considered*
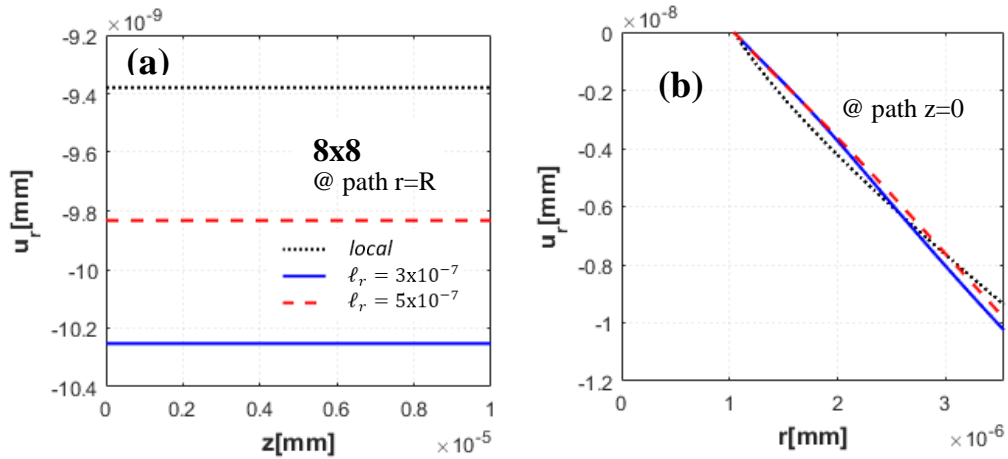
Figure 6.7 *– (a) Variation of* u_r *along the path* $r = R$, *(b) variation of* u_r *along the path* $z = 0$ *for* (8×8) *CNT for* $\ell_r=0$, 3×10^{-7}, 5×10^{-7} *mm are considered*

Figure 6.8(a) and (b) depict the normal stresses σ_r and σ_z along the path $r = 0$, respectively. σ_r values are constant for all the cases but the results of E-grad model

108

are higher than the local one. For $\ell_{\mathrm{r}} = 3 \times 10^{-7}$ mm, σ_r and σ_z have the highest magnitude. σ_z values for the E-grad model are much higher than the local stress. These high stress values are important for the evaluation of the strength of the composites. The elastic modulus can be increased with the addition of nano-inclusion, but the strength of the composite may be decreased due to this dramatic increase in stress. In other words, the strength predictions of the models with gradually varying interphase and uniform interphase models could be very different, although their stiffness predictions do not show significant difference.

Figure 6.9(a) illustrates the variation of σ_r along the path $r = R$. Because it is a free surface, the stress values are almost zero for all cases. The variation of σ_z along the path $r = R$ is shown in Figure 6.9(b). For the local case, the Young's modulus is higher than the E-grad model along this path, therefore the stress value is higher for the local case. The results of the E-grad model are almost the same for $\ell_{\mathrm{r}} = 3 \times 10^{-7}$ mm and $\ell_{\mathrm{r}} = 5 \times 10^{-7}$ mm.

Figure 6.10(a) shows the variation of σ_r along the path $z = 0$. It can be seen that at the inner surface, σ_r magnitude decreases as ℓ_r increases. Furthermore, the values of σ_r for the E-grad model is substantially higher than the local case. All the curves go to zero at the free surface as expected. Figure 6.10(b) depicts σ_z variation along the path $z = 0$. It can be seen that at the inner surface, σ_z is considerably higher for the E-grad model than the local case. The normal stress σ_z is the highest for $\ell_r = 3 \times 10^{-7}$ mm, because the Young's modulus at the inner surface is the largest for this case. σ_z values converge to the same value at the outer surface of the interphase for the E-grad model, while σ_z is constant for the local elasticity model.
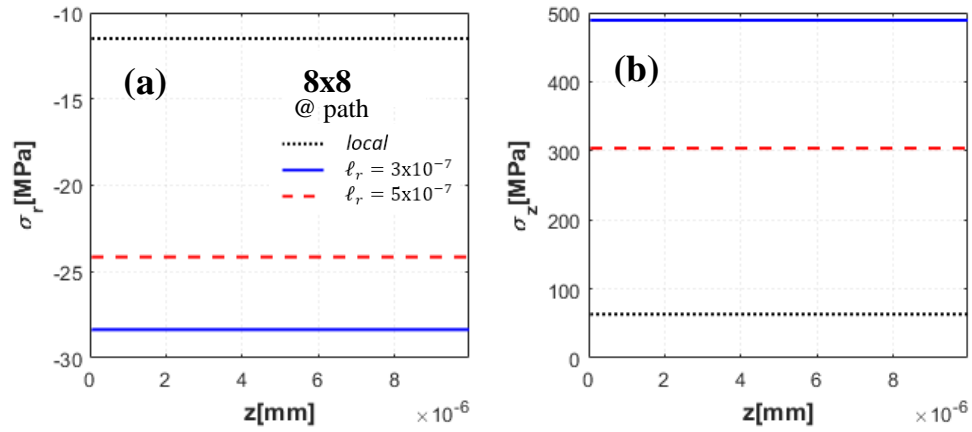
Figure 6.8 *– (a) Variation of σ_r along the path $r = 0$, (a) variation of σ_z along the path $r = 0$ for (8×8) CNT for $\ell_r=0$, 3×10^{-7}, 5×10^{-7} mm are considered*

Figure 6.9 *– (a) Variation of σ_r along the path $r = R$, (b) variation of σ_z along the path $r = R$ for (8×8) CNT for $\ell_r=0$, 3×10^{-7}, 5×10^{-7} mm are considered*

110

Figure 6.10 – *(a) Variation of σ_r along the path $z = 0$, (a) variation of σ_z along the path $z = 0$ for (8×8) CNT for ℓ_r=0, 3×10⁻⁷, 5×10⁻⁷ mm are considered*

6.2. HOMOGENIZED PROPERTIES AND STATISTICAL ORIENTATION OF FIBRES

6.2.1. (8×8) CNT embedded in interphase

In the previous section, polymer ordering around the CNT is considered only in radial direction. However, it is known that the ordering is also present at the tips of the CNTs in the axial direction, see Malagu et al. (2017), Wei and Srivastava (2004). Therefore, in this section, in addition to the interphase in radial direction, a gradually varying interphase from the tips of the CNT in axial direction is considered. For this purpose, an axisymmetric FE model of an embedded CNT is generated as depicted in Figure 6.11. All the dimensions are the same with the model in Figure 6.4 except the cap region.

Figure 6.11 (a) shows the geometry of the problem. The size of the interphase in axial direction is taken as $t_{cap} = 10 \times 10^{-7}$ mm following the molecular dynamics simulation results in Malagu et al. (2017). Figure 6.11 (b) presents the axisymmetric FE mesh and some predefined paths for post processing. The modulus boundary conditions for the E-grad model are demonstrated in Figure 6.11(c). $E = E_I =$

55000 MPa and $G = G_I = 21912$ MPa (values for (8×8) CNT and $l_r = 3 \times 10^{-7}$ mm given in Table 6.2) at the inner boundary, and $E = E_M = 3040$ MPa and $G = G_I = 1118$ MPa at the outer boundary are considered as boundary conditions.

Different ℓ values are considered in r and z directions because of the thickness differences of interphase in these directions. To this end, $\ell_r = 3 \times 10^{-7}$ mm in radial direction and $\ell_z = 1 \times 10^{-7}$ mm in axial direction are assumed. Figure 6.12 shows the variation of E along the predefined paths. Figure 6.12 (a) depicts that at path $r = 0$, E converges from E_I to E_M. At path $r = M$, E stays constant at $E = E_I$ and converges to E_M after the material corner. It can be seen that a small difference is observed between the path $r = 0$ and the path $r = M$. Along the path $r = R$, E value stays constant at $E = E_M$. As can be seen form Figure 6.12 (b), similar trend is also observed along the paths $z = 0, z = M$ and $z = L$. Compared to r paths the E variation is less steep because of higher ℓ_r value.
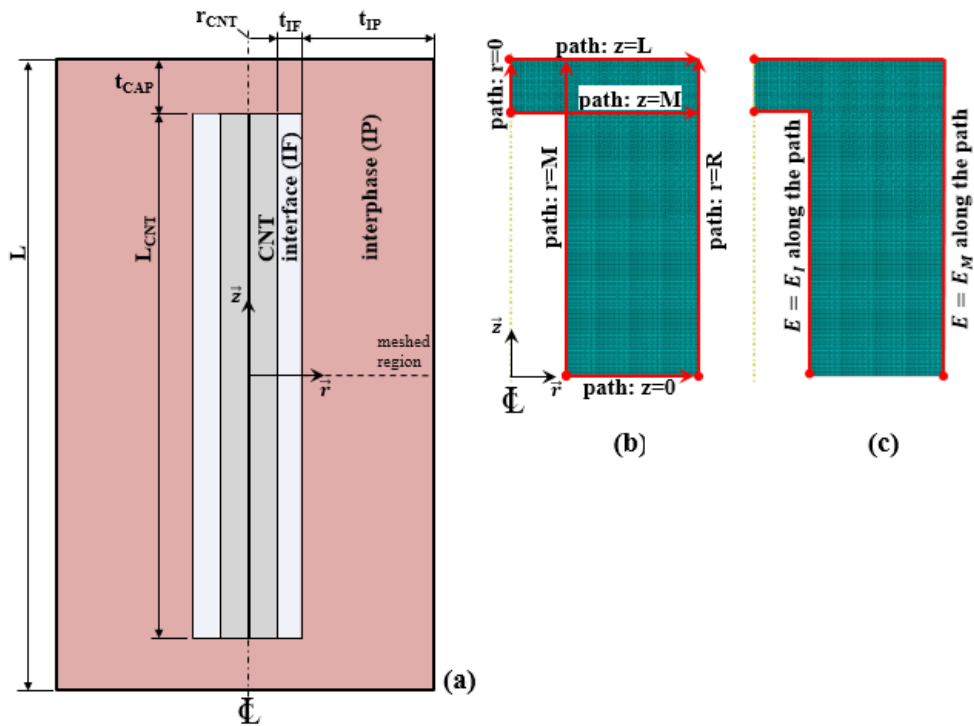
Figure 6.11 – *2D axisymmetric E-grad model (a) geometry, (b) FE mesh, (c) boundary conditions for E field solution*

112
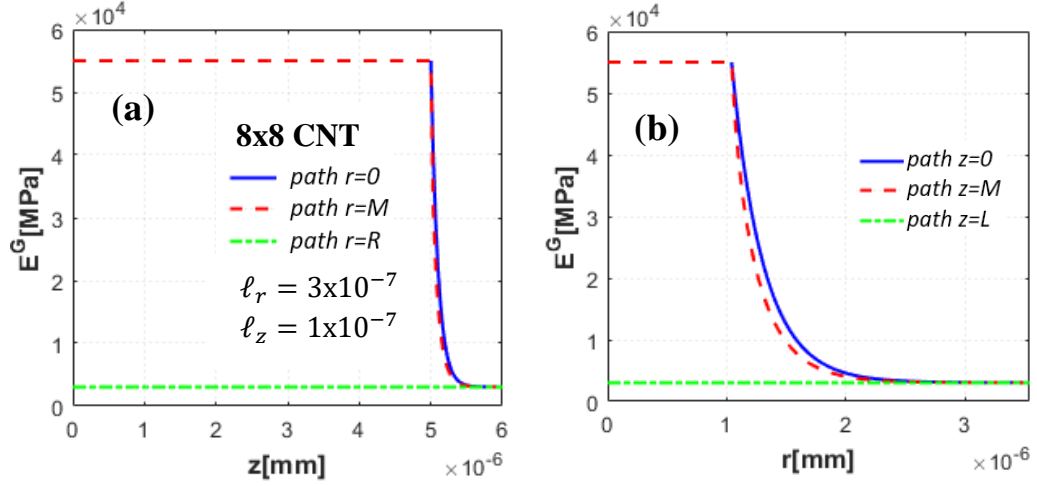
Figure 6.12 – *Variation of E along the path (a) r=0,M,R, (b) z=0,M,L, for ℓ_r=3×10^{-7} mm and ℓ_z=1×10^{-7}mm for* (8 × 8) *capped CNT*

6.2.2. Homogenized material properties of (8×8) CNT embedded in interphase

In this section, homogenized material properties, i.e., an effective fiber, of (8×8) CNT embedded in the interphase are found, see Figure 6.11. It is assumed that the homogenized material is a transversely isotropic with five independent elastic constants; $C_{11}, C_{12}, C_{13}, C_{33}, C_{44}$. For a transversely isotropic linear elastic material in 3D, the stress-strain relation $\boldsymbol{\sigma} = \mathbb{C}:\boldsymbol{\varepsilon}$ is given in cylindrical coordinates as:

$$\begin{bmatrix} \sigma_{rr} \\ \sigma_{\theta\theta} \\ \sigma_{zz} \\ \sigma_{\theta z} \\ \sigma_{rz} \\ \sigma_{r\theta} \end{bmatrix} = \begin{bmatrix} C_{11} & C_{12} & C_{13} & 0 & 0 & 0 \\ C_{12} & C_{11} & C_{13} & 0 & 0 & 0 \\ C_{13} & C_{13} & C_{33} & 0 & 0 & 0 \\ 0 & 0 & 0 & C_{44} & 0 & 0 \\ 0 & 0 & 0 & 0 & C_{44} & 0 \\ 0 & 0 & 0 & 0 & 0 & (C_{11}-C_{12})/2 \end{bmatrix} \begin{bmatrix} \varepsilon_{rr} \\ \varepsilon_{\theta\theta} \\ \varepsilon_{zz} \\ \varepsilon_{\theta z} \\ \varepsilon_{rz} \\ \varepsilon_{r\theta} \end{bmatrix} \quad (6.1)$$

For the calculation of the elastic constants, the strain energy of the graded material for various load cases is equated to the strain energy of a homogenized material with the same outer dimensions as shown in Figure 6.13.

For the calculation of the elastic constants, different load cases have to be applied on the geometries to generate different deformations. Two of the deformations are homogeneous, while the other three are inhomogeneous. Figure 6.14 shows the considered load cases to provoke different elastic constants. These load cases are

applied in a stepwise procedure which is explained below.
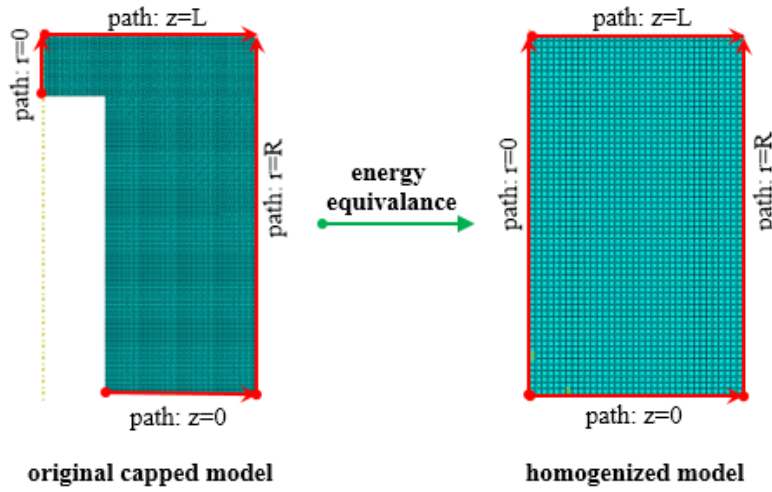
Figure 6.13 – *The models for which the strain energy equivalence are required. (a) Interphase of a (8×8) capped CNT with graded properties, (b) homogenized equivalent fiber model*

Step1, Consideration of Load Case 1: The following BCs are applied in this load case; $u_z = 0$ along path $z = 0$, $u_z = \bar{u}_z$ along path $z = L$, $u_r = 0$ along path $r = 0$, $u_r = 0$ along path $r = R$, see Figure 6.14(a). This uniform loading in z direction leads to a homogeneous strain condition for the homogenized model, i.e., $\varepsilon_r = 0$, $\varepsilon_z = 0.01$, $\varepsilon_\theta = 0$, $\varepsilon_{rz} = 0$. It means that the only active material constant is C_{33}. By equating the energy of the capped model to the homogenized model, it is found that $C_{33} = 6837.56$ MPa.

Step2, Consideration of Load Case 2: The following BCs are applied in this load case; $u_z = 0$ along path $z = 0$, $u_z = 0$ along path $z = L$, $u_r = 0$ along path $r = 0$, $u_r = \bar{u}_r$ along path $r = R$, see Figure 6.14(b). By prescribing this uniform loading in r direction, a homogeneous strain condition is obtained for the homogenized model such that $\varepsilon_r = 0.01$, $\varepsilon_z = 0$, $\varepsilon_\theta = 0.01$, $\varepsilon_{rz} = 0$. By equating the energy of the capped model to homogenized model, a relation is found between C_{11} and C_{12} as $C_{12} = 9154.44 - C_{11}$.

Step3, Use of Genetic Algorithm (GA) for Load Cases 3, 4 and 5: Other than the above load cases, it is not possible to generate an additional homogeneous strain

field which provides further identification of the unknown elastic constants. Therefore, inhomogeneous load cases are considered to identify the remaining unknown elastic constants. The following BCs are considered for the Load Case 3; $u_z = 0$ along path $z = 0, u_r = 0$ along path $z = 0$, $u_r = 0$ along path $r = R$, $u_z = \bar{u}_z = 0.01 \times z$ along path $r = R$, see Figure 6.14(c). For the Load Case 4; $u_z = 0$ along path $z = 0$, $u_z = \bar{u}_z = 0.02 \times r$ along path $z = L$, $u_r = 0$ along path $r = 0, u_r = 0$ along path $r = R$, see Figure 6.14(d). For the Load Case 5; $u_z = 0$ along path $z = 0$, $u_z = 0$ along path $z = L$, $u_r = 0$ along path $r = 0$, $u_r = \bar{u}_r = 0.6 - 0.01 \times z$ along path $r = R$.
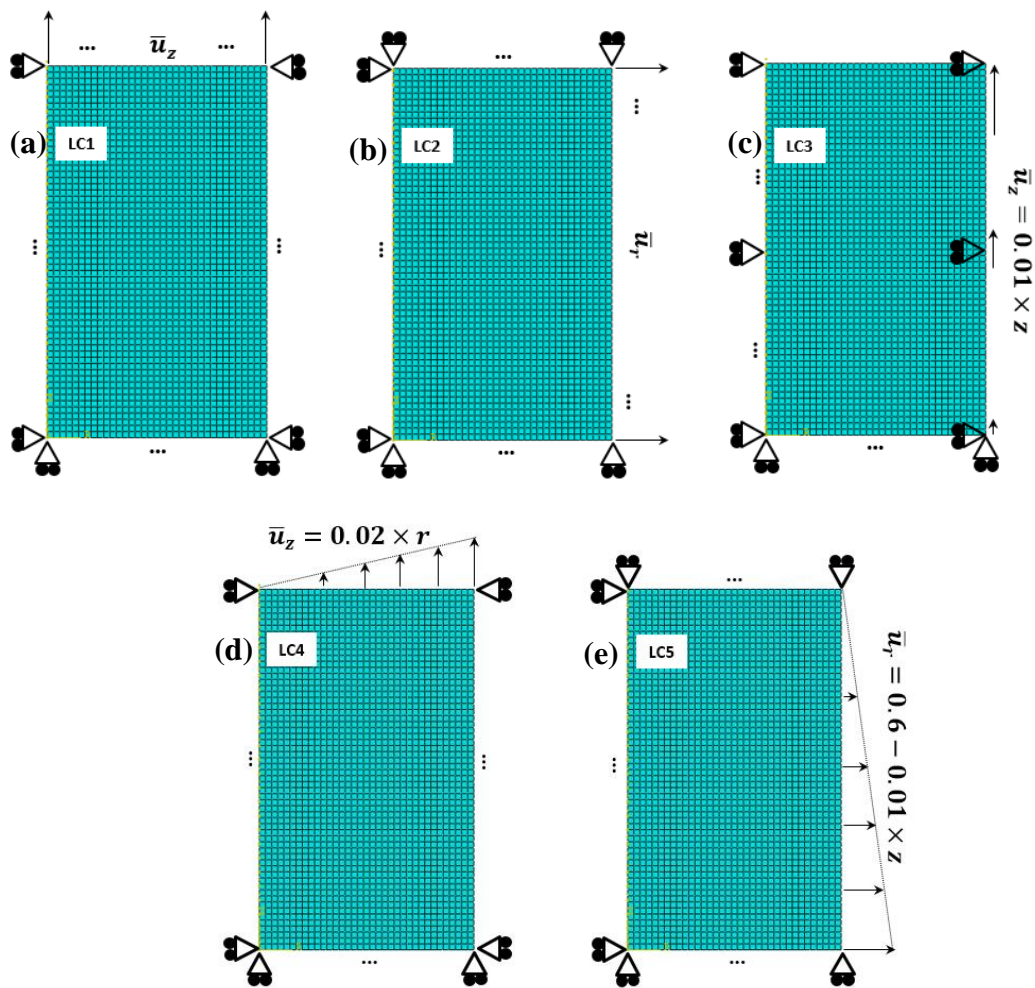
Figure 6.14 – Homogeneous and inhomogeneous load cases used for the determination of the elastic constants (a) Load case 1, (b) Load case 2, (c) Load case 3, (d) Load case 4, (e) Load case 5.

115

Then, the strain energy equivalence between two models is written in the form of an optimization problem in terms of remaining unknown elastic constants. The optimization problem is then solved by using Matlab Genetic Algorithm (GA) toolbox (Matlab, 2018). C_{33} is already calculated by using the Load Cases 1, and a relation between C_{11} and C_{12} is found by using the Load Case 2. Therefore, C_{11}, C_{13} and C_{44} are considered as remaining unknown variables for the optimization problem. The constant C_{33} is expected to be higher than the above elastic constants, because it is related with the fiber direction. Therefore, for the upper bound of all remaining constants $C_{33} = 6837.56$ MPa is given. Furthermore, as a lower bound for C_{13} and C_{44}, 0 MPa is set. As required by Eqn. (6.1), $C_{11} - C_{12}$ must be positive. Therefore, the lower bound of C_{11} is set to be 9154.44/2. The fitness function $y(C_{11}, C_{13}, C_{44})$ for the optimization problem is formulated as:

$$
\begin{aligned}
y(C_{11}&, C_{13}, C_{44})\\
&= |ET\_capped\_LC_3 - ET\_hom\_LC_3|/ET\_capped\_LC_3\\
&+ |ET\_capped\_LC_4 - ET\_hom\_LC_4|/ET\_capped\_LC_4\\
&+ |ET\_capped\_LC_5 - ET\_hom\_LC_5|/ET\_capped\_LC_5
\end{aligned}
\tag{6.2}
$$

where $ET\_capped\_LC_i$ stands for the strain energy of the capped model for load case i, and $ET\_hom\_LC_i$ stands for the strain energy of the homogenized material for load case i. For the capped model, calculated strain energies from the nonlocal model for the above five load cases are given in Table 6.3.

Table 6.3 – Energy values of the capped model from nonlocal model for the considered load cases

	LC1	LC2	LC3	LC4	LC5
ET [$J \times 10^{-9}$]	80756.73	216241.78	3.9050.52	58502.05	197307.49

By by using Matlab Genetic Algorithm (GA) toolbox elastic constants are determined. The considered GA parameters can be found in the APPENDIX A. The elastic constants computed from the load cases 1 and 2, and by the GA algorithm are given in Table 6.4.

116

Table 6.4 – *Homogenized material elastic constants*

C_{11} [MPa]	C_{12} [MPa]	C_{13} [MPa]	C_{33} [MPa]	C_{44} [MPa]
5070.67	4083.77	2699.80	6837.56	911.07

6.2.3. Statistical Orientation of Fibres

In Gasser et al. (2006), for the hyperelastic modelling of anisotropic arterial layers, authors considered collagen fiber orientations in different directions. They used a Gaussian like distribution function to model the orientation of the collagen fibers. The same modeling approach is also considered here for the orientation of effective fibers developed in the previous section.

The effective fibers are considered to be oriented around a main direction which is $\mathbf{E}_3$ in our case. Figure 6.15 shows the required definitions for the problem formulation, where $\mathbf{E}_3(= \boldsymbol{a})$ shows the main fiber direction, $\boldsymbol{m}$ is the orientation of an arbitrary fiber, θ is the zenith angle, i.e., the angle between X_3 axis and $\boldsymbol{m}$, and ϕ is the azimuth angle, i.e., the angle between X_1 axis and the projection of $\boldsymbol{m}$ onto $X_1 - X_2$ plane. The fiber orientation, **m,** is given as:

$$\boldsymbol{m}(\theta, \phi) = sin\theta cos\phi \boldsymbol{E}_1 + sin\theta sin\phi \boldsymbol{E}_2 + cos\theta \boldsymbol{E}_3 \tag{6.3}$$

A π periodic distribution function, $\rho(\theta, \phi)$, is considered in 3D space (Gasser et al. 2006)

$$\rho(\boldsymbol{m}(\Theta, \phi)) = \frac{1}{\pi}\sqrt{\frac{b}{2\pi}}\frac{exp[b(cos(2(\Theta - \alpha)) + 1)]}{erfi(\sqrt{2b})} \tag{6.4}$$

where, b is the concentration parameter, $erfi$ is the imaginary error function and α is the deviation of the main direction from $\mathbf{E}_3$ which is taken as zero in this study. A transversely isotropic effective fiber distribution is considered, therefore, ρ is independent of ϕ. Note that when $\rho(\theta, \phi)$ is integrated over a unit sphere, the result must be unity:

$$\int_\Omega \rho(\boldsymbol{m}(\Theta,\phi))d\Omega = \int_0^\pi \int_0^{2\pi} \rho(\boldsymbol{m}(\Theta,\phi))sin(\theta)d\theta d\phi = 1 \qquad (6.5)$$

The effect of b on fiber distribution is shown in Figure 6.16. As seen from the figure, $b = 0$ represents a uniform fiber distribution. As b increases, fibers are concentrated about the main fiber direction and $b >> 1$ represents that all the fibers are perfectly aligned in the main direction. It can also be seen from the figure that ρ is π-periodic.
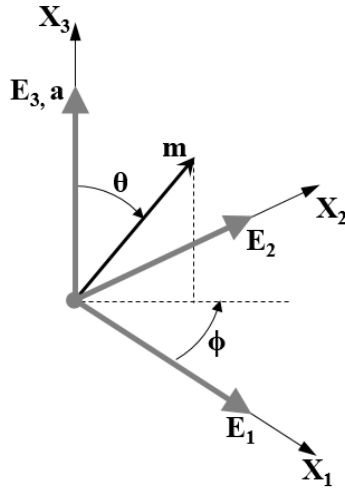
Figure 6.15 *– Fiber orientation vector **m** about the main direction **E**₃=**a***
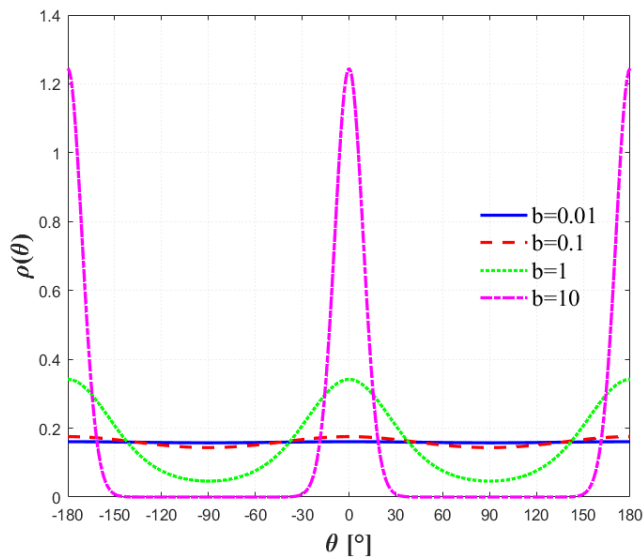
Figure 6.16 *– Effect of fiber concentration parameter b on the distribution function ρ*

118

6.2.4. Composite material

In this section, a composite material is considered with statistically oriented fibers in matrix material, and the calculation of the homogenized properties of the composite is provided. It is further assumed that each phase is subjected to the same macroscopic deformation. In other words, the deformation is assumed to be affine. A prescribed macroscopic strain $\bar{\boldsymbol{\varepsilon}}$ is applied on the transversely isotropic composite material. The applied strain is then transformed into the local fiber coordinate system as

$$\boldsymbol{\varepsilon}_{fm} = \boldsymbol{T}(\theta, \phi) \, \bar{\boldsymbol{\varepsilon}} \, \boldsymbol{T}^T(\theta, \phi) \tag{6.6}$$

where $\boldsymbol{\varepsilon}_{fm}$ is the strain tensor of an individual fiber in the local coordinate system, T is the transpose of a matrix and $\boldsymbol{T}$ is the transformation matrix which is given as

$$\boldsymbol{T}(\theta, \phi) = \boldsymbol{R}_{\boldsymbol{y}}(\theta)\boldsymbol{R}_{\boldsymbol{z}}(\phi) \tag{6.7}$$

$$\boldsymbol{R}_{\boldsymbol{y}}(\theta) = \begin{bmatrix} cos\theta & 0 & sin\theta \\ 0 & 1 & 0 \\ -sin\theta & 0 & cos\theta \end{bmatrix} \tag{6.8}$$

$$\boldsymbol{R}_{\boldsymbol{z}}(\phi) = \begin{bmatrix} cos\phi & -sin\phi & 0 \\ sin\phi & cos\phi & 0 \\ 0 & 0 & 1 \end{bmatrix} \tag{6.9}$$

where $\boldsymbol{R}_{\boldsymbol{y}}(\theta)$ and $\boldsymbol{R}_{\boldsymbol{z}}(\phi)$ are the rotation matrices about $\boldsymbol{E}_2$ and $\boldsymbol{E}_3$, respectively. Figure 6.17 shows a representation of rotation matrices. Then the stress tensor of the fibers in local coordinate system is calculated as

$$\boldsymbol{\sigma}_{fm} = \mathbb{C} : \boldsymbol{\varepsilon}_{fm} \tag{6.10}$$

where $\boldsymbol{\sigma}_{fm}$ is the stress tensor of an individual fiber in local coordinate system, $\mathbb{C}$ is the elasticity tensor of the homogenized fiber with elastic constants in Table 6.4. The stress tensor of the fiber is then transformed back into the global coordinate system

$$\boldsymbol{\sigma}_{fa} = \boldsymbol{T}^T(\theta, \phi) \, \boldsymbol{\sigma}_{fm} \, \boldsymbol{T}(\theta, \phi) \tag{6.11}$$

where $\boldsymbol{\sigma}_{fa}$ is the stress tensor of an individual fiber in global coordinate system. The total stress of the fiber portion of the composite material is obtained with an integral over the orientation space

$$\boldsymbol{\sigma}_f = \iint_{\Omega} \rho(\theta,\phi)\boldsymbol{\sigma}_{fa}d\Omega = \int_0^{\pi} \int_0^{2\pi} \rho(\theta,\phi)\,\boldsymbol{\sigma}_{fa}\,\sin\theta d\phi d\theta \qquad (6.12)$$

where $\boldsymbol{\sigma}_f$ is the total stress tensor of the fibers in global coordinate system. The above integral is evaluated by 21 or 37 points numerical integration schemes. The details of the integration scheme can be found in Bazant and Oh (1986) and Miehe et al. (2004). For the polymer matrix, an isotropic linear elastic law is assumed

$$\boldsymbol{\sigma}_p = \mathbb{C}_p : \bar{\boldsymbol{\varepsilon}} \qquad (6.13)$$

where $\boldsymbol{\sigma}_p$ and $\mathbb{C}_p$ are the stress and the modulus tensors of the polymer matrix material, respectively. The total stress response of the composite material is obtained according to the considered volume fractions

$$\bar{\boldsymbol{\sigma}} = \boldsymbol{\sigma}_f V_f + \boldsymbol{\sigma}_p V_p \qquad (6.14)$$

In above equation $\bar{\boldsymbol{\sigma}}$ is the macroscopic stress of the composite, V_f is the volume fraction of the distributed effective fibers, V_p is the volume fraction of the polymer matrix. It is clear that, $V_f + V_p = 1$ has to hold.
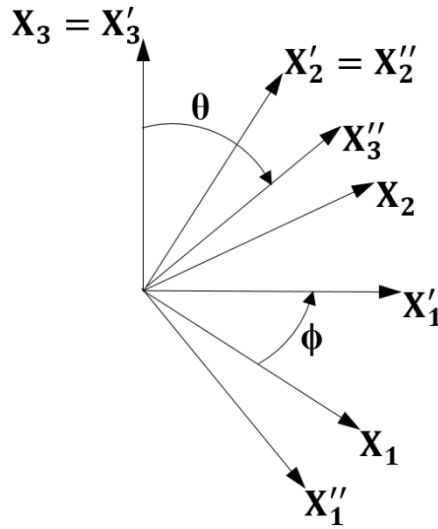
$$(X_1, X_2, X_3) \rightarrow (X_1', X_2', X_3') \rightarrow (X_1'', X_2'', X_3'')$$

Figure 6.17 – Representation of $T(\theta,\phi)=R_y(\theta)R_z(\phi)$

6.2.5. Numerical Example

In this section, the statistical orientation of the effective fibers (Table 6.4) in the matrix (Table 6.1) is considered as shown in the previous sections. The fibers are assumed to be oriented as in Figure 6.15. A simple tension test is simulated by prescribing a macroscopic strain of 0.01 in z direction, while other directions are assumed to be free. Iterations are carried out to make the total composite stress in transverse directions to be zero.

The effects of the orientation parameter b and volumetric fraction of CNT, V_f, are investigated in a parametric study. Three values of b (0, 2 and 4) and two values of V_f (%0.5 and %1) are considered. The results are given in Table 6.5. It can be seen that as b increases, the stress of the fibers in the tensile loading direction σ_{fzz} increases which results in an increase in the macroscopic stress $\bar{\sigma}$ of the composite. The modulus of the composite in the loading direction also increases. The stress of the matrix, σ_{pzz}, more or less remains the same for different values of b. An increase in V_{CNT} also increases the total stress response of the composite except for $b = 0$ case. It can also be clearly seen that the overall Poisson's ratio ν of the composite material decreases with increasing b which means that the material behaves stiffer in the longitudinal direction. The results for higher b values are also obtained, but it is seen that the numerical integration scheme fails to capture the stress response. This is caused by the concentration of the fibers in the mean direction for which the integration scheme fails to resolve. So far the above results are explained with 21 integration scheme. For higher b values, more accurate results can be found by using 37 points integration scheme.

An important point to mention is that for composite material with isotropic fiber orientation, $b = 0$, $E_T = 2828$ MPa is lower than the modulus of the pure matrix, 3040 MPa. This is caused by the lower values of the elastic constants, C_{11} and C_{44} of the effective fiber, which means that the stiffness in radial direction and shear modulus in transverse plane has lower values compared to the pure matrix ($C_{11} = 5109$ MPa and $C_{44} = 2235$ MPa for the isotropic pure matrix), since the actual fiber geometry is a hollow structure. Choi et al. (2016) observed the same situation also for SWNT/epoxy nanocomposite. In order to demonstrate this, C_{44} is increased

gradually while keeping the other elastic parameters constant, Table 6.6. It is seen that after $C_{44} = 2500$ MPa, the effective fiber shows stiffer behavior than the matrix. Additionally, by keeping the other elastic parameters constant and considering the relation $C_{12} = 9154.44 - C_{11}$, C_{11} is increased gradually, Table 6.7. It is seen that composite becomes stiffer after elastic constants in transverse directions, $C_{11} = C_{22}$ become greater than 6000 MPa.

Table 6.5 – *Tensile loading results of a nanocomposite with statistically oriented fibers in a polymer matrix*

b	V_f	V_{CNT}	ν	E_T [MPa]	$\bar{\sigma}$ [MPa]	σ_{fzz} [MPa]	σ_{pzz} [MPa]
0	%26	%0.5	0.3732	2828.47	28.28	24.42	29.64
	%51	%1.0	0.3854	2620.44	26.20	23.58	28.94
2	%26	%0.5	0.3623	3128.09	31.28	34.16	30.27
	%51	%1.0	0.3644	3212.69	32.13	34.03	30.15
4	%26	%0.5	0.3494	3538.88	35.39	47.85	31.01
	%51	%1.0	0.3403	4015.43	40.15	48.44	31.53

(21 integration points)

Table 6.6 – *Effect of increase in C_{44} on the tensile loading results of a nanocomposite with statistically oriented fibers in a polymer matrix*

C_{44} [MPa]	b	V_f	V_{CNT}	ν	E_T [MPa]	$\bar{\sigma}$ [MPa]	σ_{fzz} [MPa]	σ_{pzz} [MPa]
1500				0.3697	2905.61	29.06	26.82	29.84
2000	0	%26	%0.5	0.3668	2970.46	29.70	28.84	30.01
2500				0.3639	3035.10	30.35	30.85	30.18

Table 6.7 *– Effect of increase in C_{11} tensile loading results of a nanocomposite with statistically oriented fibers in a polymer matrix*

C_{11} [MPa]	C_{12} [MPa]	$C_{11} - C_{12}$ [MPa]	b	V_f	V_{CNT}	ν	E_T [MPa]	$\bar{\sigma}$ [MPa]	σ_{fzz} [MPa]	σ_{pzz} [MPa]
5500	3654.44	1845.56	0	%26	%0.5	0.3681	2940.19	29.40	27.90	29.93
6000	3154.44	2845.56				0.3624	3069.41	30.69	31.92	30.26
6500	2654.44	3845.56				0.3566	3197.83	31.98	35.91	30.60

CHAPTER 7

SUMMARY, CONCLUSION AND FUTURE WORK

In Chapter 2, nanocomposite properties are explained in detail based on a particular polymer nanocomposite couple; CNT and PEEK. Individual properties of the CNT and the PEEK, the interface properties of CNT/PEEK, the manufacturing processes, the characterization techniques, and the mechanical properties are investigated in a comparison study among some selected works from literature. It is seen that CNTs have different properties in terms of purity, density, diameter, length, number of walls etc. Similarly, PEEK polymers have different specifications in terms of molecular weight, density, glass transition temperature, melting temperature, viscosity etc. In some of the references, various methods (chemical etching, grafting by in-situ polymerization, wrapping and oxidization) are used for the functionalization on the CNTs. Various manufacturing methods with different temperature and pressure levels, process time are used in literature for the production of polymer nanocomposites. Not only the conventional methods (strain gage, extensometer) but also more modern methods (Raman Spectroscopy, Transmission Electron Microscopy, Scanning Electron Microscopy, Fourier Transform-Infra Red) are used for the characterization of nanocomposites. At the end of the chapter, the mechanical properties of the CNT/PEEK nanocomposite are investigated. Although, the mechanical properties of the polymer are generally enhanced with the addition of CNT, the level of improvement significantly varies among the references.

In Chapter 3, the Eringen's nonlocal elasticity and the Aifantis's gradient elasticity frameworks are explained which are used for the incorporation of the size effect in the elasticity theory. The details of two formulations, some analytical solutions, different forms, variational and FEM formulations are provided. The relations of the gradient model to the nonlocal model and to the higher order gradient models are discussed.

In Chapter 4, a new gradient elasticity model, E-grad model, for inhomogeneous

elastic rod is proposed. The proposed model is based on the introduction of the gradient enhanced Young's modulus with a differential equation. In the proposed model, in addition to the differential equation of the modulus, the classical equilibrium equation is solved. Both analytical and FE formulations of the proposed model are provided. For a 3-phase one-dimensional model problem, the analytical and finite element results are compared with the Aifantis's gradient elasticity formulation. Compared to Aifantis's formulation, it is seen that the internal characteristic length has a significantly more pronounced influence on the results of the proposed model.

In Chapter 5, the E-grad model is extended to multi-dimensional framework. The FE formulation is provided for axisymmetric problems. A soft cylindrical rod with a stiff spherical inclusion is considered as a model problem. The model provides a smooth and continuous variation of E and G fields over the entire domain. It is shown that, as expected, the macroscopic stiffness of the composite increases with increasing internal length scale parameter. The response of the model is compared with the numerical and experimental results of a polyimide/silica nanocomposite. It is seen that the proposed model predicts the experimentally measured macroscopic modulus of nanocomposite well. Finally, the spherical inclusion problem is simulated by choosing different length scale parameters in different directions, and it is shown that the behavior of the nanocomposite with isotropic constituents becomes anisotropic, if the length scale parameters are chosen differently.

In Chapter 6, by using the E-grad model and genetic algorithm optimization, an effective fiber model is generated to obtain the homogenized modulus of a CNT reinforced polymer. The effective fiber model is then utilized in a fiber reinforced polymer which takes the statistical distribution of the fibers into account. It is seen that for the zero value of the concentration parameter the nanocomposite is isotropic, while the increase in the concentration parameter leads to a transversely isotropic nanocomposite material.

The key observations and the future works of the study are summarized below:

- In Chapter 2, it was shown that the differences between the material properties of the CNT/PEEK nanocomposites in literature are due to the different material properties of the constituents, functionalization of CNTs, interface and interphase properties, manufacturing methods and characterization techniques. Therefore, numerical models have to be material specific for reliable results. In future, for industrial applications, a standard procedure has to be developed for composite manufacturing.

- In Chapter 3, it was shown that, the nonlocal and the gradient elasticity models have more complex variational and FE formulations, even for the simplest Eringen's nonlocal elasticity and Aifantis's gradient elasticity models. These models also require higher order stress fields, strain fields and boundary conditions which are not very intuitive.

- In Chapter 4, a novel gradient elasticity model, E-grad model, was proposed. The proposed model has simple variational and FE formulations. It also does not require any additional higher order stress fields, strain fields and boundary conditions. It eliminates sharp changes/singularities in the material property distribution, and in displacement, strain and stress fields. In future, the proposed formulation can also be used to remove any type of singularities in different kind of problems. However, the model requires an inhomogeneous material to start with, i.e., nonlocal effects disappear if the material is homogeneous.

- In Chapter 5, the E-grad model was extended to general multi-dimensional framework. In a comparison with a problem from literature, it was shown that the E-grad model gives reasonable results. A functionally graded interface with nonlocal effects can be created with the proposed model. It was also shown that the model can create an anisotropic material by using different internal length scales in different directions. In future, the functionally graded interface with anisotropic behavior can be further studied for other materials, i.e., phase changing materials, evolution of material properties in time.

- In Chapter 6, from a literature survey, it was seen that for non-functionalized CNTs, the interface between the CNT and polymer is weak and is not effective in load transfer. Furthermore, an interphase is developed in the polymer near to

CNT surface with elastic properties stronger than the polymer. In some studies, this interphase region is taken as the main reinforcing mechanism in nanocomposites. By neglecting the CNT in numerical models of the nanocomposites, it is found that although a reinforcement is obtained in axial direction, weaker material properties are obtained in transverse and shear directions. The full details of the interaction between the CNT and the polymer are difficult to model in continuum scale. Therefore, in future, more atomistic and sub-atomistic simulations, i.e., MD, DFT, coarse grain, have to be used for a better understanding of the load transfer mechanisms between the CNT and the polymer. Especially, better understanding of the interface and the interphase regions requires deeper investigation.

REFERENCES

[1]. Abali, B.E., Müller, W.H., Eremeyev, V.A. 2015. "Strain Gradient Elasticity with Geometric Nonlinearities and its Computational Evaluation", Mechanics of Advanced Materials and Modern Processes, 1:4

[2]. Abaqus/CAE V2016, Dassault Systemes

[3]. Abbate, M., Musto, P., Ragosta, G., Scarinzi, G., Mascia, L. 2004. "Polyimide-silica hybrids: spectroscopy, morphology and mechanical properties", Macromol. Symp. 218, 211–220.

[4]. Abdollahi, R., Boroomand, B. 2013. "Benchmarks in Nonlocal Elasticity Defined by Eringen's Integral Model", International Journal of Solids and Structures, 50, 2758–2771

[5]. Aifantis, E.C. 1984. "On The Microstructural Origin of Certain Inelastic Models', Trans. ASME J. Engng. Mater. Tech., 106, 326-330

[6]. Aifantis, E., 1992. "On The Role of Gradients in the Localization of Deformation and Fracture". Int. J. Eng. Sci. 30, 1279–1299

[7]. Aifantis, E.C. 1999. "Strain Gradient Interpretation of Size Effects", International Journal of Fracture, 95, 299–314

[8]. Aifantis, E.C. 2011. "On the gradient approach - Relation to Eringen's Nonlocal Theory", International Journal of Engineering Science, 49, 1367–1377

[9]. Akgöz, B., Civalek, Ö. 2016. "Bending Analysis of Embedded Carbon Nanotubes Resting on an Elastic Foundation Using Strain Gradient Theory", Acta Astronautica, 119, 1–12

[10]. Altan, S.B., Aifantis, E.C. 1992. "On the Structure of the Mode-III Crack-Tip in Gradient Elasticity", Scripta Met., 26, 319-324

[11]. Altan, B. S., Aifantis, E. C. 1997. "On Some Aspects in the Special Theory of Gradient Elasticity", Journal of the Mechanical Behavior of Materials, 8, 231-282.

[12]. Arash, B., Park, H.S., Rabczuk, T. 2015. "Mechanical properties of carbon nanotube reinforced polymer nanocomposites: A coarse-grained model", Composites Part B, 80, 92-100

[13]. Arash, B., Wang, Q. 2012. "A Review On the Application of Nonlocal Elastic Models in Modeling of Carbon Nanotubes and Graphenes", Computational Materials Science 51, 303–313

[14]. Ashrafi, B., Díez-Pascual, A.M., Johnson, L., Genest, M., Hind, S., Martinez-Rubi, Y., González-Domínguez, Jose M., Martínez, M. T., Simard, B., Gómez-Fatou, M.A., Johnston, A. 2012. "Processing and properties of PEEK/glass fiber laminates: Effect of addition of single-walled carbon nanotubes". Composites: Part A, 43, 1267–1279

[15]. Askes, H., Aifantis, E.C. 2011. "Gradient Elasticity in Statics and Dynamics: An Overview of Formulations, Length Scale Identification Procedures, Finite Element Implementations and New Results" International Journal of Solids and Structures, 48, 1962–1990

[16]. Askes, H., Gitman, I.M. 2010. "Review and Critique of the Stress Gradient Elasticity Theories of Eringen and Aifantis" G.A. Maugin, A.V. Metrikine (eds.), Mechanics of Generalized Continua, Advances in Mechanics and Mathematics 21, Springer

[17]. Askes, H., Gutiérrez, M.A. 2006. "Implicit Gradient Elasticity", International Journal for Numerical Methods in Engineering, 67, 400–416

[18]. Askes, H., Suiker, A.S.J., Sluys, L.J. 2002. "A Classification of Higher-Order Strain-Gradient Models – Linear Analysis", Archive of Applied Mechanics, 72, 171–188

[19]. Askes, H., Morata, I. Aifantis, E.C. 2008. "Finite Element Analysis with Staggered Gradient Elasticity", Computers and Structures, 86, 1266–1279

[20]. Ateshian, G.A., Rajan, V., Chahine, N.O., Canal, C.E., Hung, C.T. 2009. "Modeling the Matrix of Articular Cartilage Using a Continuous Fiber Angular Distribution Predicts Many Observed Phenomena", Journal of Biomechanical Engineering, 2009, 31, 061003

[21]. Auffray, N. 2013. "Geometrical Picture of Third-Order Tensors", H. Altenbach et al. (eds.), Generalized Continua as Models for Materials, Springer-Verlag

[22]. Auffray, N., Le Quang, H., He, Q.C. 2013. "Matrix Representations for 3d Strain-Gradient Elasticity", arXiv:1301.1890 [math-ph]

[23]. Bai, J.B., Allaoui, A. 2003. "Effect of the length and the aggregate size of MWNTs on the improvement efficiency of the mechanical and electrical properties of nanocomposites—experimental investigation", Composites: Part A, 34,689–694

[24]. Bakshi, S.R., Musaramthota, V., Virzi, D.A., Keshri, A.K., Lahiri, D., Singh, V., Seal, S., Agarwal, A. 2011. "Spark plasma sintered tantalum carbide–carbon nanotube composite: Effect of pressure, carbon nanotube length and dispersion technique on microstructure and mechanical properties", Materials Science and Engineering A, 528, 2538–2547

[25]. Bazant, Z.P., Oh, B.H., 1986. "Efficient numerical integration on the surface of a sphere". Z. Anegw. Math. Mech. 66, 37–49

[26]. Benvenuti, E., Simone, A. 2013. "One-Dimensional Nonlocal and Gradient Elasticity: Closed-Form Solution and Size Effect", Mechanics Research Communications, 48, 46–51

[27]. Beskou, S.P., Beskos, D. 2010. "Static Analysis of Gradient Elastic Bars, Beams, Plates and Shells", The Open Mechanics Journal, 4, 65-73

[28]. Boyer, F., Olivier, P.A., Pons, F., Cadaux, P.H. 2012. "Mechanical and electrical behavior of a Peek/Carbon nanotube composite". ECCM15 – 15th European Conference On Composite Materials, Venice, Italy

[29]. Brydson, J. 1999. "Plastics Materials", 7th ed. Wobum, MA: Butterworth-Heinemann

[30]. Callister, W.D. 2003. "Materials science and engineering: an introduction". New York: Wiley

[31]. Choi, J., Shin, H., Cho, M. 2016. "A multiscale mechanical model for the effective interphase of SWNT/epoxy nanocomposite", Polymer, 89, 159-171

[32]. Coleman, J.N., Cadek, M., Ryan, K.P., Fonseca, A., Nagy, J.B., Blau, W.J., Ferreira, M.S. 2006. "Reinforcement of polymers with carbon nanotubes. The role of an ordered polymer interfacial region. Experiment and modeling", Polymer, 47, 8556-8561

[33]. Cortes, D.H., Elliott, D.M. 2014. "Accurate Prediction of Stress in Fibers with Distributed Orientations Using Generalized High-Order Structure Tensors", Mechanics of Materials, 75, 73–83

[34]. Cosserat, E., Cosserat, F. 1909. "Theorie des Corps Deformables", Hermann et Fils, Paris

[35]. Davoudi, K.M., Gutkin, M.Y., Shodja, H.M. 2009. "Analysis of Stress Field of a Screw Dislocation Inside an Embedded Nanowire Using Strain Gradient Elasticity", Scripta Materialia, 61, 355–358

[36]. Dell'Isola, F., Sciarra, G., Vidoli, S. 2010. "Generalized Hooke's Law for Isotropic Second Gradient Materials", Proc. R. Soc A: Math. Phys. Eng. Sci., 465, 2177–2196

[37]. Dresselhaus, M.S., Dresselhaus, G., Saito, R. 1995. "Physics Of Carbon Nanotubes" Carbon, Vol. 33, No. 7, 883-891

[38]. Driemeier, L., Comi, C., Proenç, S.P.B., 2005. "On Nonlocal Regularization in One Dimensional Finite Strain Elasticity and Plasticity", Computational Mechanics, 36, 34–44

[39]. Eringen, A.C. 1983. "On Differential Equations of Nonlocal Elasticity and Solutions of Screw Dislocation and Surface Waves". J. Appl. Phys., 54, 4703–4710

[40]. Eringen, A.C. 2002. "Nonlocal Continuum Field Theories", Springer-Verlag New York

[41]. Ferretti, M., Madeo, A., dell'Isola, F., Boisse, P. 2014. "Modeling the Onset of Shear Boundary Layers in Fibrous Composite Reinforcements by Second-Gradient Theory", Z. Angew. Math. Phys. 65, 587–612

[42]. Forest, S. 1999. "Homogenization Methods and the Mechanics of Generalized Continua", Geometry, Continua and Microstructure, edited by G. Maugin, Travaux en Cours No. 60, Hermann, Paris, France, 35-48

[43]. Fuschi, P., Pisano, A.A., De Domenico, D. 2015. "Plane Stress Problems in Nonlocal Elasticity: Finite Element Solutions with a Strain-Difference-Based Formulation", J. Math. Anal. Appl., 431, 714–736

[44]. Gao, X.L., Park, S.K. 2007. "Variational Formulation of a Simplified Strain Gradient Elasticity Theory and its Application to a Pressurized Thick-Walled Cylinder Problem", International Journal of Solids and Structures, 44, 7486–7499

[45]. Gasser, T.C., Ogden, R.W., G.A. Holzapfel. 2006. "Hyperelastic Modelling of Arterial Layers with Distributed Collagen Fiber Orientations", Journal of the Royal Society Interface, 3, 15–35

[46]. Girard, M.J.A., Downs, J.C., Burgoyne, C.F., Suh, J.K.F. 2009. "Peripapillary and Posterior Scleral Mechanics—Part I: Development of an Anisotropic Hyperelastic Constitutive Model", Journal of Biomechanical Engineering, 131, 051011-1-9

[47]. Gitman, I.M., Askes, H., Kuhl, E., Aifantis, E.C. 2010. "Stress Concentrations in Fractured Compact Bone Simulated with a Special Class of Anisotropic Gradient Elasticity", International Journal of Solids and Structures, 47, 1099–1107

[48]. Grady, B.P. 2011. "Carbon Nanotube-Polymer Composites, Manufacture, Properties, and Applications", Wiley

[49]. Guehenec, M., Tishkova, V., Dagreou, S. Leonardi, F., Derail, C., Puech, P., Pons, F., Gauthier, B., Cadaux, P.H., Bacsa, W. 2013. "The effect of twin screw extrusion on structural, electrical, and rheological properties in carbon nanotube poly-ether-ether-ketone nanocomposites". J. Appl. Polym. Sci., 2527-2535

[50]. Gusev, A.A., Lurie, S.A. 2017. "Symmetry Conditions in Strain Gradient Elasticity", Mathematics and Mechanics of Solids, 22(4), 683–691

[51]. Gülaşık, H., Göktepe, S., Gürses, E. 2018a. "A Modulus Gradient Model for an Axially Loaded Inhomogeneous Elastic Rod", Meccanica, 53, (2018), 2573–2584

[52]. (submitted) Gülaşık, H., Göktepe, S., Gürses, E. 2018b. "A Modulus Gradient Model for Inhomogeneous Materials with Isotropic Linear Elastic Constituents"

[53]. Holzapfel, G.A., Ogden, R.W. 2015. "On the Tension-compression Switch in Soft Fibrous Solids", European Journal of Mechanics A/Solids, 49, 561-569

[54]. Hwang, Y., Kim, M., Kim, J. 2013. "Improvement of the mechanical properties and thermal conductivity of poly(ether-ether-ketone) with the addition of graphene oxide-carbon nanotube hybrid fillers". Composites: Part A, 55, 195–202

[55]. Innovativecomposite, "what-is-carbon-fiber", 2018. http://www. innovativecomposite. com /what-is-carbon-fiber/, retrieved 16.04.2016

[56]. Jain, R., Choi, Y. H., Yaodong, L., Minus, M. L., Chae, H. G., Kumar, S., Baek, J. 2010. "Processing, structure and properties of poly (ether ketone) grafted few wall carbon nanotube composite fibers". Polymer, 51, 3940-3947

[57]. Jensen, B.D., Wise, K.E., Odegard, G.M. 2016. "Simulation of mechanical performance limits and failure of carbon nanotube composites", Modelling Simul. Mater. Sci. Eng., 24, 025012 (23pp)

[58]. Karatrantos, A., Clarke, N., Kröger, M. 2016. "Modeling of Polymer Structure and Conformations in Polymer Nanocomposites from Atomistic to Mesoscale: A Review", Polymer Reviews, 56:3, 385-428

[59]. Lam, D.C.C., Yang, F., Chong, A.C.M., Wang, J., Tong, P. 2003. "Experiments and Theory in Strain Gradient Elasticity", Journal of the Mechanics and Physics of Solids, 51, 1477–1508

[60]. Latorre, M., Montans, F.J. 2016. "On the Tension-Compression Switch of the Gasser–Ogden–Holzapfel Model: Analysis and a New Pre-Integrated Proposal", Journal of the Mechanical Behavior of Biomedical Materials, 57, 175 – 189

[61]. Lazar, M. 2016. "Irreducible Decomposition of Strain Gradient Tensor in Isotropic Strain Gradient Elasticity", ArXiv: 1604 [physics.class-ph]

[62]. Li, J., Zhang, L.Q. 2011. "Reinforcing effect of carbon nanotubes on PEEK composite filled with carbon fiber". Materials Science and Technology, 27, 252-256

[63]. Liu, C.H., Liu, Y.Y., Zhang, Y.H., Wei, R.R., Zhang. H.L. 2009. "Tandem extraction strategy for separation of metallic and semiconducting SWCNTs using condensed benzenoid molecules: effects of molecular morphology and solvent", Physical Chemistry Chemical Physics, 2009, 11, 7257–7267

[64]. Madani, S.Y., Mandel, A. Seifalian, A.M. 2013. "A concise review of carbon nanotube's toxicology", Nano Rev., 2013, 4

[65]. Malagu, M., Benvenuti, E., Duarte, C.A., Simone, A. 2014. "One-Dimensional Nonlocal and Gradient Elasticity: Assessment of High Order Approximation Schemes", Comput. Methods Appl. Mech. Engrg., 275, 138–158

[66]. Malagù, M., Benvenuti, E., Simone, A. 2015. "One-Dimensional Nonlocal Elasticity for Tensile Single-Walled Carbon Nanotubes: A Molecular Structural Mechanics Characterization", European Journal of Mechanics A/Solids, 54, 160-170

[67]. Malagù, M., Goudarzi, M., Lyulin, A., Benvenuti, E., Simone, A. 2017. "Diameter-dependent elastic properties of carbon nanotube-polymer composites: Emergence of size effects from atomistic-scale simulations", Composites Part B, 131, 260-281

[68]. Matlab, "Genetic Algorithm Options", 2018. https://www.mathworks.com/help/gads/genetic-algorithm-options.html, retrieved 18.07.2018

[69]. Miehe, C., Goktepe, S., Lulei, F. 2004. "A micro-macro approach to rubber-like materials—Part I: the non-affine micro-sphere model of rubber elasticity", Journal of the Mechanics and Physics of Solids, 52, 2617–2660

[70]. Mindlin, R.D. 1964. "Micro-Structure in Linear Elasticity", Arch. Rational Mech. Anal., 16, 51-78

[71]. Mohiuddin, M., Hoa, S.V. 2011. "Temperature dependent electrical conductivity of CNT–PEEK composites". Composites Science and Technology, 72, 21–27

[72]. Murmu, T., Pradhan, S.C. 2009. "Thermo-Mechanical Vibration of a Single-Walled Carbon Nanotube Embedded In An Elastic Medium Based On Nonlocal Elasticity Theory", Computational Materials Science, 46, 854-859

[73]. Odegard, G.M, Gates, T.S., Wise, K.E., Park, C., Siochi, E.J. 2003. "Constitutive modeling of nanotube–reinforced polymer composites", Composites Science and Technology, 63, 1671–1687

[74]. Ogasawara, T., Tsuda, T., Takeda, N. 2011. "Stress–strain behavior of multi-walled carbon nanotube/PEEK composites". Composites Science and Technology, 71, 73–78

[75]. Pandolfi, A., Holzapfel, G.A. 2008. "Three-Dimensional Modeling and Computational Analysis of the Human Cornea Considering Distributed Collagen Fibril Orientations", Journal of Biomechanical Engineering, 130, 1-12

[76]. Pandolfi, A., Vasta, M. 2012. "Fiber Distributed Hyperelastic Modeling of Biological Tissues", Mechanics of Materials, 44, 151–162

[77]. Papanicolopulos, S.A., Zervos, A., Vardoulakis, I. 2009. "A three-dimensional C1 finite element for gradient elasticity", International Journal for Numerical Methods in Engineering, 77:1396–1415

[78]. Peddieson, J., Buchanan, G.R., McNitt, R.P. 2003. "Application of nonlocal continuum models to nanotechnology", International Journal of Engineering Science, 41, 305–312

[79]. Pisano, A.A., Fuschi, P. 2003. "Closed Form Solution for a Nonlocal Elastic Bar in Tension", International Journal of Solids and Structures, 40, 13–23

[80]. Polizzotto, C. 2001. "Nonlocal Elasticity and Related Variational Principles", International Journal of Solids and Structures, 38, 7359-7380

[81]. Polizzotto, C. 2003. "Unified Thermodynamic Framework for Nonlocal/ Gradient Continuum Theories", European Journal of Mechanics A/Solids, 22, 651–668

[82]. Polizzotto, C. 2003. "Gradient Elasticity and Nonstandard Boundary Conditions", International Journal of Solids and Structures, 40, 7399–7423

[83]. Polizzotto, C. 2016. "A Note on the Higher Order Strain and Stress Tensors Within Deformation Gradient Elasticity Theories: Physical Interpretations and Comparisons", International Journal of Solids and Structures, 90, 116–121

[84]. Polizzotto, C. 2017. "A Hierarchy of Simplified Constitutive Models Within Isotropic Strain Gradient Elasticity", European Journal of Mechanics A/Solids, 61, 92-109

[85]. Polizzotto, C. 2018. "Anisotropy in strain gradient elasticity: Simplified models with different forms of internal length and moduli tensors", European Journal of Mechanics - A/Solids, 71, 51-63

[86]. Polizzotto, C., Fuschi, P., Pisano, A.A. 2004. "A Strain-Difference-Based Nonlocal Elasticity Model", International Journal of Solids and Structures, 41, 2383–2401

[87]. Polizzotto, C., Fuschi, P., Pisano, A.A. 2006. "A Nonhomogeneous Nonlocal Elasticity Model", European Journal of Mechanics A/Solids, 25, 308–333

[88]. Ru, C.Q., Aifantis, E.C. 1993. "A Simple Approach to Solve Boundary-Value Problems in Gradient Elasticity". Acta Mech,101, 59–68

[89]. Rudraraju, S., Van der Ven, A., Garikipati, K. 2014. "Three-Dimensional Isogeometric Solutions to General Boundary Value Problems of Toupin's Gradient Elasticity Theory at Finite Strains", Comput. Methods Appl. Mech. Engrg., 278, 705–728

[90]. Shu, J.Y., King, W.E., Fleck, N.A. 1999. "Finite Elements for Materials with Strain Gradient Effects", Int. J. Numer. Meth. Engng. 44, 373-391

[91]. Sudak, L. J. 2003. "Column buckling of multiwalled carbon nanotubes using nonlocal continuum mechanics", Journal of Applied Physics, 94 (11), 7281-7281

[92]. Suiker, A.S.J., Chang, C.S. 2000. "Application of Higher-Order Tensor Theory for Formulating Enhanced Continuum Models", Acta Mechanica, 142, 223-234

[93]. Tishkova, V., Raynal, P., Puech, P., Lonjon, A., Le Fournier, M., Demont, P., Flahaut, E., Bacsa W. 2011. "Electrical conductivity and Raman imaging of

double wall carbon nanotubes in a polymer matrix". Composites Science and Technology, 71, 1326-1330

[94]. Toupin, R.A. 1962. "Elastic Materials with Couple Stresses', Arch. Rational Mech. Anal., 11, 385-414

[95]. Tserpes, K.I., Papanikos, P., Labeas, G., Pantelakis, Sp.G. 2008. "Multi-scale modeling of tensile behavior of carbon nanotube-reinforced composites", Theoretical and Applied Fracture Mechanics, 49, 51–60

[96]. Tserpes, K.I., Silvestre, N. 2014. "Modeling of Carbon Nanotubes, Graphene and their Composites", Springer International Publishing, Switzerland

[97]. Vidu, R., Rahman, M., Mahmoudi, M., Enachescu, M., Poteca, T.D., Opris, I. 2014. "Nanostructures: a platform for brain repair and augmentation", Frontiers in Systems Neuroscience, 8

[98]. Wang, X. Jiang, Q., Xu, W. Cai, W., Inoue, Y. Zhu, Y. 2013. "Effect of carbon nanotube length on thermal, electrical and mechanical properties of CNT/bismaleimide composites", CARBON 53, 145 – 152

[99]. Wang, Z., Oelkers, R.J., Lee, K.C., Fisher, F.T. 2016. "Annular Coated Inclusion Model and Applications for Polymer Nanocomposites – Part I: Spherical Inclusions", Mechanics of Materials, 101, 170–184

[100]. Wei, C., Srivastava, D., Cho, K. 2004. "Structural Ordering in Nanotube Polymer Composites", Nano Letters, Vol. 4, No. 10

[101]. Wikipedia, "High performance plastics", 2016. https://en.wikipedia.org/wiki/ High_performance_plastics, retrieved 23.06.2016

[102]. Wikipedia, "Polyether ether ketone", 2018. https://en.wikipedia.org/wiki/ Polyether_ether_ketone, retrieved 16.04.2018

[103]. Wernik, J.M., Meguid, S.A. 2011. "Multiscale modeling of the nonlinear response of nano-reinforced polymers", Acta Mech, 217: 1

[104]. Wu, H.C., Chang, X., Liu, L., Zhao, F., Zhao, Y. 2009. "Chemistry of carbon nanotubes in biomedical applications", J. Mater. Chem., 2010, 20, 1036–1052

[105]. Zhang, S., Wang, H., Wang, G., Jiang, Z. 2012. "Material with High Dielectric Constant, Low Dielectric Loss, And Good Mechanical and Thermal Properties Produced Using Multi-Wall Carbon Nanotubes Wrapped with Poly (Ether Sulphone) in a Poly (Ether Ether Ketone) Matrix". Applied Physics Letters, 101

[106]. Zhou, S., Li, A., Wang, B. 2016. "A Reformulation of Constitutive Relations in the Strain Gradient Elasticity Theory for Isotropic Materials" International Journal of Solids and Structures, 80, 28–37

[107]. Zibaei, I., Rahnama, H., Taheri-Behrooz, F., Shokrieh, M.M. 2014. "First Strain Gradient Elasticity Solution for Nanotube-Reinforced Matrix Problem", Composite Structures, 112, 273–282

APPENDICES

APPENDIX A

The details of the MATLAB genetic algorithm used for the homogenization problem in Section 6.2.2 are given below.

Matlab GA Toolbox options:

CreationFcn: @gacreationlinearfeasible

CrossoverFcn: @crossoverintermediate

HybridFcn: @fmincon

MaxGenerations: 50

MutationFcn: @mutationadaptfeasible

PopulationSize: 200

UseParallel: 1

UseVectorized: 0

ConstraintTolerance: 1.0000e-03

CrossoverFraction: 0.8000

EliteCount: '0.05*PopulationSize'

FitnessLimit: -Inf

FitnessScalingFcn: @fitscalingrank

FunctionTolerance: 1.0000e-06

InitialPopulationMatrix: []

InitialPopulationRange: []

InitialScoresMatrix: []

MaxStallGenerations: 50

MaxStallTime: Inf

MaxTime: Inf

NonlinearConstraintAlgorithm: 'auglag'

OutputFcn: []

PopulationType: 'doubleVector'

SelectionFcn: @selectionstochunif

For a constraint problem "*mutationadaptfeasible*", "*gacreationlinearfeasible*", "*crossoverintermediate*" are the recommended mutation, creation and crossover functions, respectively, in Matlab GA toolbox. In order to speed up the computation, parallel computing is used. The population size is increased to 200 from the default value of 50 to better resolve the domain. By using a "*fmincon*" function as a hybrid function, a constraint minimization is applied at the end of each GA run to further optimize the result. The other parameters are kept at default values.

<u>Convergence of GA:</u>

To check the convergence of the GA, fitness value and average distance between variables are plotted at each generation as seen in Figure A.1. Figure A.1(a) shows the mean value of the fitness function which rapidly decreases and stays almost constant after 1st generation. Note that the best fitness value stays always at a low value starting from the first generation. The average distance between variables is another method to check the convergence of a GA problem. Figure A.1(b) shows that distance between the variables starts at a high value. This indicates that the algorithm covers the domain well at the start. After the 15th generation, the distance values remain almost constant which means that the minimization is achieved.

<u>Effect of "fmincon":</u>

Sometimes, a constraint algorithm is used further to increase the accuracy of the GA. As specified in the above paragraphs, Matlab "*fmincon*" function is used as hybrid function in GA to increase the accuracy of the considered problem. From the below Matlab output, it can be seen that the GA algorithm is terminated after reaching the generation limit of 50. Then, *fmincon* algorithm starts. It can be observed that the outputs of both algorithms are almost the same which shows that the GA converged to the possible minimum before "*fmincon*".

C values: C11=5.070919e+03, C12=4.083521e+03, C13=2.699875e+03,
C44=9.120725e+02, C33=6.837560e+03

Optimization terminated: maximum number of generations exceeded.

Switching to the hybrid optimization algorithm (FMINCON).

C values: C11=5.070670e+03, C12=4.083770e+03, C13=2.699802e+03,
C44=9.110730e+02, C33=6.837560e+03

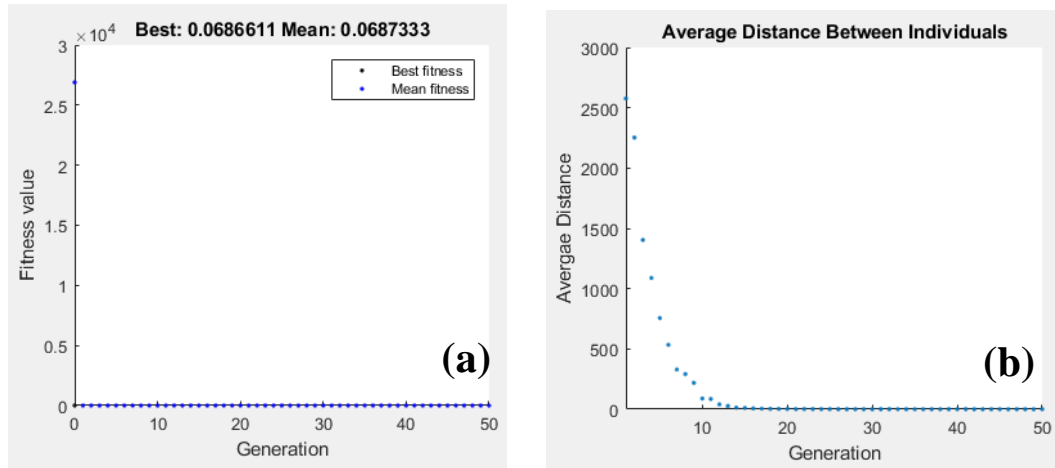*FMINCON terminated.*

***Figure A.1** – Matlab GA outputs; (a) fitness value vs generation, (b) average distance between variables vs generation*

<u>*Effect of population size:*</u>

In GA, the default population size for problems with less than five variables is 50. The results in Table 6.4 are for a population size of 200. The same problem is solved with a higher population size of 300 to better resolve the domain. In Table A.1, it is seen that only C_{11} and C_{12} changes about 3%, while the other parameters remain almost the same if the population size is increased from 200 to 300.

***Table A.1** – Homogenized material elastic constants with 300 population size*

C_{11} [MPa]	C_{12} [MPa]	C_{13} [MPa]	C_{33} [MPa]	C_{44} [MPa]
5209.35	3945.09	2699.71	6837.56	906.44

143

Check load case:

By using the parameters in Table 6.4, another load case, Figure A.2, was also run to check the validity of the elastic constants. The energy outputs from the capped nonlocal model and homogenized local model are compared which are $2.643 \times 10^5 [10^{-9} \text{Joule}]$ and $2.588 \times 10^5 [10^{-9} \text{Joule}]$, respectively. The difference between the energy values is about 2% which is considered to be acceptable.
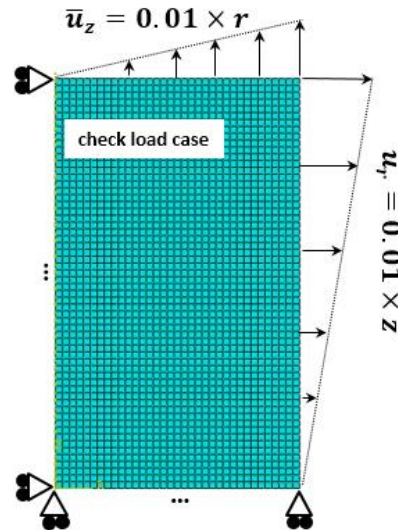

Figure A.2 – *Check load case for the validation of the elastic constants*

CURRICULUM VITAE

PERSONAL INFORMATION

Surname, Name: Gülaşık, Hasan
Nationality: Turkish (TC)
Date and Place of Birth: 06 October 1981, Yozgat
Marital Status: Single
Phone: +90 543 7288115
email: hasangulasik@gmail.com

EDUCATION

Degree	Institution	Year of Graduation
MS	METU, Department of Aerospace Engineering	2014
BS	METU, Department of Mechanical Engineering	2004
High School	İncirli High School, Ankara	1999

WORK EXPERIENCE

Year	Place	Enrollment
2014 - 2018	METU, Department of Aerospace Engineering	Project Researcher
2007 - 2013	Turkish Aerospace Industries	Structural Analysis Specialist
2005-2007	Askam Kamyon İmalat ve Ticaret A.Ş.	Project Engineer

FOREIGN LANGUAGES

Advanced English

PUBLICATIONS

1. Gülaşık, H., Göktepe, S., Gürses, E. 2018. "A Modulus Gradient Model for an Axially Loaded Inhomogeneous Elastic Rod", Meccanica, 53, 2573–2584
2. Gülaşık, H., Çöker, D. 2014. "Delamination-Debond Behaviour of Composite T-Joints in Wind Turbine Blades", Journal of Physics Conference Series 524(1), 012043

HOBBIES

Photography, politics